Repeating seismicity across the Earth-Moon system



Alice Turner

Linacre College

University of Oxford

A thesis submitted for the degree of

Doctor of Philosophy

To Granddad Ron.
Thank you for teaching me to have courage and determination.

Acknowledgements

This thesis would not have been possible without the support of my supervisor Jessica Hawthorne. Thank you for all your encouragement and guidance. But also for giving me the freedom to explore and learn from my own mistakes. I would also like to thank my second supervisor Andrew Walker. Your help and feedback has been invaluable and you always have a wise word for every stressful academic situation.

Thank you to the earthquakes mechanics group ("the shakey bois") and the wider seismology group at Oxford: Yannick Caniven, Hui Huang, Julien Renou, Robin Sullivan, Ben Fernando, Matthew Kemp, Miriam Gauntlett along with many others. Special thanks should go to Dan Gittins and Rebecca Colquhoun, for putting up with me when I complain and for providing motivational speeches, without whom this thesis would not have come to fruition. I am also thankful to all the other PhD students in the Department of Earth Sciences who shared all the highs and lows of my PhD journey: Duhita, Gwen, Mhari, Hannah and many many others.

My gratitude also extends outside of Oxford. Thank you, Matthew Gaddes, for your input on the third chapter of this thesis and to all the other researchers at COMET for accepting this lunar seismologist into your ranks. Thank you to Camilla Cattania for her help with understanding the models of repeating earthquakes and feedback on the paper that makes up the second chapter of this thesis. Thank you Jannes Münchmeyer for his valuable and helpful comments and for keeping me company at many conferences. Thanks should also go to Ceri Nunn and Taichi Kawamura for helping to understand the quirks lunar seismic data at the start of this project. I would like to express my deepest gratitude to Ana Ferreira, Paula Koelemeijer and the rest of the UCL seismology group. Thank you for starting me on this seismology journey and your continued support and encouragement.

I am indebted to my family - my mum, dad, and sister Charlotte for their continued support throughout my extended education. And to my newest family member, Valentin – living with you has been the highlight of being in Oxford. I would have never been able to do this without our dinner and trashy TV routine.

I would also like to thank all of my fluffy friends of the feline variety – Ariel, Cosmo, Halley, and Scout, and of the canine variety – Tez, Pepper, and Sherwa. Your silly antics always bring a smile to my face.

And finally, thank you to Edward. Thank you for all your belief in me, even when I don't quite believe it myself. Thank you for all the un-PhD-related adventures we have had, and I am excited for all the ones to come.

This work was primarily funded by UK Research and Innovation by an STFC scholarship. Supplementary funding was received from Linacre College and the British Geophysical Association travel fund.

Statement of Authorship

The work in Chapter 2 is in preparation to be submitted to Geophysical Research Letters under the following title:

Turner, A.R., Hawthorne J.C. and Cattania, C. (in prep.). *Searching for partial ruptures in Parkfield, California.*

Jessica Hawthorne supervised the project and provided the code to identify co-located earthquakes in Parkfield. Camilla Cattania provided Figure 2.1 and provided valuable insights into the interpretation. Alice Turner authored the paper and figures (which were improved with comments and suggestions from the authors), modified the original code supplied by Jessica Hawthorne, wrote supplementary code and conducted the analysis.

The work in Chapter 3 has been accepted for publication in the Journal of Geophysical Research: Planets. under the following title:

Turner, A.R., Hawthorne, J. C., and Gaddes, M. (2022). *Stresses in the lunar interior: insights from slip directions in the A01 deep moonquake nest.*

Jessica Hawthorne supervised the project and provided the original principal component analysis code. Matthew Gaddes provided the ICASAR code to carry out the cluster analysis. Alice Turner authored the paper and figures (which were improved with comments and suggestions from the authors), modified the original codes supplied by Jessica Hawthorne and Matthew Gaddes, wrote supplementary code, and conducted the analysis.

Chapter 4 of this thesis uses that same principal component analysis code supplied by Jessica Hawthorne. Alice Turner authored the chapter and figures, modified the original codes supplied by Jessica Hawthorne, wrote supplementary code and conducted the analysis.

Abstract

Repeating earthquakes are a unique seismic phenomenon where the same fault patch regularly fails. They occur in various settings and are useful geophysical tools to monitor and image the subsurface. However, we do not understand the underlying physics that generates repeating earthquakes. I focus on two subsets of these repeaters: in Parkfield, California and in the Moon.

I examine repeaters in Parkfield to test a model where the deficit between seismic slip and long-term slip on the fault is explained by partial ruptures. I find that partial ruptures can accommodate $\sim 30\%$ of the slip on the fault, but this is not enough to explain the slip deficit on the fault, and an alternative model may be required.

I use deep moonquake observations to constrain the tectonic stress in the moon. Some deep moonquakes appear to slip backwards relative to other moonquakes. There are two models for these backwards slipping events: a large tectonic stress or a large tidal stress. To discriminate between these two models, I apply principal component analysis to the waveforms of deep moonquakes. I find the tidal stress to be the main driver of deep moonquakes and place an upper constraint of 0.1 MPa on any tectonic stress in the lunar interior.

Finally, I align deep moonquakes to reduce the uncertainty of arrival times; the uncertainty can be up to $\sim$10 seconds for P-arrivals and $\sim$4 seconds for S-arrivals. This limits our ability to use this data to locate deep moonquakes. To reduce the uncertainty, I align deep moonquakes to a reference event using principal component analysis. The method aligns the P-arrivals of 20 - 40 % of the real deep moonquakes to within 1.5 seconds of the reference event – a significant improvement relative to the original absolute error.

Contents

List of Figures **x**

Nomenclature **xiv**

1 Introduction **1**
1.1 Identifying repeating earthquakes 4
1.1.1 Location criteria for identifying repeating earthquakes 5
1.1.2 Waveform similarity criteria for identifying repeating earthquakes 6
1.2 Repeating earthquakes on the San Andreas Fault 7
1.2.1 Setting of repeating earthquakes 7
1.2.2 Open questions about repeating earthquakes – the moment recurrence problem 9
1.2.3 Models for repeating earthquakes 10
1.3 Repeating deep moonquakes 14
1.3.1 Lunar instrumentation 14
1.3.2 Lunar seismic signals 15
1.3.3 Setting of repeating deep moonquakes 18
1.3.4 Open questions about deep moonquakes 20
1.4 Thesis road map 27

2 Searching for partial ruptures in Parkfield, California **29**
2.1 Introduction 31
2.2 Predictions from rate and state models 33
2.3 Finding repeaters and partial ruptures 34
2.3.1 Identifying repeating earthquakes 36
2.3.2 Identifying partial ruptures 37
2.4 Results 37
2.4.1 Analysing repeating earthquakes and partial ruptures 39
2.4.2 Moment-recurrence scaling 42
2.4.3 Testing for bias in analysis 44
2.5 Discussion 47

2.5.1 Partial rupture slip budget and repeater recurrence intervals 47
2.5.2 How big are repeaters relative to their nucleation size R_∞? 47
2.5.3 Compatibility of observations with the model 48
2.6 Conclusion 49

3 Stresses in the lunar interior: insights from slip directions in the A01 deep moonquake nest 50
3.1 Introduction 52
3.1.1 Motivation 53
3.1.2 Models of reversed polarity moonquakes 54
3.2 Data selection and initial processing 57
3.3 Principal component analysis of A01 moonquake waveforms 59
3.4 Qualitative analysis of principal components (G) 63
3.5 Quantitative analysis of the number of slip directions 63
3.5.1 Determining number of slip directions using unbiased principal component coefficients (m') 64
3.5.2 Determining number of slip directions using the similarity of principal component vectors (G) 67
3.5.3 Partitioning of slip between directions 69
3.6 Validation 71
3.6.1 Potential influence of waveform alignment 72
3.6.2 Potential influence of scattering 73
3.7 Discussion 75
3.7.1 Explaining reversed polarity moonquakes 75
3.7.2 Implications of a small tectonic stress 76
3.7.3 Further application to moonquakes and earthquakes 77
3.8 Conclusion 78

4 Using principal component analysis to improve relative arrival times of deep moonquakes 79
4.1 Introduction 81
4.2 Searching for relative time-shifts of deep moonquakes 83
4.2.1 Applying principal component analysis to deep moonquake waveforms 83
4.2.2 Assumptions 85
4.2.3 Solving a minimisation problem for time-shifts 86
4.2.4 Testing waveform alignment 88
4.3 Synthetic verification 89
4.3.1 Generating synthetics 89
4.3.2 Aligning identical waveforms 89

4.3.3 Aligning similar waveforms 90
4.4 Real deep moonquakes 94
4.4.1 Selecting deep moonquake stacks 94
4.4.2 Aligning deep moonquake stacks 95
4.5 Discussion 96
4.5.1 Implications for moonquake locations 96
4.5.2 Implications for lunar interior 98
4.6 Conclusion 99

5 General conclusions and perspectives 100
5.1 Chapter aims 101
5.1.1 Chapter 2: Searching for partial ruptures in Parkfield, California 101
5.1.2 Chapter 3: Stresses in the lunar interior: insights from slip directions in the A01 deep moonquake nest 102
5.1.3 Chapter 4: Using principal component analysis to improve relative arrival times of deep moonquakes 103
5.2 Future work 104
5.3 Broader outlook 106
5.3.1 Repeating earthquakes 106
5.3.2 Lunar seismology 107
5.3.3 Earth analogues for deep moonquakes 109
5.4 Concluding remarks 110

Appendices

A Supporting information for "Searching for partial ruptures in Parkfield, California" 112
A.1 Derivation of slip in partial ruptures 112

B Supporting information for "Stresses in the lunar interior: insights from slip directions in the A01 deep moonquake nest" 120

C Supporting information for "Using principal component analysis to improve relative arrival times of deep moonquakes" 144

References 148

List of Figures

1.1 Different environments across the Earth and the Moon where repeating seismicity has been observed. 2
1.2 Two methods of identifying repeating earthquakes. 5
1.3 Distribution of repeating earthquakes in California. 8
1.4 Locked patches embedded in a creeping fault. 9
1.5 Magnitude-recurrence interval scaling for repeating earthquakes. . . 10
1.6 Models for repeating earthquakes. 12
1.7 Nearside and farside of the Moon showing location of Apollo seismic stations. 16
1.8 Apollo seismic instrument response. 16
1.9 Comparison of a deep earthquake and a deep moonquake. 17
1.10 Structure of the interior of the Moon. 19
1.11 Fourier amplitude spectra of the occurrence times of 9 deep moonquake nests. 20
1.12 Pressure and temperature conditions of deep moonquakes. 24
1.13 Models of deep moonquake mechanisms. 26

2.1 Example of full and partial ruptures from simulations. 35
2.2 Seismicity of the Parkfield region. 38
2.3 Examples of repeaters and all of their co-located events, made up of partial ruptures and repeating earthquakes. 40
2.4 Moment-recurrence scaling and the total moment in repeating earthquakes identified from the NCEC. 43
2.5 Total moment in repeating earthquakes to the total moment to partial ruptures, normalised by the number of repeating earthquakes in each sequence from NCEC catalogue. 44
2.6 Moment-recurrence scaling and the total moment in repeating earthquakes identified from the Waldhauser and Schaff (2021) repeating earthquake catalogue. 45
2.7 Log slip per repeating cycle versus median moment for each repeater and its co-located events. 46

3.1 Models for reversed polarity deep moonquakes. 56

3.2 Deep moonquake waveforms used for PCA decomposition, recorded at station S12, channel MHN, in the peaked operation mode. 59
3.3 Illustration of the PCA decomposition for the A01 moonquakes. . . 62
3.4 Principal components derived from the S12 MHN data in the peaked operational mode of the instrument. 64
3.5 Unbiased coefficients of principal components, from the S12 MHN data in the peaked operational mode. 67
3.6 Clustering results of bootstrapped principal component vectors $\mathbf{G}$, obtained for S12 MHN in peaked operational mode. 70
3.7 Slip coefficient ratio $|m'_{1k}/m'_{2k}|$ for each station and channel. 71
3.8 Normalised unbiased slip coefficients for the first and second Green's functions. 72
3.9 Testing the influence of inaccurate waveform alignment. 74
3.10 Testing the influence of scattering. 74

4.1 Ray paths of deep moonquakes through the lunar mantle. 85
4.2 Illustration of the multi-step iterative grid search in two dimensions. 86
4.3 Example synthetic waveform 90
4.4 Objective functions for the relative time-shifts between synthetic waveforms generated using 1, 2, 3, 4, 5, and 6 principal components. 91
4.5 Synthetic waveforms aligned to within 0.5 seconds of true alignments. 92
4.6 Synthetic waveforms aligned when 3 waveforms are misaligned by 8 seconds. 93
4.7 Example real deep moonquake stack 94
4.8 Location of the deep moonquake stacks used in this study 95
4.9 Alignment of real deep moonquake stacks recorded at station S16. . 97

A.1 Moment-recurrence scaling and the total moment in repeating earthquakes identified in the NCEC catalogue assuming a stress drop of 3 MPa. 114
A.2 Moment-recurrence scaling and the total moment in repeating earthquakes identified in the NCEC catalogue assuming a stress drop of 10 MPa and a Wyss magnitude scaling. 115
A.3 Moment-recurrence scaling and the total moment in repeating earthquakes identified in the NCEC catalogue using the location error ellipse reported in the NCEC catalogue. 116
A.4 Total moment in repeating earthquakes to the total moment to partial ruptures, normalised by the number of repeating earthquakes in each group of co-located events identified using the 95^{th} percentile error ellipse in the NCEC catalogue. 117

A.5 Total moment in repeating earthquakes to the total moment to partial ruptures, normalised by the number of repeating earthquakes in each group of co-located events identified by Waldhauser and Schaff (2021). 117
A.6 Distribution of the magnitudes of events from the Waldhauser and Schaff (2021) repeating catalogue that were not identified in the catalogue of repeating earthquakes from the NCEC catalogue. . . . 118
A.7 Linear Gutenberg-Richter distribution for earthquakes in Parkfield. 118
A.8 Correction for the NCSN catalogues detection bias. 119

B.1 Template deep moonquake waveforms. 121
B.2 Deep moonquake waveforms used for PCA decomposition, recorded at station S12, channel MHE, in the peaked operation mode. 121
B.3 Deep moonquake waveforms used for PCA decomposition, recorded at station S12, channel MHN, in the flat operation mode. 123
B.4 Deep moonquake waveforms used for PCA decomposition, recorded at station S12, channel MHE, in the flat operation mode. 124
B.5 Deep moonquake waveforms used for PCA decomposition, recorded at station S16, channel MHN, in the peaked operation mode. 125
B.6 Deep moonquake waveforms used for PCA decomposition, recorded at station S16, channel MHE, in the peaked operation mode. 126
B.7 Deep moonquake waveforms used for PCA decomposition, recorded at station S16, channel MHN, in the flat operation mode. 127
B.8 Deep moonquake waveforms used for PCA decomposition, recorded at station S16, channel MHE, in the flat operation mode. 127
B.9 Principal components derived from the S12 MHE data in the peaked operational mode of the instrument. 128
B.10 Principal components derived from the S12 MHN data in the flat operational mode of the instrument. 128
B.11 Principal components derived from the S12 MHE data in the flat operational mode of the instrument. 129
B.12 Principal components derived from the S16 MHN data in the peaked operational mode of the instrument. 130
B.13 Principal components derived from the S16 MHE data in the peaked operational mode of the instrument. 131
B.14 Principal components derived from the S16 MHN data in the flat operational mode of the instrument. 132
B.15 Principal components derived from the S16 MHE data in the flat operational mode of the instrument. 132
B.16 Unbiased coefficients of the principal components, from the S12 MHE data in the peaked operational mode. 133

B.17 Unbiased coefficients of the principal components, from the S12 MHN data in the flat operational mode. 134
B.18 Unbiased coefficients of the principal components, from the S12 MHE data in the flat operational mode. 135
B.19 Unbiased coefficients of the principal components, from the S16 MHN data in the peaked operational mode. 136
B.20 Unbiased coefficients of the principal components, from the S16 MHE data in the peaked operational mode. 137
B.21 Unbiased coefficients of the principal components, from the S16 MHN data in the flat operational mode. 138
B.22 Unbiased coefficients of the principal components, from the S16 MHE data in the flat operational mode. 139
B.23 Clustering results of bootstrapped $\mathbf{G}$, obtained for S12 MHE in peaked operational mode. 140
B.24 Clustering results of bootstrapped $\mathbf{G}$, obtained for S12 MHN in flat operational mode. 140
B.25 Clustering results of bootstrapped $\mathbf{G}$, obtained for S12 MHE in flat operational mode. 141
B.26 Clustering results of bootstrapped $\mathbf{G}$, obtained for S16 MHN in peaked operational mode. 141
B.27 Clustering results of bootstrapped $\mathbf{G}$, obtained for S16 MHE in peaked operational mode. 142
B.28 Clustering results of bootstrapped $\mathbf{G}$, obtained for S16 MHN in flat operational mode. 142
B.29 Clustering results of bootstrapped $\mathbf{G}$, obtained for S16 MHE in flat operational mode. 143
B.30 Slip coefficient ratio $|m'_{2k}/m_{1k}|'$ for each station and channel. 143

C.1 TauP theoretical ray paths of deep moonquakes through the lunar mantle. 145
C.2 Alignment of real deep moonquake stacks recorded at station S16 with shifts of 1.5 seconds 146
C.3 Alignment of real deep moonquake stacks recorded at station S12 with shifts of 10 seconds. 147

Nomenclature

List of acronyms

ALSEP . . . . Apollo Lunar Surface Experiments Package

COMET . . . Centre for Observation and Modelling of Earthquakes and Tectonics

FSS . . . . . Farside Seismic Suite

HBDSCAN . . Hierarchical density-based spatial clustering of applications with noise

ICASAR . . . An algorithm for robustly applying independent component analysis to InSAR data by Gaddes et al. (2019)

IPGP . . . . . Institut de Physique du Globe de Paris

miniSEED . . A subset of the SEED (The Standard for the Exchange of Earthquake Data) used for time series data.

MHX . . . . . X component of a 3-component seismometer

MHY . . . . . Y component of a 3-component seismometer

NCEDC . . . . Northern California Earthquake Data Center

NCSN . . . . . Northern California seismic network

P . . . . . Primary/pressure/compressional seismic phase

PCA . . . . . Principal component analysis

PSE . . . . . Passive seismic experiment

S . . . . . Secondary/shear seismic phase

S12 . . . . . Seismic station in the lunar seismic network deployed during the Apollo 12 mission

S14 . . . . . Seismic station in the lunar seismic network deployed during the Apollo 14 mission

S15 . . . . . Seismic station in the lunar seismic network deployed during the Apollo 15 mission

S16 . . . . . Seismic station in the lunar seismic network deployed during the Apollo 16 mission

SCEC . . . . . Southern California Earthquake Center

STFC . . . . . Science Technology Facilities Council

t-SNE . . . . . t-distributed stochastic neighbour embedding

List of symbols

a,b . . . . . rate and state parameters

D_c . . . . . rate and state critical slip distance (m)

G . . . . . Green's function/principal component

j . . . . . subscript denote a principal components

k . . . . . subscript denote a moonquake waveform

t . . . . . time (s)

I_q . . . . . cluster quality factor

M . . . . . local magnitude (Nm)

m . . . . . moment tensor element/ principal component coefficent

m' . . . . . unbiased principal component coefficients

M_0 . . . . . seismic moment (Nm)

M_w . . . . . magnitude

R . . . . . asperity radius (m)

R_∞ . . . . . nucleation radius (m)

S . . . . . slip (m)

T_r . . . . . recurrence interval (s)

U . . . . . matrix of waveforms

V . . . . . sliding velocity (m/s)

V^* . . . . . reference sliding velocity (m/s)

V_{creep} . . . . . long-term geodetic slip rate/ creep rate (cm/year)

$\Delta\sigma$ . . . . . stress drop (MPa)

Θ . . . . . state parameter

μ . . . . . co-efficient of friction

μ_0	static co-efficient of friction
ν	Poisson's ratio
τ	relative time-shift between deep moonquake waveforms (s)

1 Introduction

Contents

1.1 Identifying repeating earthquakes 4
1.1.1 Location criteria for identifying repeating earthquakes . 5
1.1.2 Waveform similarity criteria for identifying repeating earthquakes 6
1.2 Repeating earthquakes on the San Andreas Fault . . . 7
1.2.1 Setting of repeating earthquakes 7
1.2.2 Open questions about repeating earthquakes – the moment recurrence problem 9
1.2.3 Models for repeating earthquakes 10
1.3 Repeating deep moonquakes 14
1.3.1 Lunar instrumentation 14
1.3.2 Lunar seismic signals 15
1.3.3 Setting of repeating deep moonquakes 18
1.3.4 Open questions about deep moonquakes 20
1.4 Thesis road map 27

It is currently not possible to predict exactly when and where earthquakes will occur, nor how large they will be. Yet some specific earthquakes appear to be more predictable than others. These earthquakes happen over and over again in the same place with surprising regularity – so-called "repeating earthquakes".

Repeating earthquakes are hosted on faults in a range of environments and driven by various stresses, some of which are illustrated in Figure 1.1. They are abundant on shallow creeping faults in the Earth's crust (Chen et al., 2020; Chiaraluce

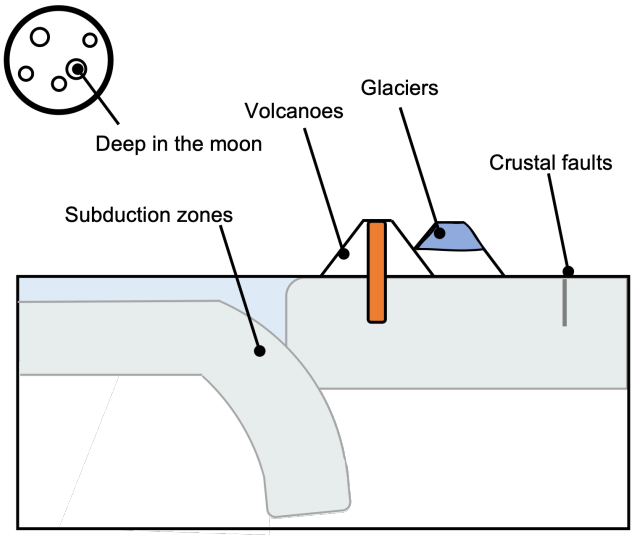


Figure 1.1: Some of the different environments across the Earth and the Moon where repeating seismicity has been observed.

et al., 2007; Chen et al., 2009), including the San Andreas Fault (Nadeau et al., 1995; Vidale et al., 1994; Abercrombie et al., 2020; Williams et al., 2019; Lengliné and Marsan, 2009; Waldhauser and Schaff, 2021), and the North Anatolian Fault (Uchida and Bürgmann, 2019; Schmittbuhl et al., 2016). Subduction zones also host repeating earthquakes on the slab interface (Igarashi et al., 2003; Dominguez et al., 2016; Malebran et al., 2020; Huang and Meng, 2018; Chalumeau et al., 2021) and within the subducting slab to depths of up to 600 km (Wiens and Snider, 2001; Yu and Wen, 2012; Poli et al., 2016; Prieto et al., 2012). Repeating earthquakes are not limited to plate boundaries; they can also occur in more exotic settings including volcanoes (White et al., 1998; Wellik et al., 2021; Petersen, 2007; Poupinet et al., 1996), glaciers (Kufner et al., 2021; Danesi et al., 2007), landslides (Yamada et al., 2016; Gomberg et al., 2011; Poli, 2017), or triggered by fluid injection (e.g., Lengliné et al., 2014; Cochran et al., 2018). Repeating seismicity has even been located on other bodies in the solar system, such as in clusters 700 - 1200 km inside the Moon (Frohlich and Nakamura, 2009; Bulow et al., 2007) and on Mars (Sun and Tkalčić, 2022).

Repeating earthquakes provide a stable natural source of seismic energy, and as such, they are a common tool for a range of geophysical applications. They are used

to monitor changes in subsurface properties over time such as the temporal variation in seismic velocities (Schaff and Beroza, 2004; Rubinstein et al., 2007; Kelly et al., 2013) or seismic anisotropy (e.g., Uchida et al., 2020; Peng and Ben-Zion, 2005), to observe rotation of the Earth's inner core (Yang and Song, 2020; Yu, 2016), or to track geodetic slip rate at depth on creeping faults (Waldhauser and Schaff, 2021; Nadeau and McEvilly, 1999; Turner et al., 2013). Repeating earthquakes are also used to understand seismic processes; small repeating earthquakes are a simple and intuitive phenomenon that may help us understand the earthquake cycle and the processes that control larger, more damaging earthquakes (Uchida and Bürgmann, 2019). The changes in magnitude or time interval between repeating earthquakes are often used to understand postseismic slip (Huang and Meng, 2018), transient triggering (Wu et al., 2014) and fault healing (Marone et al., 1995). Despite the functionality of repeating earthquakes, in many cases we still do not understand the physical processes that generate and control them.

In this thesis, I use seismic observations to understand the processes that create and control repeating earthquakes. I focus on two types of events: repeating earthquakes on the San Andreas Fault and repeating deep moonquakes. In Chapter 2, I focus on repeating earthquakes on the San Andreas Fault in Parkfield. The recurrence time of small repeating events should be intuitive – the next earthquake on a particular patch will occur when the strain drop has recovered. But these events occur less often than one would expect from theoretical scaling laws. Recent models suggest an explanation: small earthquakes could occur between repeating events as "partial ruptures". Using high-quality seismic catalogues in Northern California, I systematically search for these partial ruptures. I do not find enough partial ruptures to account for long recurrence times of repeating earthquakes, and an alternate model may be required to explain why repeating earthquakes happen less often than expected.

In Chapter 3, I then focus on deep repeating moonquakes. Deep moonquakes occur between 700 - 1200 km depth and have the potential to provide unique insight into the stresses acting in the deep lunar interior. I use deep moonquake

observations to constrain the tectonic stress in the moonquake source region. Some of these deep moonquakes appear to slip backwards i.e, in the opposite direction to events that happen on the same fault plane. There are two models for these backwards slipping events: a large tectonic stress that varies in space or a large tidal stress that changes in time. To discriminate between these two models, I use principal component analysis of waveforms of deep moonquakes. I find the tidal stress to be the main driver of deep moonquakes and place for the first time an upper constraint of 0.1 MPa on any tectonic stress in the lunar interior.

Finally, in Chapter 4, I continue my work on deep moonquakes by improving estimates of P- and S-wave arrival times, which are crucial for inversions of velocity structure and source location. The waveform characteristics of lunar events make picking arrival times challenging. To address this, I apply principal component analysis to deep moonquake waveforms to improve estimates of the relative timing between these events. I find the PCA can help reduce the uncertainty of the relative arrival times of 20- 40% of the deep moonquakes I test.

In this introductory chapter, I provide an in-depth background into the concepts examined further in this thesis. As this thesis is in an integrated format, Chapters 2 and 3 have been prepared for publication and appear as such. Although some material in this introductory chapter will be repeated in the introduction of each chapter, I also present additional background material not required for publication but necessary to provide context to the thesis overall. In Section 1.1, I describe how researchers identify repeating earthquakes. In Section 1.2, I provide detailed background on why repeating earthquakes seem to occur less often than we expect. In Section 1.3, I provide details of the lunar data and the many unresolved problems of deep moonquakes, including their location, mechanism and driving stress. Finally, in Section 1.4, I outline the aims of each chapter of this thesis.

1.1 Identifying repeating earthquakes

I begin by describing how researchers identify repeating earthquakes. A perfect repeating sequence consists of two or more earthquakes that rupture the same small

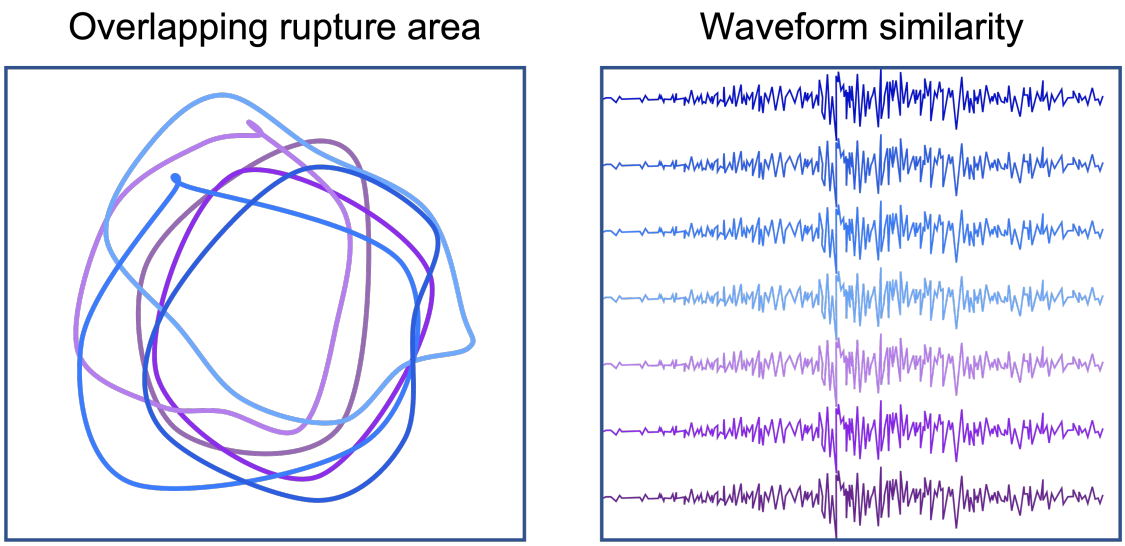


Figure 1.2: Cartoon of the the two main methods of identifying repeating earthquakes – overlapping rupture areas and similarity of waveforms.

section of the fault (termed the "fault patch" or "asperity"). The pair have the same location, magnitude and focal mechanism and a similar source time function. The pair also have highly similar waveforms since the generated seismic waves should follow the same path from the source to the receiver. There are two common methods to identify repeating earthquakes: using overlapping rupture areas based on accurate event locations or using waveform similarity (Figure 1.2). In practice, identifying repeating earthquakes can be challenging – all data contain noise, and the slip and area of the fault that ruptures in repeaters can have slight variations.

1.1.1 Location criteria for identifying repeating earthquakes

The first method to identify repeating earthquakes is inherently related to their definition – events that have an overlapping rupture area (e.g., Williams et al., 2019; Waldhauser and Ellsworth, 2002). First, events are relocated to determine high-precision hypocentre locations, often obtained via double-difference relocations (Waldhauser and Ellsworth, 2002). From these locations, co-located events can then be identified by searching for overlapping rupture areas. The rupture area of an earthquake is commonly calculated using a simple model of a circular asperity (Eshelby, 1957):

$$R = \frac{7}{16}\frac{M_0}{\Delta\sigma}^{1/3}, \tag{1.1}$$

where R is the source radius, M_0 is the seismic moment, and $\Delta\sigma$ is a magnitude independent stress drop. The assumed value of the stress drop varies between studies but is normally between 1 - 10 MPa (Lengliné and Marsan, 2009; Williams et al., 2019; Waldhauser and Schaff, 2021). Using a stress drop of 10 MPa, a M_w 2 earthquake has a radius of ∼50 m. Assuming a lower stress drop leads to a larger source radius.

Since this method relies on high-precision hypocentres, it requires a large number of stations with good geographical distribution and enough high-quality arrival times to accurately locate the events.

1.1.2 Waveform similarity criteria for identifying repeating earthquakes

A second, more common method to identify repeating earthquakes uses waveform similarity. If a pair of repeating events rupture the same patch and are both recorded at the same station, the resulting waveforms will have a high similarity. The similarity is measured using cross-correlation or cross-spectra. A pair of events will be considered repeaters if the cross-correlation between them is above some threshold value.

This method is particularly advantageous for identifying repeating events with sparse station coverage. In principle, repeating earthquakes can be identified with only a single station operating throughout the analysis period – as is the case for the lunar data.

However, the waveform similarity is controlled by not only the separation between a pair of events but also many other factors, including station azimuth, epicentral distance, and velocity structure, so some repeating earthquakes may have lower waveform similarity (Uchida, 2019; Gao et al., 2021).

Several studies use a hybrid of both approaches (e.g., Waldhauser and Schaff, 2021; Lengliné and Marsan, 2009), including criteria on both the overlap of the

rupture area and the waveform similarity to ensure only true repeating earthquakes are identified.

In this thesis, I study two sets of repeating earthquakes occurring in very different environments and with very different station availability and data quality. I identify repeaters in California in using a location criteria and I use a catalogue of repeating moonquakes identified using waveform similarity criteria (Nakamura, 2003).

1.2 Repeating earthquakes on the San Andreas Fault

In this section, I provide background on the first type of repeating earthquake studied in this thesis: small magnitude repeating earthquakes in California. In California, repeating earthquakes have been observed along the San Andreas Fault (Nadeau et al., 1995; Vidale et al., 1994; Abercrombie et al., 2020; Williams et al., 2019; Lengliné and Marsan, 2009; Waldhauser and Schaff, 2021), the Hayward Fault (Schmidt et al., 2005; Bürgmann et al., 2000; Waldhauser and Ellsworth, 2002), the Calaveras Fault (Schaff et al., 2002; Templeton et al., 2008) and in the northern San Francisco Bay Area (Shakibay Senobari and Funning, 2019), as illustrated in Figure 1.3. In northern and central California, Waldhauser and Schaff (2021) identify 27,657 individual repeating earthquakes in 7,713 sequences. In the area close to the town of Parkfield in central California, repeating earthquakes make up over ∼50% of seismicity (Nadeau et al., 2004).

1.2.1 Setting of repeating earthquakes

Crustal repeating earthquakes, such as those in California, are associated with sections of the fault that are creeping (Uchida et al., 2015; Rubin et al., 1999). They are thought to represent the failure of brittle asperities, loaded by the surrounding creeping fault (e.g., Beeler et al., 2001), as illustrated in Figure 1.4. In this framework, repeating earthquakes reveal the relationship between seismic and aseismic slip on the fault; the seismic slip on a patch can be related to the surrounding aseismic slip loading the patch. On this basis, one can derive

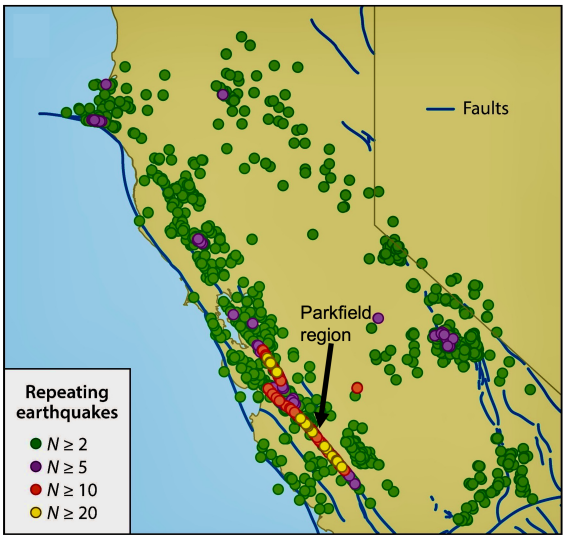


Figure 1.3: Distribution of repeating earthquakes in California coloured by the number of earthquakes in each sequence. Edited from Uchida and Bürgmann (2019)

the classical relationship between the recurrence interval (T_r, the time between sequential repeating earthquakes), the aseismic slip loading the patch (S_{creep}), the seismic moment of a repeating earthquake (M_0) and the static stress drop of an earthquake ($\Delta\sigma$). The static stress drop of a circular patch with radius r is defined as (Eshelby, 1957):

$$\Delta\sigma = \frac{7\pi S_{seis}}{16r}, \tag{1.2}$$

where S_{seis} is the seismic slip. The seismic moment is defined as:

$$M_0 = \mu\pi r^2 S_{seis}, \tag{1.3}$$

where μ is the shear modulus. For repeating earthquakes, we assume that the patch is locked between repeating earthquakes and therefore the the slip in each earthquake should match the long-term accumulated slip since the last event:

$$S_{seis} = S_{creep} = V_{creep} T_r, \tag{1.4}$$

where V_{creep} is the long-term creeping rate of the fault. By substituting Equation 1.4 into Equations 1.3 and 1.2 and solving for r, we find that the recurrence interval scales with moment as:

$$T_r = \frac{\Delta\sigma^{\frac{2}{3}} M_0^{\frac{1}{3}}}{1.81\mu V_{creep}}. \tag{1.5}$$

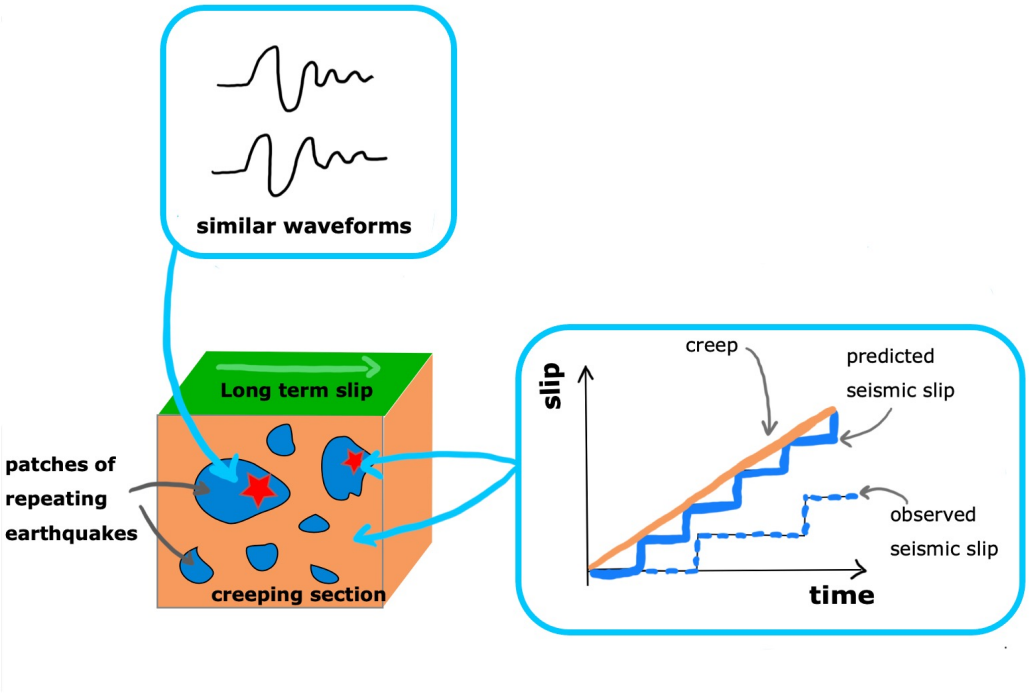


Figure 1.4: Repeating earthquakes are considered to be locked patches (blue) embedded in a creeping fault (orange). The creeping section slips at a steady rate, while the locked patches exhibit stick-slip behaviour, with the seismic slip accumulated matching the slip accumulated since the last event, as illustrated in the right panel. The top panel illustrates the high waveform similarity of the repeating earthquakes.

If there is no dependence of $\Delta\sigma$ or V_{creep} on M_0, then

$$T_r \propto M_0^{\frac{1}{3}}. \tag{1.6}$$

From this relationship, a M_w 2 earthquake in Parkfield has a theoretical recurrence interval of ~0.5 years, assuming the Parkfield slip rate of 23 mm/year (Nadeau and Johnson, 1998) and a stress drop of 10 MPa (Abercrombie, 2014; Allmann and Shearer, 2007; Imanishi and Ellsworth, 2006). A larger stress drop would lead to longer recurrence intervals.

1.2.2 Open questions about repeating earthquakes – the moment recurrence problem

In contrast to the theoretical scaling ($T_r \propto M_0^{\frac{1}{3}}$) derived above, Nadeau and Johnson (1998) observe that small magnitude repeating earthquakes in Parkfield

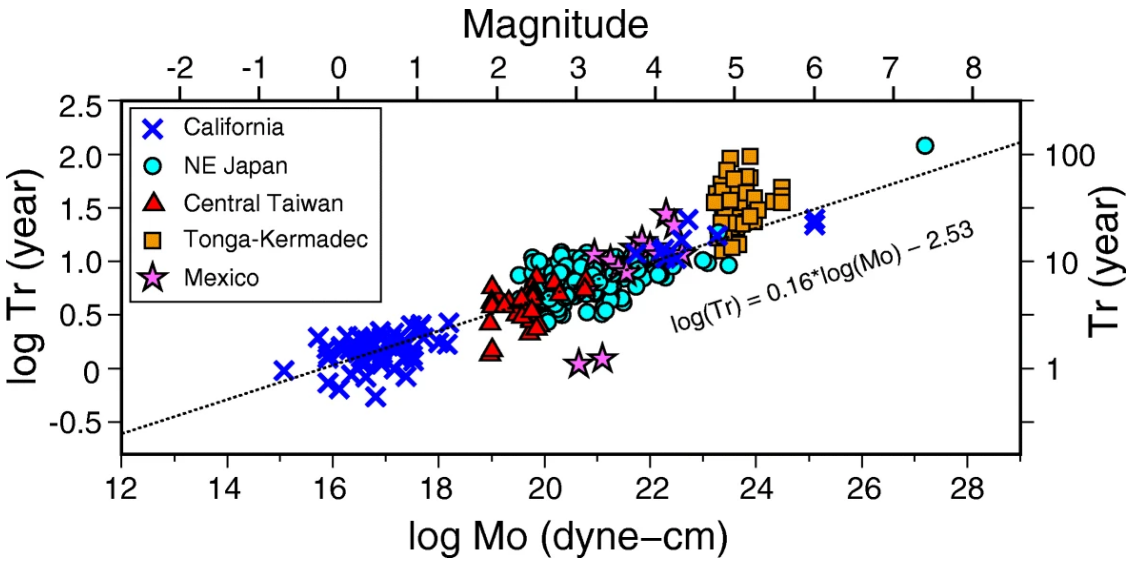


Figure 1.5: Relationship between the sequence averaged recurrence interval and sequence averaged moment of repeating earthquake sequences across global faults, normalised by plate convergence. Figure from Uchida (2019). Original data for each region is from Nadeau and Johnson (1998, San Andreas Fault), Chen et al. (2007, Central Taiwan), Yu and Wen (2012, Tonga-Kermadec), Dominguez et al. (2016, Mexico) and Uchida and Matsuzawa (2013, NE Japan).

have recurrence times that scale with moment as $T_r \propto M_0^{0.17}$. The recurrence interval scales much more weakly with the moment than in the theoretical scaling relationship, and thus the repeating earthquakes happen less often than expected. A M_w 2 earthquake has an observed recurrence interval of ∼3 years (Nadeau and Johnson, 1998), an order of magnitude larger than the theoretical recurrence interval of ∼0.5 years. This scaling persists across a range of geological settings, including Taiwan and Japan, when corrected for geodetically derived slip rate on these fault zones (Figure 1.5, Chen et al., 2007).

1.2.3 Models for repeating earthquakes

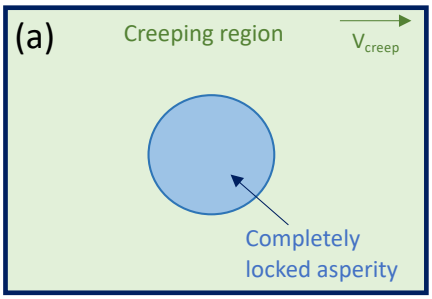
To explain the long recurrence times of repeating earthquakes, one of the assumptions made when deriving the theoretical scaling law must be incorrect: either (a) the stress drop is not magnitude independent, (b) the local slip rate does not match the geodetically observed slip rate at the surface, or (c) the patch is not locked between repeating earthquakes. A range of models have challenged each of these assumptions (Figure 1.6).

Nadeau and Johnson (1998) first suggested that the assumption of a constant stress drop for these repeating earthquakes may be incorrect (Figure 1.6a). For repeating earthquakes, the stress drop would have to be inversely proportional to the 1/4 the power of seismic moment to match the geodetically observed slip rate in Parkfield and recover the $T_r \propto M_0^{0.17}$ scaling (Chen et al., 2007). In this case, very small repeating events could have very high stress drop (∼2 GPa, Sammis and Rice, 2001). However, these high stress drops are two orders of magnitude larger than those that are observed for repeating earthquakes. And although the dependence of earthquake stress drops on magnitude is a debated subject, the observed stress drops of repeaters do not seem to depend on the magnitude (Abercrombie et al., 2020). Such high stress drops are also at odds with the strength of rock and would only be possible with perfect healing of the asperity between repeating earthquakes (Sammis et al., 1999).

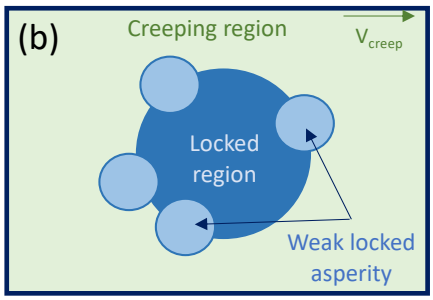
The second suite of models challenges the assumption that the local slip rate should match the geodetic slip rate observed at the surface. To create a locally different slip rate, Sammis and Rice (2001) present a model where repeating earthquakes occur at the edge of a larger locked asperity (Figure 1.6b). The stress shadow around this larger locked asperity alters the loading rate of the small weak repeating patch. The model recovers the $T_r \propto M_0^{0.17}$ scaling, with repeating earthquakes which have stress drops of 0.08 - 0.5 MPa.

Similarly, Anooshehpoor and Brune (2001) suggest a geometric explanation to create a lower local slip rate on the repeating asperity. In a foam block model, they create a strong inner asperity, enclosed in a larger creeping asperity, which is surrounded still by a larger locked fault (Figure 1.6c). The innermost strong asperity has a smaller local slip velocity than the medium-sized creeping asperity surrounding it, and the small asperity fails many times between larger system scale events of the whole locked fault.

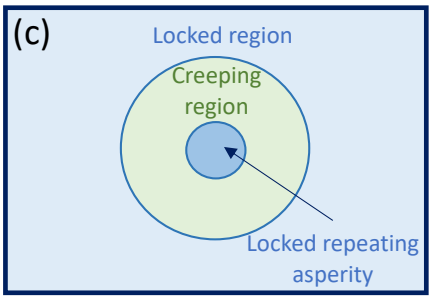
Williams et al. (2019) suggest an alternative method to create a lower local slip rate: if faults are made up of strands of sub faults, the long-term slip rate may vary spatially. As slip scales with the fault length (e.g., Watterson, 1986; Walsh



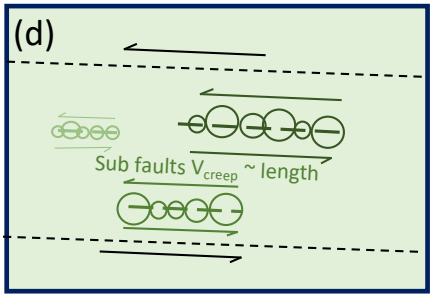
High stress drop
(Nadeau and Johnson, 1998)



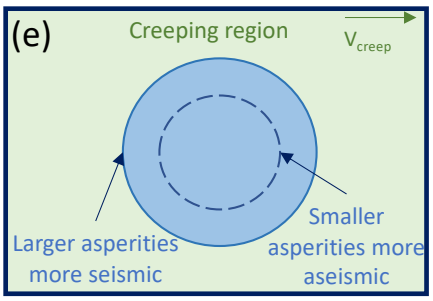
Weak asperities on edge larger locked asperity
(Sammis & Rice, 2001).



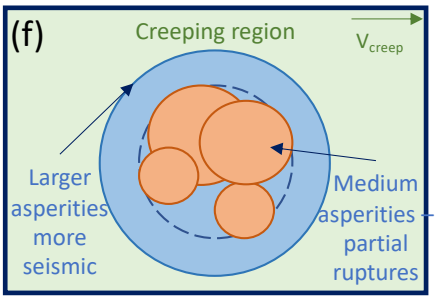
Cocentric locked and creeping asperities
(Anooshehpoor and Brune, 2001)



Varying geodetic slip rate
(Williams et al, 2019)



Aseismic slip on patch
(Beeler et al., 2001)



Aseismic slip and partial ruptures
(Chen and Lapusta, 2009, Cattania and Segall, 2018)

Figure 1.6: Models used to account for the deviation in scaling between the moment and the recurrence interval of repeating earthquakes.

and Watterson, 1988), smaller sub-faults will have lower slip rates (Figure 1.6d). Individual sub-faults follow the theoretical $T_r \propto M_0^{1/3}$ scaling, but when averaged across the large-scale regional fault, the $T_r \propto M_0^{0.17}$ scaling is recovered.

A final class of models challenges the assumption that the seismic patch is completely locked between the repeating events. Instead, seismic and aseismic slip can also contribute to the slip budget on the fault (Figures 1.6e and 1.6f). Beeler et al. (2001) first suggested that the smallest repeating asperities may experience a large amount of aseismic slip, with the ratio of seismic to aseismic slip on the patch reducing for larger events. More recently, models of seismic and aseismic slip on an asperity use a rate and state friction framework. Rate and state friction is a commonly used empirical relationship that describes the evolution of friction on the fault (Dieterich, 1979; Ruina, 1983). The change in friction, μ, is expressed in terms of the static coefficient of friction (μ_0), the sliding velocity (V), and the "state" (Θ) of the fault:

$$\mu = \mu_0 + a\frac{V}{V^*} + b\frac{V^*\Theta}{D_c}. \tag{1.7}$$

In Equation 1.7, a and b are constants thought to be related to the material properties, V^* is a reference sliding velocity, and D_c is the distance over which the evolution from μ_0 to μ occurs.

The rate and state models of repeating earthquakes assume a velocity weakening asperity embedded in a velocity strengthening fault. These models recover the $T_r \propto M_0^{0.17}$ scaling across a range of asperity sizes (Chen and Lapusta, 2009; Cattania and Segall, 2019) because the asperities are able to slip both seismically and aseismically. In these simulations, the specific behaviour of the asperity depends on its radius relative to the size of the smallest asperity that can host a seismic event (called the "nucleation size", R_∞).

For asperities that are smaller than the nucleation size ($R \leq R_\infty$), the patch is never fully locked and does not produce earthquakes. The patch only slips aseismically. For asperities that are small relative to the nucleation size ($R_\infty \leq R \leq 2R_\infty$), the edges of the fully locked asperity begin to move aseismically and creep.

As time progresses, this creeping region encroaches into the locked region, starting at the edge and moving radially inwards, causing the radius of the locked part of the patch to shrink. This continues until the whole patch is moving aseismically. At this point, an earthquake nucleates from the centre and ruptures the entire patch. For asperities with size $2R_\infty \leq R \leq 4.3R_\infty$, again, the creep encroaches into the locked region, shrinking the locked part of the patch. However, in this regime with a larger asperity, the creep front never reaches the centre; there is always a locked core to the patch. Earthquakes initiate on the edge of the patch in an aseismic region and rupture the entire patch. When R $\geq 4.3R_\infty$, the total area of the locked part of the patch is much larger than the total area of the aseismic region surrounding it. In this regime, the patch experiences small earthquakes that do not rupture the entire patch, termed "partial ruptures". In each of these regimes, the observed moment-recurrence scaling of the characteristic repeating earthquakes is recovered by relaxing the requirement that the patch is locked between events.

In Chapter 2, I test a recent rate-and-state model (Cattania and Segall, 2019) that considers predicts partial ruptures by searching for partial ruptures in Parkfield, California.

1.3 Repeating deep moonquakes

The second type of repeating seismicity considered in this thesis occurs in a more exotic setting – deep inside the Moon. These deep moonquakes were first observed when seismometers were placed on the near side of the Moon during the Apollo missions.

1.3.1 Lunar instrumentation

Five seismometers were successively placed by astronauts on the near side of the Moon during Apollo missions 11, 12, 14, 15 and 16. The first instrument deployed during Apollo 11 did not last the lunar night (Latham et al., 1970a). The four subsequent stations formed an almost equilateral triangle, with stations 12 and 14 at one corner, as illustrated in Figure 1.7. Each station was made up of a 3 component

"mid-period" instrument and a single component "short period" instrument (Nunn et al., 2020b). Although the two horizontal components for the mid-period sensor were intended to point north and east, they were misaligned for stations S12 and S16.

The mid-period instruments were operated in two instrument response modes, flat and peaked mode, illustrated in Figure 1.8. The peaked instrument response mode was the natural response of the seismometer, with a peak in the frequency response at about 0.45 Hz (Nunn et al., 2020b). The flat instrument mode was designed to be sensitive to a broader frequency range, from about 0.1 to 1 Hz, but was less stable, so instruments were mostly operated in peaked mode (Nunn et al., 2020b). The signals were sampled at 6.63 Hz for the mid-period instrument and 53 Hz for the short-period instrument, although there are small variations in sampling rate throughout the operation of the lunar seismic network (Nunn et al., 2017; Nunn et al., 2020b). The data were then transmitted from the Moon to the Earth. These instruments faithfully monitored the Moon until they were unceremoniously turned off in 1977, providing seven years' worth of lunar seismic data. The original data were stored on magnetic tapes, taking up over 50 m^2 of storage floor space (Nakamura et al., 1980). Careful preservation of this Apollo seismic data and conversion to the miniSEED format commonly used in seismology today (Nunn et al., 2017; Nunn et al., 2020a; Nunn et al., 2022) has fuelled continued seismic research with this over 50-year-old dataset, including the findings presented in this thesis.

1.3.2 Lunar seismic signals

Four main classes of signal were catalogued from the Apollo seismic data. The catalogue includes artificial impacts from spacecrafts, meteoroid impacts, and shallow moonquakes, but the most frequent type of lunar seismicity is deep moonquakes. Over 7000 small magnitude ($< M_w$ 3) deep moonquakes originating from 700 - 1200 km depth were recorded over the 7-year operational period of the instruments. Early in the processing of the lunar data, researchers found that many deep moonquakes had visually similar waveforms. They were grouped into "nests" of events with high waveform similarity, implying repeated rupture in the same location. Further

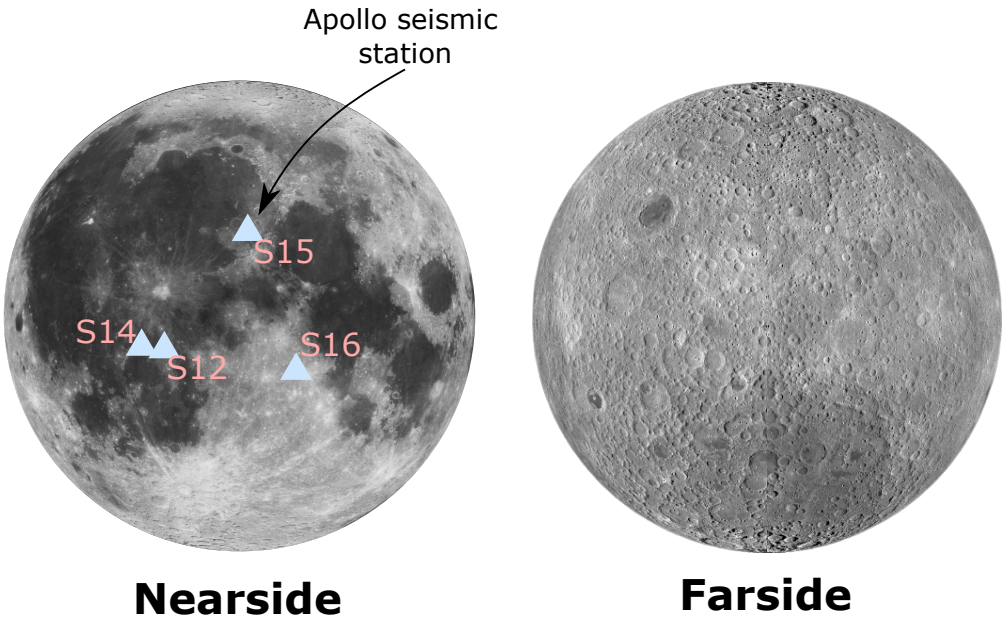


Figure 1.7: Nearside and farside of the Moon. The locations of the Apollo seismic stations on the near side of the Moon are shown as blue triangles. Images from NASA/Goddard/Arizona State University

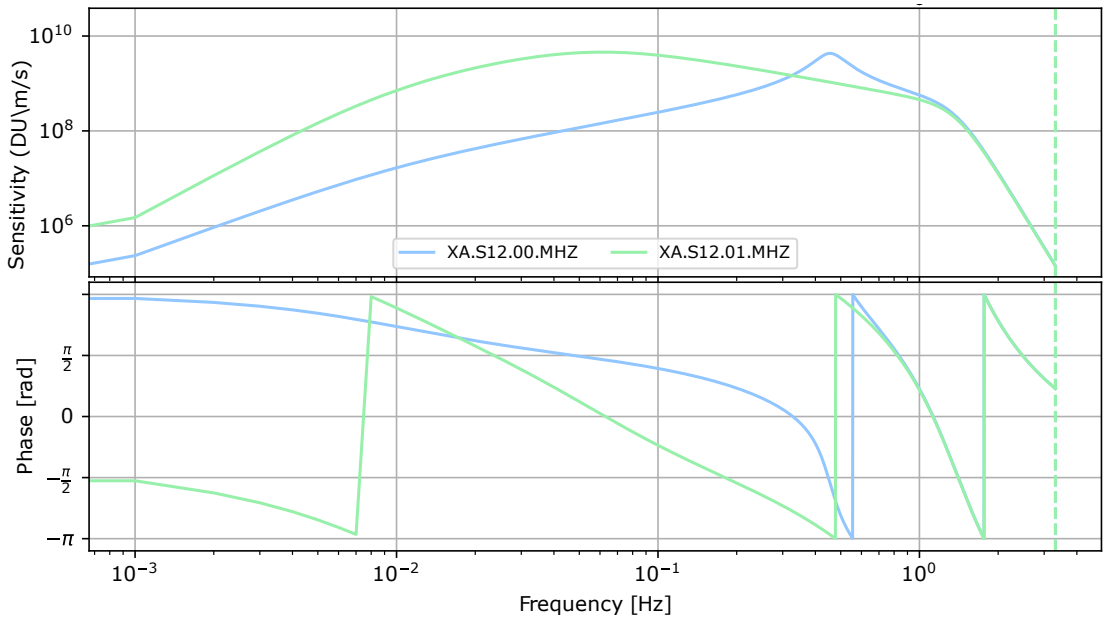


Figure 1.8: Top: The amplitude response of the Apollo seismometers. The peaked mode is shown in blue, and the flat mode is in green. **Bottom:** Phase response of the Apollo seismometers.

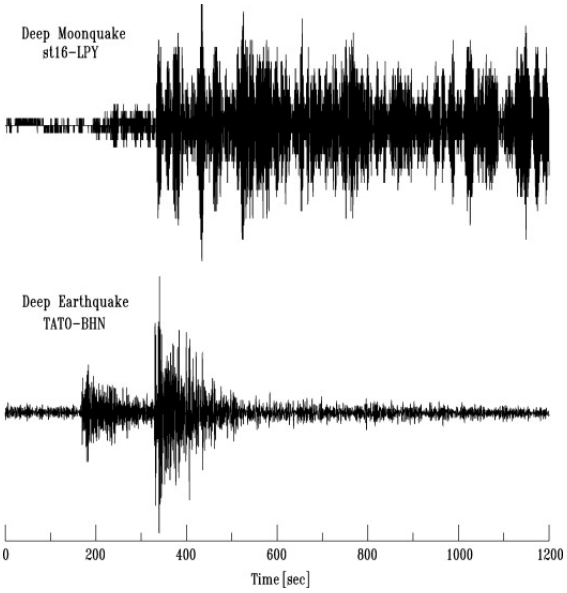


Figure 1.9: Top: Normalised horizontal-component displacement seismogram for a M_b 2.5 deep moonquake occurring on 5 June 1973 at Apollo lunar station S16. **Bottom**: Normalised horizontal-component displacement seismogram for a 629 km depth M_w 6 earthquake occurring in the Philippines on 23 May 1998 and recorded at station TATO. Figure from Frohlich and Nakamura (2009).

analysis revealed a ∼27 and ∼29-day periodicity in the occurrence times of deep moonquakes within these nests – they respond to the gravitational forces raised by the Earth on the Moon (Toksöz et al., 1977; Cheng and Toksöz, 1978; Goulty, 1979; Minshull and Goulty, 1988). At least 300 of these tidal deep moonquake nests have been identified (e.g., Nakamura et al., 1982; Nakamura, 1978; Lognonné et al., 2003), including ∼88 new nests recently identified using cross-correlation and clustering techniques (Bulow et al., 2005; Nakamura, 2003; Nakamura, 2005a). The largest nest, the A01 nest, is located 18° SW of Apollo station 12, at a depth of about 870 km (Nakamura, 2005b; Nakamura, 2005a) and contains over 400 individual repeating deep moonquakes (Nunn et al., 2020b). This nest will be the focus of Chapter 2 of this thesis.

The deep moonquake signals recorded by the seismic network are noticeably different from those observed on Earth, as highlighted in Figure 1.9. Compared to seismograms from Earth, the lunar seismograms have an especially long coda. The long coda is created by the highly fractured outer shell of the Moon, which allows seismic energy to reverberate (Nunn et al., 2020b; Blanchette-Guertin et al.,

2012; Nakamura et al., 1977). The large amplitude and greater duration of the seismic coda implies a lower intrinsic attenuation on the Moon (Dainty and Toksöz, 1981), possibly due to the lack of water in the lunar interior to dampen the seismic signal (Evans et al., 2014; Tittmann et al., 1980). Because the energy is so intensely scattered, it hides all but the first direct arrivals, making traditional terrestrial seismic analysis approaches challenging.

To overcome the challenges of working with the lunar data, many studies make use of their repeated nature. Individual deep moonquakes from a nest are aligned and combined to form stacks to amplify coherent seismic phases and suppress noise (Bulow et al., 2005; Nakamura, 2003; Lognonné et al., 2003; Yuan et al., 2021). Even when the coherent seismic phases are amplified in the stacked data, the arrival times picked by different researchers can vary by up to ∼10 seconds for the arrival of the P-arrivals and ∼ 4 seconds for the S-arrivals (Nunn et al., 2020b). For comparison, the uncertainty on arrival times for earthquakes, are nearly always < 1 second (Chang et al., 2017; Sippl et al., 2013; Chang et al., 2017). The uncertainty of arrival times increases the uncertainty of deep moonquake locations and imaging of the lunar interior.

1.3.3 Setting of repeating deep moonquakes

Repeating deep moonquakes rupture faults that are deep in the lunar interior, as illustrated by the red dots in Figure 1.10. Here, I provide a brief description of the lunar structure. To understand the structure of the interior of the Moon, geophysical observations have been made from Earth, from spacecrafts in orbit, and in situ by astronauts on the surface of the Moon. These include lunar laser ranging studies carried out from the surface of the earth (Williams et al., 2006) and from orbit (Matsuyama et al., 2016; Zuber et al., 2012), remote gravity (Williams et al., 2014) and magnetic field observations from orbit (Shimizu et al., 2013), and geochemical and petrological analysis of returned samples (Che et al., 2021; Tartèse et al., 2019). But the highest resolution geophysical method to image the lunar interior uses the signals from deep moonquakes recorded on the Apollo instruments

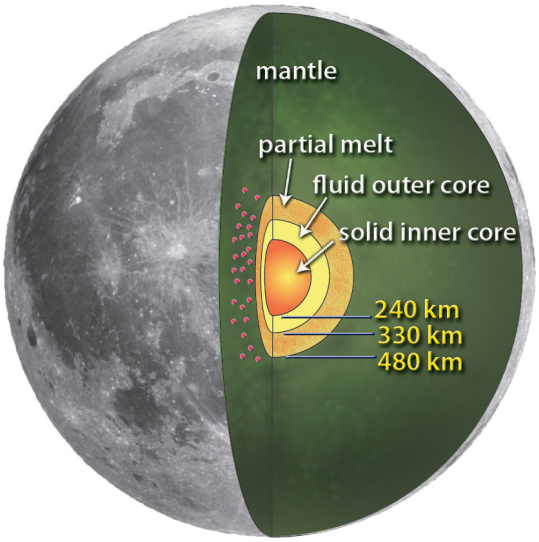


Figure 1.10: structure of the interior of the Moon. Deep moonquake nests are illustrated as red dots. Figure from Weber et al. (2011).

placed on the surface of the Moon (e.g., Garcia et al., 2019; Nakamura et al., 1982). Yet, due to the characteristics of the seismic signals and the small seismic network, the lunar interior still remains highly uncertain.

These geophysical observations suggest that just like Earth, the Moon is a differentiated planetary body, with a crust, mantle, and core. The crust is highly fractured, and is around 20 km thicker on the farside (Wieczorek et al., 2013). The uppermost layer of the moon (the "megaregolith") is very heterogeneous and consists of fragmented eject blocks and a highly fractured material (Blanchette-Guertin et al., 2012). The depth to which the heterogeneity and "megaregolith" extends ranges from a few hundreds of meters (Latham et al., 1972) up to 200 km (Gillet et al., 2017).

Beneath the crust is the lunar mantle, where deep moonquakes occur. the lunar mantle is homogeneous to first-order (Nakamura, 1983; Garcia et al., 2012; Lognonné et al., 2003), although some lateral heterogeneity in the deep moonquake source region may be present (Qin et al., 2012; Zhao et al., 2008; Nakamura, 1983). Deeper in the mantle, recent reanalysis of the Apollo era seismic data suggests an attenuating layer at around 1000 km, just beneath the deep moonquake generating region (Figure 1.10, Weber et al., 2011; Nakamura, 2005a). Diving again deeper, the Moon has an iron-rich core with a radius of 250 - 430 km (Weber

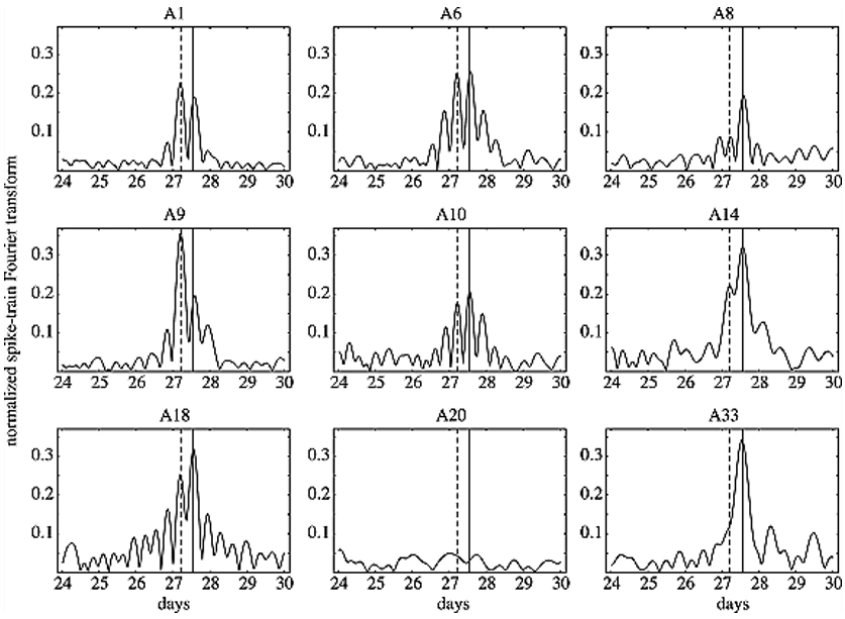


Figure 1.11: Fourier amplitude spectra of the occurrence times of 9 deep moonquake nests from Bulow et al. (2007). Most spectra have a peak around ∼27 days.

et al., 2011). Neither strong convection nor plate tectonics presently operate on the Moon (Watters et al., 2010). As such, any present-day deformation related to non-tidal stresses (which here we group as "tectonic") may provide insight into the history and formation of the Moon.

1.3.4 Open questions about deep moonquakes

Although the signals generated by deep moonquakes are key to understanding the lunar interior, why and how deep moonquakes occur remains a mystery. Here I outline some open questions about deep moonquakes.

What is the relationship between deep moonquakes and the tidal stress?

The first open question is the relationship between deep moonquakes and tidal stresses. The monthly periodicities of most moonquakes suggest that they are at least partly excited by tidal stresses. Each nest has its own characteristic periodicity controlled by one or more of the orbital periods, as illustrated by the peaks in the Fourier spectra in Figure 1.11 (Bulow et al., 2007). Longer period modulations

in moonquake periodicity of 206 days and 6 years are controlled by tidal effects from the sun (Bulow et al., 2007).

Although most moonquake nests are at least weakly periodic (Frohlich and Nakamura, 2007), it is still unknown if these deep moonquakes are driven by tidal stresses alone or if the tides act as a triggering mechanism on top of some long-term non-tidal ("tectonic") stress.

There have been two approaches to understanding the relationship between deep moonquakes and tidal stress in the literature: tidal modelling and seismological observations.

The first approach is to model the tidal stress tensor at the deep moonquake location (e.g., Toksöz et al., 1977; Cheng and Toksöz, 1978). In an elastic model of the Moon, there is a broad peak in the modelled tidal shear stress at a depth between 600 - 1000 km – coincident with the deep moonquake hypocentres (Toksöz et al., 1977; Cheng and Toksöz, 1978). Yet researchers struggle to consistently correlate moonquake occurrence times with individual stress components (Toksöz et al., 1977; Minshull and Goulty, 1988). In recent examples, Weber et al. (2009) and Araki (2001) search for a fault plane where the maximum tangential stress or stress rate coincides with deep moonquake occurrence. But for many nests, no suitable fault plane can be identified. Additionally, the modelled tidal stress is small compared to the overburden. The poor correlation and small magnitude of the tidal stress suggest that a large tectonic stress may be important in driving deep moonquakes (Goins et al., 1981).

Alternatively, the influence of the tidal stress may be inferred from seismic evidence. Ideally, we would use the first motions of the moonquake waveforms to determine fault plane solutions and then project the stress onto the fault plane of each moonquake. However, as highlighted in Section 1.3.2, many aspects of the lunar data make it challenging to determine the fault plane solutions directly from seismic data. As yet, there is no robust fault plane solution for deep moonquakes. Other seismic analysis has been more successful. Kawamura et al. (2017) find the stress released in a deep moonquake comparable to the tidal stress, suggesting that

the deep moonquakes could represent the cyclic build-up and release of tidal energy without the requirement for additional tectonic stress. Similarly, from P-S ratios and S wave polarisation, Nakamura et al. (1977) find a change in the slip direction with time, only possible if a large tidal stress generates deep moonquakes.

Much of the discussion about the stresses that drive deep moonquakes focuses on some deep moonquakes that appear to slip backwards i.e., in the opposite direction to other events from the same nest (Nakamura, 1978; Frohlich and Nakamura, 2009). Their waveforms are very similar but flipped compared to the waveforms of the other events. While some researchers suggest that to generate events with a reversed polarity waveform would require a tectonic stress, others suggest the tidal stress alone may create the flipped waveforms (Toksöz et al., 1977; Weber et al., 2009; Nakamura et al., 1980; Nakamura et al., 1977). Understanding these reversed polarity deep moonquakes is the focus of Chapter 3 of this thesis.

Are there farside deep moonquakes?

Locating deep moonquakes remains a challenge due to the waveform characteristics (see Section 1.3.2). Of all the deep moonquake nests that have been located, most are on the near side of the Moon – the same side of the Moon as the Apollo seismic instruments. Only 8 nests are located with certainty on the farside of the Moon (Nakamura, 2005a). No deep moonquakes have been located with certainty within 40 degrees of the antipode.

One possible explanation for the lack of observed deep moonquakes is that the farside is aseismic. This would imply that the lunar interior is structurally and dynamically asymmetric. Such a hypothesis is plausible, especially due to crustal dichotomies observed on the Moon. The crust on the farside is almost 20 km thicker than the nearside (Wieczorek et al., 2013) and lacks the dark mare basalts and heat-producing elements of the nearside (Lawrence et al., 2003).

Alternatively, researchers may simply not have identified farside deep moonquakes. Structures deep in the lunar interior could prevent us from observing deep moonquakes on the farside from the seismometers on the nearside. One proposed

structure which could be responsible for this is a highly attenuating layer at a depth of around 1000 km. This layer would effectively mask deep moonquakes within 40 degrees of the antipode (Weber et al., 2009; Nakamura, 2005a). This severe attenuation of seismic waves, along with other remote geophysical observations such as lunar ranging studies (Khan et al., 2014), may imply that this highly attenuating layer is a layer of partial melt sitting just above the lunar core.

Currently, there is no consensus on the cause of the distribution of deep moonquakes. To address this problem, in Chapter 4, I use a common statistical technique, principal component analysis (PCA), to reduce the uncertainty of deep moonquake arrival times, which is needed to improve the accuracy deep moonquake locations.

What mechanism generates deep moonquakes?

A final open question is the generative mechanism of deep moonquakes. Deep moonquakes occur between 700 – 1200 km depth, roughly halfway between the Moon's centre and its surface. This is much deeper than most terrestrial seismicity, which happens in the shallow brittle crust. At these depths, the temperatures reach 1500–1600 °C and pressures of ∼4 GPa, far below the lunar brittle-ductile transition. The high temperatures and pressure should inhibit brittle failure. It is still unknown how these events can occur below the brittle-ductile transition.

At shallow depths, rocks fail by brittle fracture or frictional sliding. At greater depths, the ductile strength of the rock is less than the brittle or frictional strength, so rocks deform in a ductile way. For deep moonquake faults to break at high pressures and temperatures, a mechanism is required to reduce the brittle strength to below the ductile strength of the rock.

Several mechanisms have been suggested to generate deep moonquakes, including those that explain deep and intermediate-depth earthquakes (>70 km depth), some of which have similar pressure-temperature conditions to deep moonquakes, as illustrated in Figure 1.12. Here, I outline some of these possible models for deep moonquake failure:

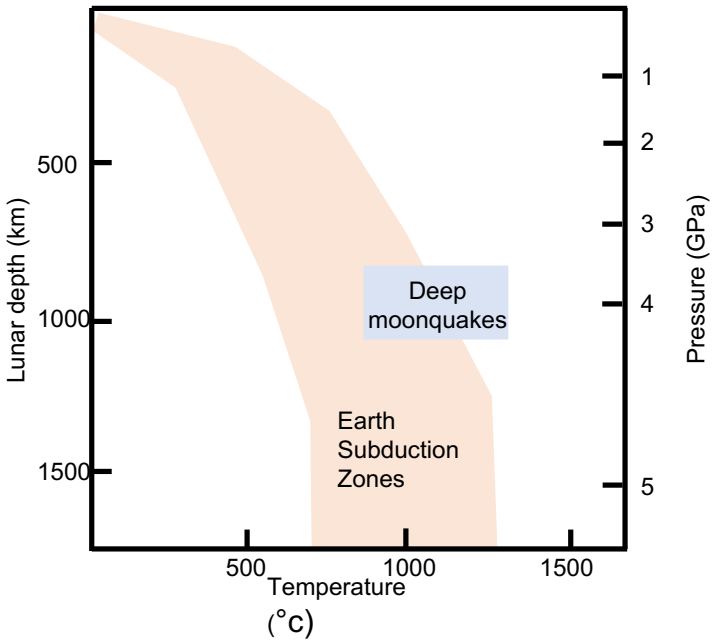


Figure 1.12: Pressure and temperature conditions of deep moonquakes compared to the pressure and temperature conditions on Earth subduction zones. Altered from Frohlich and Nakamura (2009).

Phase Change A first mechanism suggested for intermediate-depth earthquakes, which may also operate deep in the Moon, is a volume change associated with a mineralogical phase change leading to faulting (e.g., Kirby et al., 1996; Kirby, 1987; Green and Burnley, 1989; Burnley et al., 1991; Schubnel et al., 2013), illustrated in Panel a of Figure 1.13. A volumetric component of deep moonquake failure was suggested as a possibility by Weber et al. (2009) when no plane of failure could be correlated with the peak tidal stress at the time of moonquake occurrence. However, this model is only suitable if (a) there is an appropriate phase transition in the lunar interior (pressures on the Moon are too low for the olivine-spinel transformation invoked in the Earth for deep-focus seismicity) and (b) this phase change could repeatedly happen in the same location.

Thermal runaway A second mechanism invoked for intermediate-depth earthquakes is a ductile thermal shear runaway; the fault behaves elastically rather than in a brittle way. A large initial shear stress and a small increase in strain

rate lead to heating, runaway weakening and failure (Figure 1.13b, Ogawa, 1987; Karato et al., 2001; Kelemen and Hirth, 2007; John et al., 2009; Thielmann et al., 2015; Thielmann, 2018). For this mechanism to operate on the Moon, large initial stresses would be required to start the runaway process.

Fluids A third mechanism invoked for intermediate-depth seismicity is increased pore fluid pressure. An increase in pore fluid pressure decreases the effective normal stress, which allows for brittle failure at greater depths (e.g., Davies, 1999; Meade and Jeanloz, 1991; Hacker et al., 2003; Proctor and Hirth, 2015; Brantut et al., 2011; Dobson et al., 2002), as illustrated in Figure 1.13c. On Earth, these fluids are related to the dehydration reaction of minerals as they descend to great depths in subduction zones. On the Moon, the source of fluid is less clear, as the interior of the Moon is dry compared to the Earth (Evans et al., 2014). But as discussed in Section 1.3.3, the deep moonquakes lie just above a region of partial melt, leading Frohlich and Nakamura (2009) to suggest that deep moonquakes may be related to the pumping of partial melt or fluids between favourably oriented cracks.

Smooth faults and strain weakening Alternatively, there may be some generative process unique to the Moon. Frohlich and Nakamura (2009) suggest that the deep moonquake faults may be weakened by slip over repetitive cycles – similar to the strain weakening that occurs in metals. Similarly, observations of the seismic spectra (Kawamura et al., 2017) suggest that lunar faults may be much smoother than their terrestrial counterparts. Although this process may allow current lunar faults to slip under high confining pressures and small tidal driving stresses, some other mechanisms or processes would be required to create the pre-existing fault that deep moonquakes rupture along initially.

Stress concentrations in the lunar interior Finally, the rupture of deep moonquakes may be directly related to the interior structure of the Moon – just as intermediate-depth earthquakes occur in the subducting slab. Although 1-D seismic profiles suggest that the interior of the Moon is homogeneous, isotope analysis

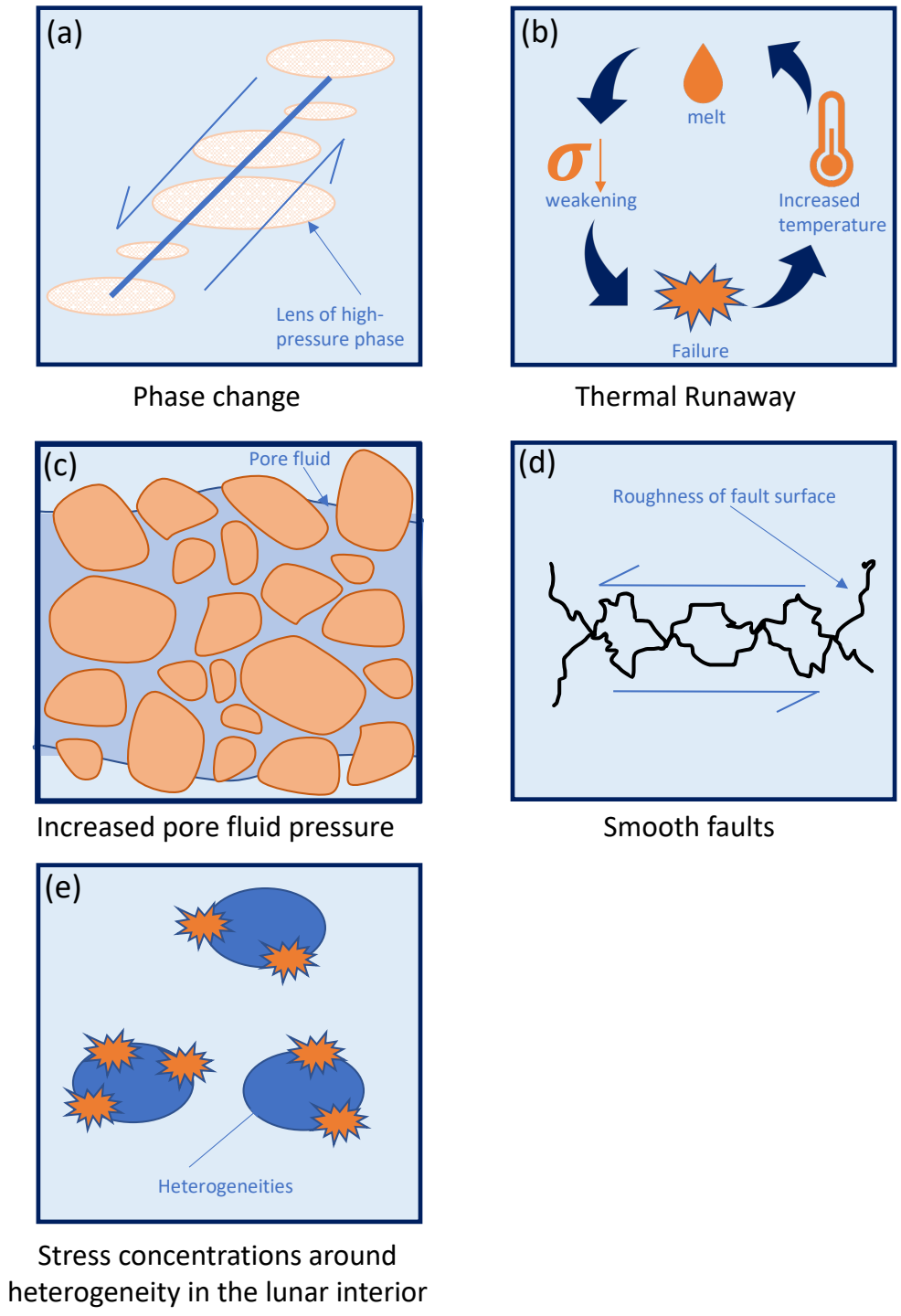


Figure 1.13: Possible mechanisms to allow for brittle failure at high pressures and temperatures deep in the Moon.

and primitive seismic tomography suggest that the lunar interior could have large heterogeneities, possibly concentrating the tidal stresses (Khan et al., 2000). The heterogeneity alone cannot generate slip under high pressures and temperatures but coupled with another mechanism described above, the heterogeneity may play an important role in generating deep moonquakes.

1.4 Thesis road map

This thesis focuses on two types of repeating earthquakes; in Parkfield and deep in the Moon.

In **Chapter 2**, I aim to understand why small magnitude repeating earthquakes in Parkfield happen less often than expected. I test a recent model that proposes that partial ruptures can account for the observed scaling between moment and recurrence time. I use a simple, fast and effective location-based method previously used by Williams et al. (2019), to identify repeating earthquakes and partial ruptures. In this chapter, I address two specific aims:

1. To use a simple location-based method to identify repeating earthquakes and partial ruptures.

2. To test if partial ruptures can explain why small magnitude repeating earthquakes occur less often than we expect.

In **Chapter 3**, I use deep moonquake observations to constrain the tectonic stress near the A01 moonquake nest. I focus on a subset of deep moonquakes which appear to slip backwards (Nakamura, 1978; Frohlich and Nakamura, 2009). I present two models for these backwards slipping events: there could be a large tectonic stress driving deep moonquakes that varies in space or a large tidal stress that changes in time. To discriminate between these two possibilities, I use principal component analysis of waveforms of deep moonquakes. In this chapter, I address three specific aims:

1. To apply principal component analysis to deep moonquake waveforms from a single nest.

2. To determine if deep moonquakes are driven by a tidal or non-tidal ("tectonic") stresses.

3. To discriminate between possible mechanisms that could generate deep moonquakes.

In **Chapter 4**, I continue to use principal component analysis to improve estimates of P-wave and S-wave arrival times, which are key for inversions of velocity structure and source location. The waveform characteristics of lunar events make picking arrival times challenging. To improve the relative arrival times, I align the waveforms using principal component analysis. In this chapter, I address two specific aims:

1. To use principal component analysis to align waveforms.

2. To improve the relative time-shifts between deep moonquakes across nests within the Moon.

Finally, the main results of this thesis and proposed future research directions are summarised and discussed in Chapter 5.

2

Searching for partial ruptures in Parkfield, California

Contents

2.1 Introduction 31
2.2 Predictions from rate and state models 33
2.3 Finding repeaters and partial ruptures 34
2.3.1 Identifying repeating earthquakes 36
2.3.2 Identifying partial ruptures 37
2.4 Results 37
2.4.1 Analysing repeating earthquakes and partial ruptures . 39
2.4.2 Moment-recurrence scaling 42
2.4.3 Testing for bias in analysis 44
2.5 Discussion 47
2.5.1 Partial rupture slip budget and repeater recurrence intervals 47
2.5.2 How big are repeaters relative to their nucleation size R_∞? 47
2.5.3 Compatibility of observations with the model 48
2.6 Conclusion 49

Abstract

Repeating earthquakes frequently rupture the same seismic asperities that are loaded to failure by surrounding aseismic slip. They occur less often than expected if these earthquakes accommodate all of the long-term slip on the fault, creating a slip deficit. Recent crack models using rate-and-state friction suggest a possible explanation: for small events, a larger amount of the long-term slip on the asperity is aseismic. For larger events where most of the slip budget is seismic, the asperity experiences partial ruptures. We aim to test the predictions of this model of repeating earthquakes by searching for the proposed partial ruptures using the Northern California earthquakes catalogue. The presence of partial ruptures suggests that asperities of repeating earthquakes are much larger than the nucleation size. We find that partial ruptures account for $\sim$ 5- 40% of the long term slip on the fault, but when we consider the slip in repeating earthquakes and partial ruptures, it still does not accommodate all of the long term slip on the fault. A different model may be required to explain the slip deficit of repeating earthquakes.

Plain Language summary

Repeating earthquakes frequently occur on the same patch of the fault. They are thought to happen on locked patches of fault which are surrounded by parts of the fault that are moving slowly. Thus, the slowly moving parts of the fault load the patch to failure, and we therefore expect the slip in an earthquake to match the slip on the surrounding fault. But this is not the case – there is a slip deficit between the seismic slip and long term slip on the fault. This slip deficit means the time between earthquakes is longer than expected. We explore whether some of the slip deficit is explained by slip happening in smaller earthquakes ("partial ruptures") between the time of the larger magnitude repeating earthquakes. We choose to search using the Northern California earthquakes catalogue, which contains many well-located repeating earthquake sequences. Although we find lots

of partial ruptures, which can account for up to 40% of the slip on the fault, it is still not enough to account for the total slip deficit.

Key Points

- We search for partial ruptures of repeating earthquakes in Parkfield, California.
- We find partial ruptures, which suggests repeating earthquake asperities are many times larger than the nucleation size.
- Repeating earthquakes and partial ruptures do not accommodate all of the long-term slip.

2.1 Introduction

Repeating earthquakes rupture the same asperity on a fault time and time again, with surprisingly regular recurrence intervals. They are identified by their co-located rupture patches, equal magnitudes and waveform similarity (Uchida and Bürgmann, 2019; Gao et al., 2021; Waldhauser and Schaff, 2021). Repeating earthquakes represent locked asperities on a fault, which are loaded to failure by the surrounding fault creep (Beeler et al., 2001). In this simple framework, the recurrence time between repeating events seems intuitive; if the asperity is locked between earthquakes, the slip in each earthquake (S) should match the surrounding fault creep (V_{creep}) that has been loading the asperity in the time since the last event (T_r): $S = V_{creep}T_r$. To relate the recurrence interval to the moment of an earthquake, we can use $M_0 \propto \Delta\sigma R^3$, where $\Delta\sigma$ is the stress drop and R is the radius of the asperity. If the stress drop and creep rate are constant then the slip in each event is linearly related to the asperity radius ($S \propto R$), and we find that the recurrence interval should scale with the moment as $T_r \propto M_0^{1/3}$.

However, the recurrence interval of repeating earthquakes is longer than we expect if we assume they have a constant stress drop, constant creep rate and the asperity is locked between repeating earthquakes. Instead, observed global repeater recurrence intervals scale with moment as $T_r \propto M_0^{0.17}$ (Nadeau and Johnson,

1998; Chen et al., 2007). The observed seismic slip in the repeating earthquakes is less than the long-term slip on the surrounding fault, creating a slip deficit. This slip deficit is greatest for small earthquakes – for a M_w=1 earthquake, the seismic slip required to match the long term geodetic slip is an order of magnitude larger than the observed seismic slip.

The difference between the observed and theoretical scaling implies that we still do not fully understand the process that controls the recurrence interval of repeating earthquakes. Yet the recurrence time of repeating earthquakes is often used to track the slip rate of the creeping faults that host them (e.g., Waldhauser and Schaff, 2021; Uchida and Bürgmann, 2019).

To understand the observed moment-recurrence scaling, researchers have proposed a range of physical models. The first set of models eliminate the assumption of a constant stress drop; to match the geodetically observed slip rate in Parkfield and recover the $T_r \propto \mathrm{M}_0^{0.17}$ scaling, the stress drop would have to be inversely proportional to the 1/4 the power of seismic moment (Chen et al., 2007). In this case, very small repeating events could have very high stress drop ($\sim$2 GPa Sammis and Rice, 2001). However, observations of repeating earthquakes show magnitude independent stress drops with a median value of 7 MPa, and a range of $\sim$1-100 MPa (Abercrombie, 2014; Imanishi et al., 2004; Allmann and Shearer, 2007). Dreger et al. (2007) and Kim et al. (2016) attempt to reconcile these two observations with heterogeneous stress on the fault. They find a localised high stress drop which matches the requirements of the model (Nadeau et al., 1994), while the average stress drop over the whole asperity is low.

The second set of models eliminate the assumption that the creep rate is constant. A locally lower creep rate could be created by a boundary effect along the border between locked and creeping sections of the fault (Sammis and Rice, 2001). However, the common occurrence of repeating earthquakes is hard to reconcile with the specific geometrical constraints of this model – in Parkfield, 55% of all earthquakes are repeating (Nadeau et al., 2004). Instead, Williams et al. (2019) suggest the creep rate may vary with fault length. Individual fault strands of different sizes follow

the expected $M_0^{1/3}$ scaling, but when averaged across fault strands of different sizes, the observed $M_0^{0.17}$ scaling is recovered. However, fewer observations support this more recent model compared to those described above.

A final set of models eliminate the assumption that the asperity is locked between repeating earthquakes. Repeating earthquakes could have prolonged recurrence intervals because some of the slip on these asperities accumulates aseismically or via smaller ruptures occurring on the same asperity ("partial ruptures") in the time in between the repeating earthquakes (Chen and Lapusta, 2009; Chen and Lapusta, 2019; Cattania and Segall, 2019; Cattania, 2019; Barbot, 2019). We regularly see only the partial rupture of locked faults around the world (e.g., Ruiz et al., 2014; Konca et al., 2008; Qiu et al., 2016; Uchida et al., 2012). Intuitively, these partial ruptures can account for a part of the slip budget of the fault.

2.2 Predictions from rate and state models

In this study, we focus on a model where the asperity is not locked between events but can slip aseismically or release some energy as smaller earthquakes between the larger characteristic repeating events. This behaviour has been modelled, most recently using the rate and state friction framework (Cattania, 2019; Cattania and Segall, 2019; Chen and Lapusta, 2009; Chen and Lapusta, 2019; Barbot, 2019). Using a small fault asperity governed by steady-state velocity-weakening friction, which is surrounded by a much larger velocity-strengthening region, these models recover the $M_0^{0.17}$ scaling. In particular, we focus on the model of Cattania and Segall (2019). In this model, the behaviour of the repeating earthquake depends on the size of the asperity radius relative to the size of the smallest asperity that can host a seismic event (called the "nucleation radius", R_∞):

- For small repeater asperities ($R_\infty \leq \mathrm{R} \leq 2R_\infty$), creep erodes the asperity. When the creep front reaches the middle of the asperity, an earthquake initiates from the centre and ruptures the entire asperity. Aseismic slip makes up 30 - 80% of the total slip on the patch.

- For repeater asperities with $2R_\infty \leq \mathrm{R} \leq 4.3R_\infty$, the creep does not erode the whole asperity. Earthquakes initiate on the edge of the asperity and rupture the entire asperity. Aseismic slip makes up 20 - 30% of the total slip on the patch.

- For repeater asperities with $\mathrm{R} \geq 4.3\mathrm{R}_\infty$, the asperity experiences small earthquakes between complete ruptures that do not rupture the entire asperity ("partial ruptures"). A complete and partial rupture from simulations of Cattania and Segall (2019) are illustrated in Figure 2.1. Aseismic slip makes up 10 - 20% of the total slip on the patch.

In each regime, the scaling is recovered by relaxing the constraint that the asperity is locked between events.

This model has testable predictions which will allow us to determine the size of these repeating earthquakes relative to the nucleation size, and explain the slip deficit. As the radius of the repeating earthquake asperity increases, so does the seismic moment ($M_0 \propto \Delta\sigma R^3$). With increasing repeater moment, we expect to observe a transition from the regime where partial ruptures are not present to a regime where a large portion of the slip budget is made up of partial ruptures. When $\mathrm{R} = 4.3R_\infty$, we expect the lower bound on ratio of repeater moments to partial moments to be $\sim$0.7 (see Appendix A.1 for the derivation of this lower bound). As the moment of the repeater further increases, the seismic slip is closer to the long term geodetic slip rate, and the slip deficit decreases, and as such, as the moment of the repeater further increases, the ratio of repeater moments to partial moments decreases. By $\mathrm{R} = 100\ R_\infty$ the minimum ratio of repeater moments to partial moments is $\sim$0.2.

2.3 Finding repeaters and partial ruptures

We test the model from Cattania and Segall (2019) by searching for repeating earthquakes and partial ruptures in Parkfield, California. We consider two repeating

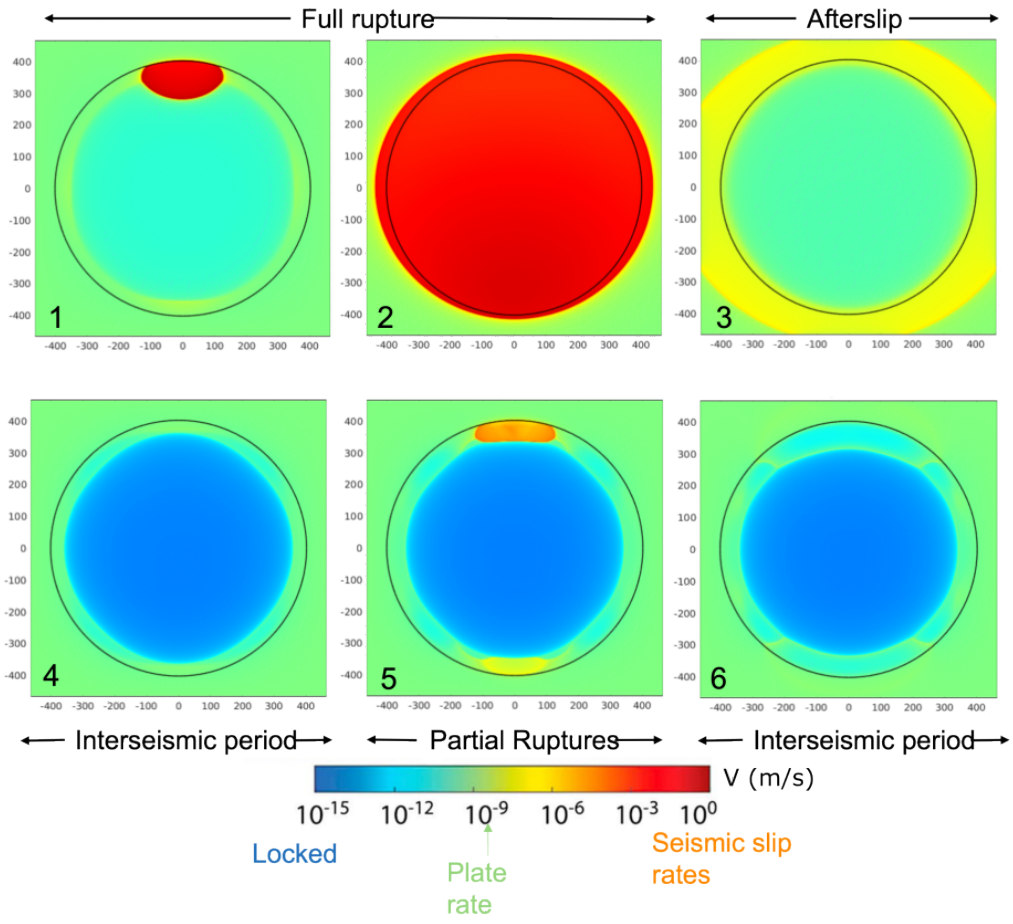


Figure 2.1: Example of full and partial ruptures from simulations. The top lines shows an example of a full rupture on an asperity of size R = $8R_\infty$, from Cattania and Segall (2019). The colour indicates the slip speed. In this model, an event nucleates and ruptures the entire asperity. In the interseismic period, the asperity is locked. A creep front slowly erodes the asperity. In the bottom row, a partial rupture nucleates, and then the asperity is locked again.

earthquake catalogues. First, we use a simple approach to identify pairs of co-located earthquakes without waveform correlation. We take advantage of the high-quality earthquake locations already obtained in this area (Waldhauser and Schaff, 2008) and identify co-located earthquakes as pairs of earthquakes located within one rupture radius of each other. Second, we use a more sophisticated and extensive repeater catalogue created using waveform correlation by Waldhauser and Schaff (2021). In this catalogue, repeating earthquakes are identified based on three criteria: (a) events are co-located within each other's circular rupture area, assuming a constant 3 MPa stress drop with a 10m uncertainty; (b) events

have magnitudes within 0.3 magnitude units of each other; (c) and events have similar waveforms in a 6 second long unfiltered time window at many stations. They must have at least one measurement of correlation coefficient of ≥ 0.95 and at least three measurements of correlation coefficients ≥ 0.9.

2.3.1 Identifying repeating earthquakes

To search for repeaters in the NCSN double-difference relocated catalogue (Waldhauser and Schaff, 2008; Schaff and Waldhauser, 2005; Waldhauser, 2013), we first select earthquakes in the 90-km-long area around Parkfield (Figure 2.2), where over 50% of seismicity occurs in repeating clusters (Nadeau et al., 2004). We analyse events between 1984 and 2021, excluding ten years after the 28^{th} September 2004 M_w 6 Parkfield earthquake; this large magnitude event affects the moment and recurrence interval of repeating sequences (Chen et al., 2010; Chen et al., 2013). The analysed catalogue contains 7590 events with magnitudes between M_w -0.3 and 4.9.

We calculate each event's moment (M_0) from the magnitudes reported in the NCSN catalogue (M) assuming $M_0 = 10^{1.2M+10.15}$ (Wyss et al., 2004). We then estimate the ruptures' radius. The radius, R, of of a circular crack with uniform stress drop (Eshelby, 1957) is given by:

$$R = \left(\frac{7}{16}\frac{M_0}{\Delta\sigma}\right)^{\frac{1}{3}}. \tag{2.1}$$

In our primary analysis, we assume a stress drop $\Delta\sigma$ of 10 MPa, as has been inferred for events in the Parkfield region (Abercrombie, 2014; Allmann and Shearer, 2007; Imanishi and Ellsworth, 2006), though we check later that we obtain similar results with a 3 MPa stress drop (Section 2.4.3).

To search for repeating earthquakes, we cut the catalogue at the magnitude of completeness (M_w 1.1) to identify mostly complete repeating pairs, without too many missed events. We then search for earthquakes whose catalogue locations are within one rupture radius horizontally as well as vertically. A repeating earthquake is initially identified as any earthquake with another event within one radius and a magnitude within $\pm$ 0.3 magnitude units. However, we remove repeater pairs

separated by only a short interval: less than 50 days (as shown in Figure 2.4). These pairs are likely to be triggered events, not true repeating earthquakes.

2.3.2 Identifying partial ruptures

Our search of the NCSN catalogue reveals 3991 individual repeating events grouped into 23185 unique pairs. We also have 2976 repeating earthquakes from the Waldhauser and Schaff (2021) catalogue, grouped into 612 sequences. We search for partial ruptures of each of these earthquakes. For each identified repeating earthquake, we search the entire catalogue (without truncating at M_w 1.1) for events within one radius but with a magnitude at least 0.3 M_w units smaller.

We account for the catalogue location error in two ways. First, we consider an 80-m uncertainty on the horizontal location and a 97-m uncertainty on the vertical location; these uncertainties are the 90% confidence limits for relative location errors in the combined relocated and real-time catalogues. This lenient constraint will include many earthquake pairs that may not be co-located, including small triggered events, providing an upper bound on the number of repeating earthquakes and partial ruptures.

Second, we use the location error ellipse reported in the NCSN catalogue for each event pair. We compute the maximum distance between the two earthquakes that is allowed given the 95% error ellipse. Repeaters and partial ruptures are only identified if this maximum distance between a pair of events is within one rupture radius, ensuring events are co-located. This more time-consuming approach provides a lower bound on the number of repeating earthquakes and partial ruptures.

2.4 Results

Now that we have two collections of repeating earthquakes and partial ruptures, we can analyse their numbers and timing.

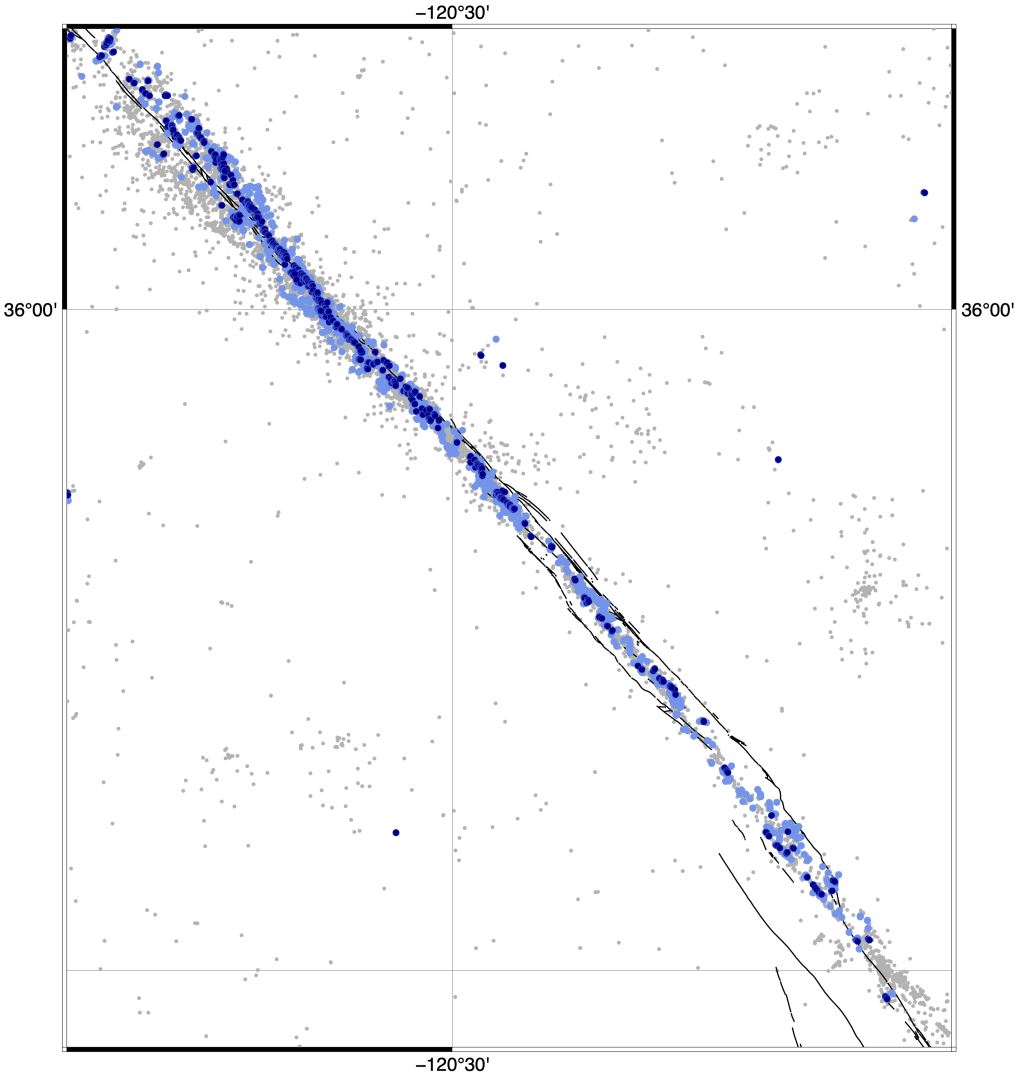


Figure 2.2: Seismicity of the Parkfield region. Grey dots show the events in the Northern California seismic network double-difference relocated catalogue. Dark blue events are repeating earthquakes identified by Waldhauser and Schaff (2021). Light blue events are repeating earthquakes identified in this study. Faults plotted from the USGS Quaternary faults and folds database.

2.4.1 Analysing repeating earthquakes and partial ruptures

We begin with the 3991 individual repeaters, identified in pairs from the relocated NCSN catalogues. These events have 4468 partial ruptures. We do not identify these events into unique sequences, but consider each repeater and all of its co-located events. Using the Waldhauser and Schaff (2021) catalogue, we find 2976 repeating events and 2463 partial ruptures.

In our initial analysis, we plot the time between successive repeating earthquake pairs – the recurrence interval– against the pair's average moment (Figure 2.4a). Then we bin the pairs by moment and calculate the median recurrence interval in each moment bin. We estimate the uncertainty of these median recurrence intervals using a bootstrapping approach. In each of the 1,000 bootstrap iterations, we resample the events with replacement and recompute the median recurrence interval in each bin (black bars in Figure 2.4a). Finally, we perform a linear regression between the log recurrence interval and the log moment, where each recurrence interval estimate is down-weighted by the number of events in each bin. The best-fitting line implies that the recurrence interval $T_r \propto M_0^{0.18}$, with 95% confidence limits on the exponent of 0.17 and 0.19, similar to previous estimates in the Parkfield region (Nadeau and Johnson, 1998) and elsewhere (Chen et al., 2007).

Figure 2.6a shows the scaling between the recurrence interval and moment of the identified repeating earthquake sequences from the Waldhauser and Schaff (2021) catalogue. The best-fitting moment-recurrence scaling is $T_r \propto M_0^{0.15}$, with 95% confidence limits on the exponent of 0.14 and 0.26. The scaling is shallower than observed when using repeaters from the NCSN catalogue.

Next, we analyse all earthquakes that occur within one radius, including similar-magnitude repeating events and smaller magnitude partial ruptures. Note that since we analyse each repeating earthquake and all of its co-located events, we effectively analyse some earthquakes more than once.

Figure 2.3 illustrates 4 examples of repeaters and all of their co-located events. The repeating earthquakes are coloured in blue, and the smaller-magnitude partial

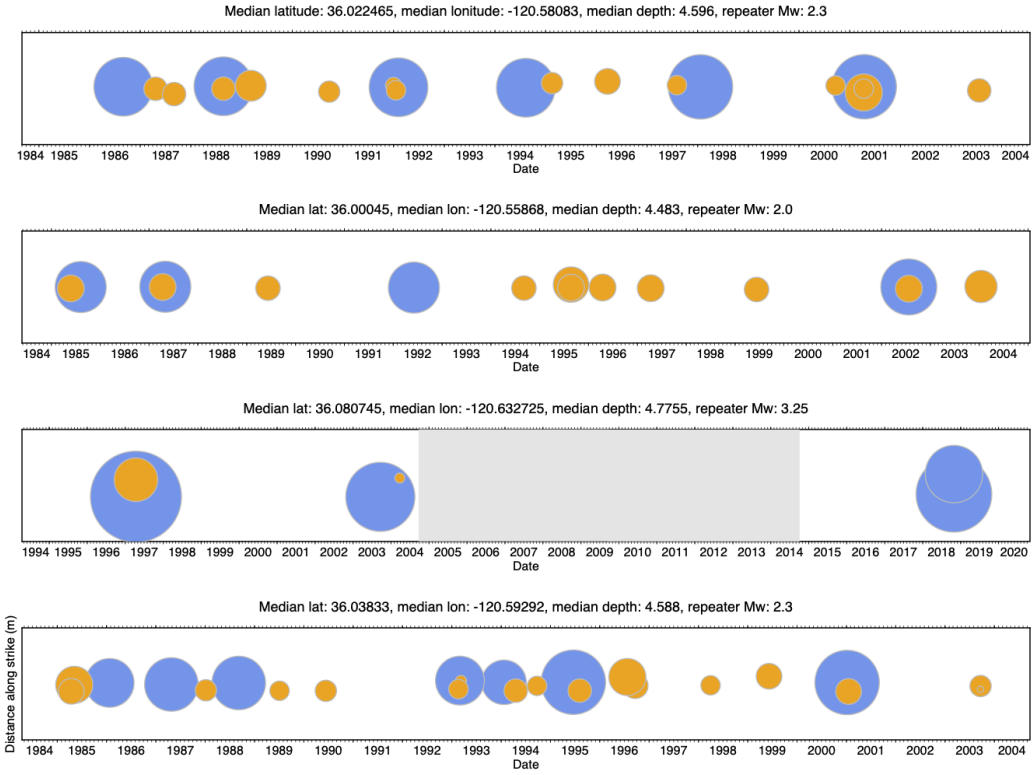


Figure 2.3: Examples of repeaters and all of their co-located events, made up of partial ruptures and repeating earthquakes. Repeating earthquakes are plotted in blue and partial ruptures in orange. The median latitude, longitude and magnitude of repeating earthquakes are printed at the top of each panel. The grey box in the third panel is the ten years after the September 28^{th} 2004 M_w 6.0 earthquake, which is excluded from this study.

ruptures are in orange. The grey box in Panel 3 blocks out the ten years after the 28^{th} September 2004 M_w 6 Parkfield earthquake, which was removed from this study.

We would now like to systematically compare the moment accumulated in repeating earthquakes to the moment accumulated in partial ruptures. In Figure 2.4b we compare the total moment in each repeater and co-located events with the same magnitude (other repeaters) to the total moment of in each repeater and all of its co-located events (with the same magnitude or smaller i.e., repeating earthquakes + partial ruptures). Each purple dot is the sum of the magnitude in a group of events made up of each repeater and its co-located events, coloured by the median magnitude of the repeaters. The light pink dots are the median average in each magnitude bin. The total moment accumulated in repeating earthquakes

is similar to the moment accumulated in both the repeating earthquakes and partial ruptures. Therefore, the median moment in partial ruptures seems to be small compared to the total moment in each group of earthquakes made up of a repeater and all of its co-located events.

However, we note that some repeaters have very few partial ruptures, such as Panel 3 in Figure 2.3. We are likely missing small-magnitude partial ruptures that are not detected. To account for these missing earthquakes, we estimate and then correct for the NCSN catalogues detection bias as a function of magnitude. We compute the magnitude distribution of the NCSN catalogue in the Parkfield region and note that it follows a linear Gutenberg-Richter relationship with a b value of 0.97 above the magnitude of completeness of M_w 1.1 (Figure A.7). We hypothesise that this distribution extends to at least $M_w = -0.5$, which is the smallest partial rupture likely to contribute a significant moment. We therefore use the observed Gutenberg-Richter distribution to compute a theoretical cumulative moment for each magnitude M_{cut} of interest: the expected moment between $M_w = -0.5$ and $M_w = M_{cut}$. We also compute the moment in all observed earthquakes between $M_w = -0.5$ and $M_w = M_{cut}$. These theoretical and observed moment distributions are illustrated in Figure A.8. The ratio of the observed to the theoretical moment is a detection ratio: the fraction of the moment detected in each magnitude range. We can therefore use the detection ratio as a simple correction for the moment in undetected partial ruptures. If we analyse repeaters with magnitude M_{rep}, the maximum magnitude partial rupture is $M_{rep} - 0.3$. We then take the correction ratio between $M_w = -0.5$ and $M_w = M_{rep} - 0.3$. We can then estimate the true total moment for each group of events, made up of a repeater and its co-located events, by dividing the observed moment by the detection ratio.

In Figure 2.4b, for each of these binned averages plotted in light pink, we take the repeater magnitude and divide it by the detection ratio, which is plotted as dark pink triangles. This correction adds on average around $\sim$15% to the total moment observed in partial ruptures. Therefore, even when applying the detection ratio correction for missed small magnitude events, the median moment in partial

ruptures seems to be small compared to the total moment in a repeater and its co-located events.

Figure 2.5 shows the total moment in repeating earthquakes to the total moment to partial ruptures, normalised by the number of repeating earthquakes for each repeater and its co-located events – essentially the fraction of the slip in partial ruptures in each cycle. The fraction of the moment in partial ruptures in each cycle varies from 5 - 40%.

Figure 2.6b shows the ratio of the total moment in repeaters to the total moment in each group of earthquakes, made up of a repeater and all of its co-located events, identified in the Waldhauser and Schaff (2021) catalogue. When correcting for missed small magnitude events, ∼90% the moment for each repeater and its co-located events is contained in the larger magnitude repeating earthquakes.

2.4.2 Moment-recurrence scaling

Finally, we return to the moment-recurrence interval scaling for these small repeating earthquakes in the Parkfield region. The long recurrence interval of repeating earthquakes suggests that they do not accommodate all of the long-term slip on the fault. Here, we test how much of the slip budget is accounted for by partial ruptures. In Figure 2.7, we convert the recurrence interval to a slip in repeating earthquakes per cycle. We assume that for a locked asperity embedded in a creeping fault, the slip in each earthquake (S) should match the long-term accumulated slip (V_{creep}) since the last event (T_r): $S = V_{creep}T_r$. By Assuming a long-term slip rate of 23mm/year (Nadeau and Johnson, 1998), we convert the recurrence interval to a slip per repeating sequence.

Originally, this only contained the slip in the repeating earthquakes. We then correct this to include the slip in the partial ruptures by multiplying by the ratio of the moment in repeating earthquakes to the total moment in the sequence (Figures 2.4a and 2.6a). Orange dots in Figure 2.7 show the corrected slip per repeating cycle. The best-fitting weighted slopes increase by 26% for the NCSN catalogue analysis and 25% for the analysis on the Waldhauser and Schaff (2021) catalogue.

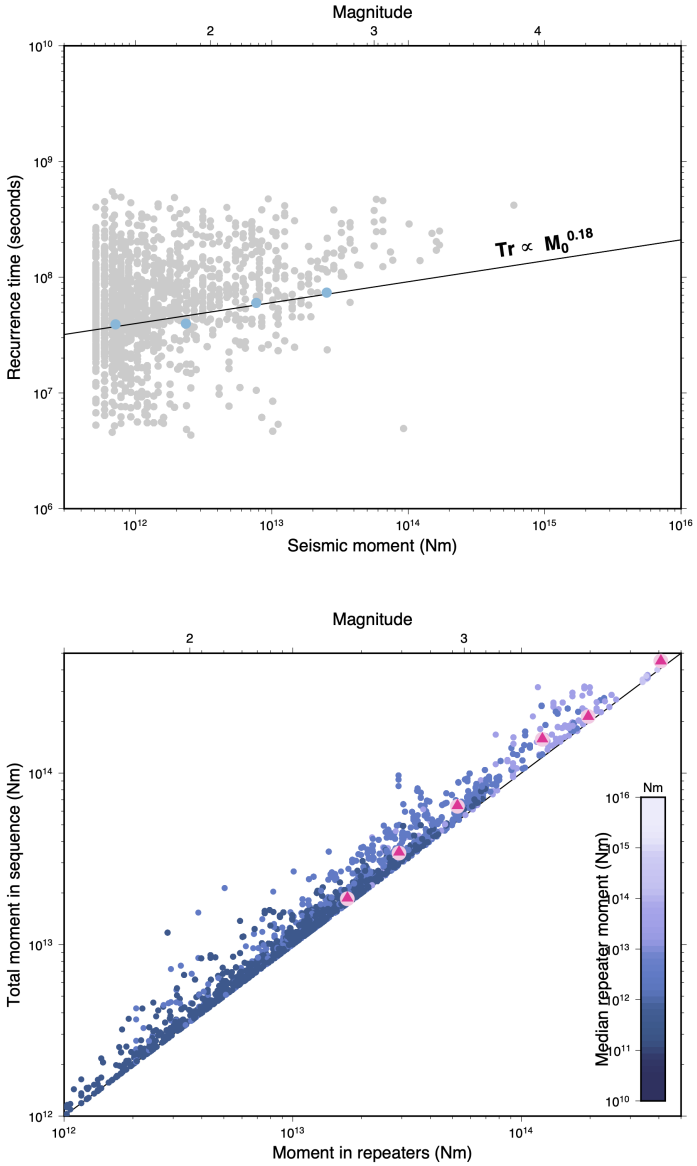


Figure 2.4: **Top:** Median recurrence interval versus median moment for pairs of repeating earthquakes from the relocated Northern California catalogue (Waldhauser, 2013) on a log-log scale. Individual values are plotted as grey circles, with medians for moment bins shown as blue circles. The error bars on the medians indicate 95% confidence limits, which were estimated via bootstrapping (details in the text). The best-fitting line is plotted in solid black with a gradient of 0.17. **Bottom:** The total moment in repeating earthquakes compared to the total moment in each group of earthquakes, made up of a repeater and its co-located events events, including repeating earthquakes and partial ruptures. Each point is coloured by the median moment of the repeating earthquake. Light pink points are the binned means. The dark pink triangles are the binned means corrected for missing small events (see text for more details).

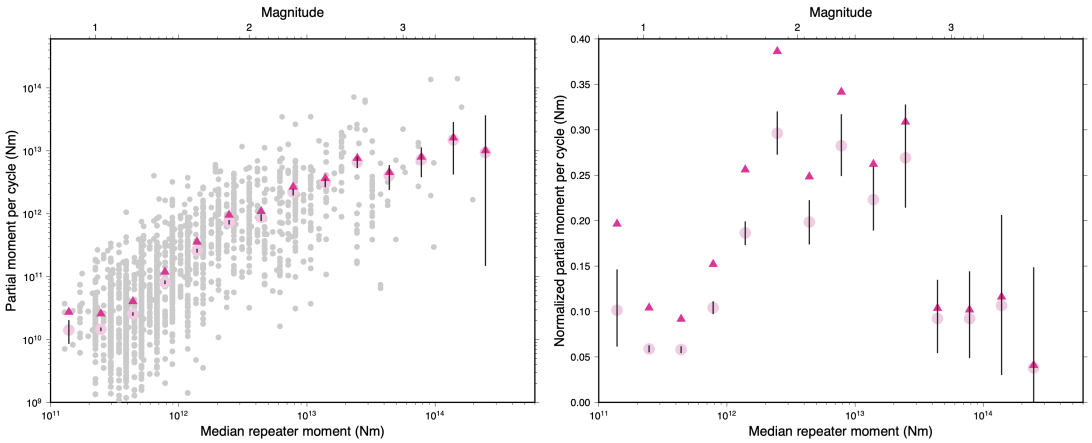


Figure 2.5: Left: Total moment in repeating earthquakes to the total moment to partial ruptures, normalised by the number of repeating earthquakes for each repeater and its co-located events. The dark pink triangles show the binned averages from bootstrapping, following the same bootstrapping procedure described in the text. The black lines show the 5^{th} and 95^{th} percentiles of these binned medians. The dark pink triangles are the corrected bin values, following the same correction described in the text. **Right:** Total moment in repeating earthquakes to the total moment to partial ruptures per cycle, normalised by the total moment in partial ruptures.

2.4.3 Testing for bias in analysis

We repeat our analysis with a range of modifications to check that our observed recurrence interval-moment scaling and identified partial ruptures are not biased by our approach. We test whether our result changes if we modify the stress drop assumed to estimate earthquake radii or the local to moment magnitude conversion (Figures A.1 and A.2). These modifications can change the slope of the recurrence-magnitude scaling by up to 20%, but we find that they do not significantly change the sum of the moment contained in partial ruptures.

We also further test the influence of the location error by estimating the minimum distance between events given the error ellipse. Our results use a fixed error bound, providing an upper limit on the number of partial ruptures. However, some events may not be co-located or are triggered events. We consider repeaters or partial ruptures with the maximum separation within the rupture radius. This reduces the number of identified repeaters and partial ruptures by ∼90%. However, the scaling relationship and the ratio of the moment in repeaters to the total moment

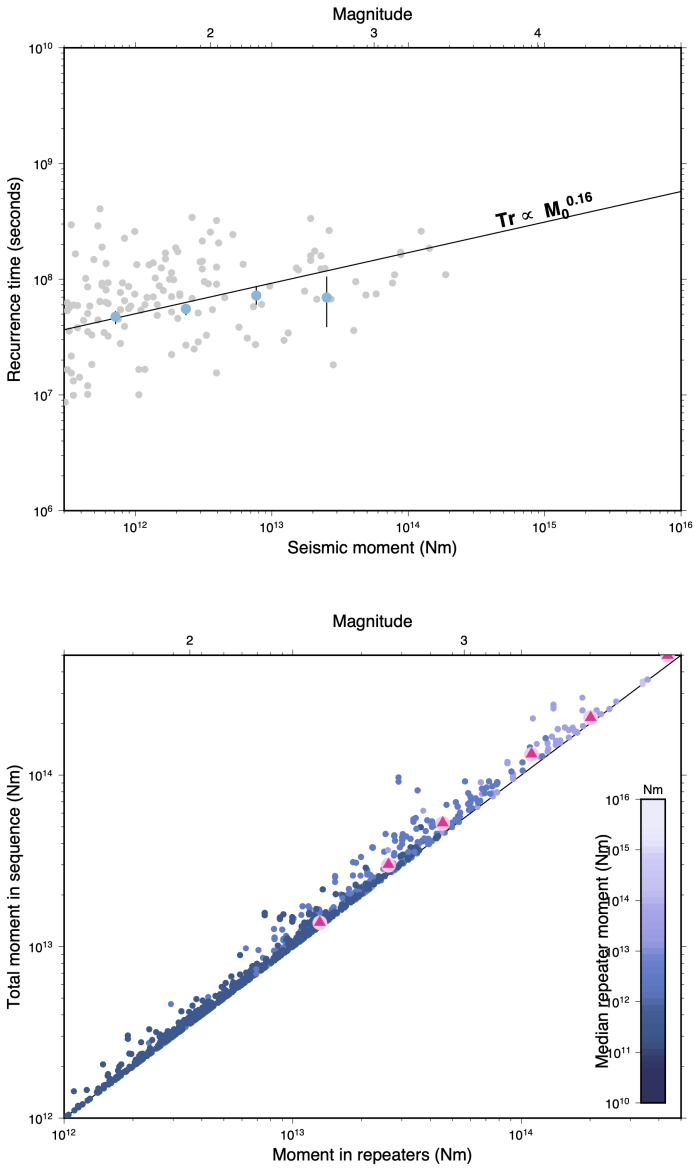


Figure 2.6: **Top:** Median recurrence interval versus median moment for sequences from the Waldhauser and Schaff (2021) repeating earthquake catalogue on a log-log scale. Individual values are plotted as grey circles, with medians for moment bins shown as blue circles. The error bars on the medians indicate 95% confidence limits, which were estimated via bootstrapping (details in the text). The best-fitting line is plotted in solid black with a gradient of 0.15. **Bottom:** The total moment in repeating earthquakes in a sequence compared to the total moment in the sequence, including repeating earthquakes and partial ruptures. Each point is coloured by the median moment of the repeating sequence. Light pink points are the binned means. The dark pink triangles are the binned means corrected for missing small events (see text for more details).

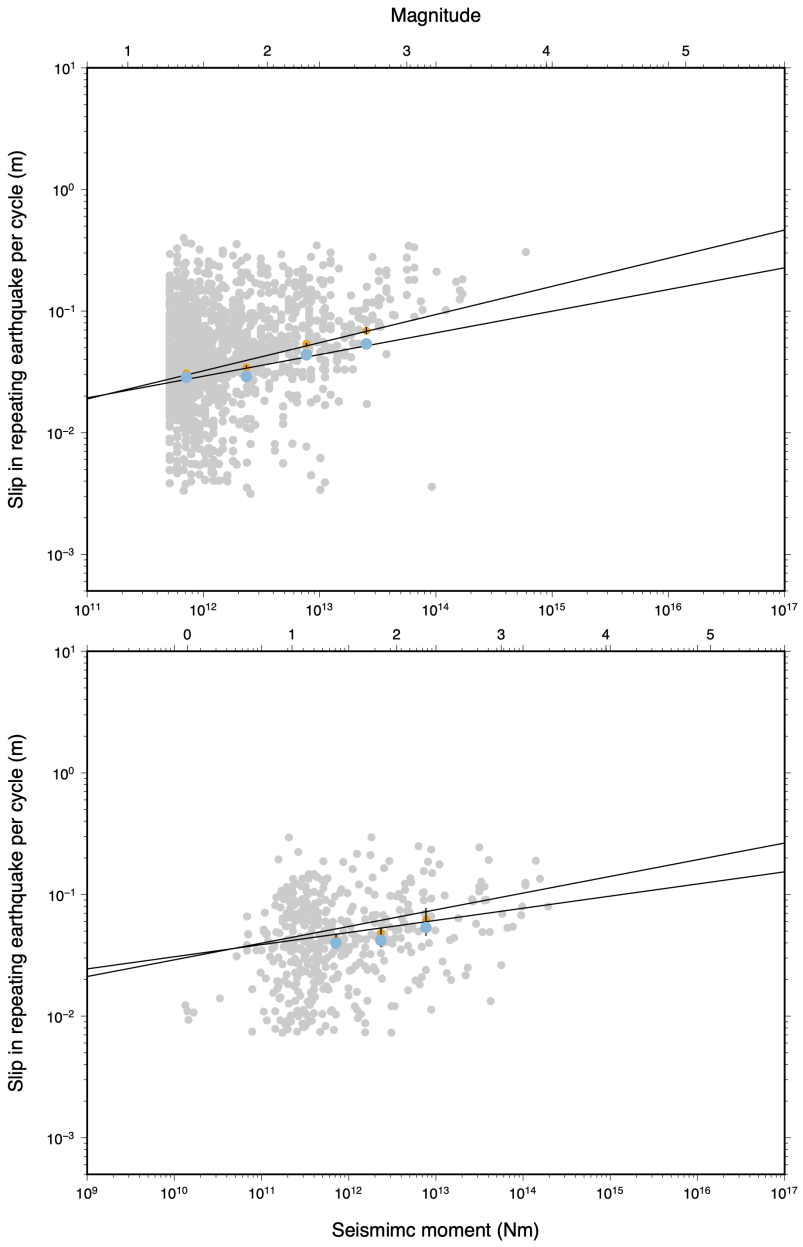


Figure 2.7: Top: Log slip per repeating cycle versus median moment for pairs of repeating earthquakes, assuming a long-term fault slip rate of 3mm/year for repeaters identified in this study. Individual values are plotted as grey circles, with medians for moment bins shown as blue circles. The error bars on the medians indicate 95% confidence limits, which were estimated via bootstrapping (details in the text). The orange circles are the medians for moment bins corrected for the moment in the partial ruptures. **Top:** Same as above but for Repeating earthquakes in the Waldhauser and Schaff (2021) catalogue.

in each sequence are similar (Figure A.3).

Comparing the catalogues, we identify 77% of the repeating earthquakes from the Waldhauser and Schaff (2021) catalogue, suggesting this simple location-based criterion for locating repeating earthquakes is suitable for this application in this region. 63% of the missed events are below the magnitude of completeness (see Figure A.6).

2.5 Discussion

We were motivated to search for partial ruptures of repeating earthquakes for two reasons: (a) to determine how much of the moment on repeater patches could be accommodated by partial ruptures and (b) to determine how large repeating earthquakes are relative to the earthquake nucleation size.

2.5.1 Partial rupture slip budget and repeater recurrence intervals

Some of the slip budget of the fault will be accommodated by the partial ruptures. Our observations reveal a significant number of partial ruptures and that these events can accommodate significant slip: up to 40% of the slip in each seismic cycle. However, for an event of M_w 1, the slip deficit is ∼an order of magnitude. The slip accommodated in partial ruptures still does not account for the total slip deficit for small magnitude events, as illustrated by the change in scaling of only ∼25% as shown in Figure 2.7.

2.5.2 How big are repeaters relative to their nucleation size R_∞?

In rate and state friction models of repeating earthquakes (Chen and Lapusta, 2009; Cattania and Segall, 2019), a ruptures' behaviours depend on the radius of the modelled unstable patch relative to the earthquake nucleation length R_∞. Small patches host simple earthquakes which rupture the whole patch; the rest of the slip is accommodated aseismically. It is only as patches become larger than ∼4.3

R_∞ that the patches host partial ruptures. As noted above, partial ruptures do accommodate significant slip on the fault. However, we do not observe a transition from no partial ruptures to partial ruptures with magnitude (Figures 2.4a & 2.6a). The magnitude-independent partial ruptures suggest that all partial ruptures are in the same regime: that most repeating earthquakes in Parkfield have R >> R_∞.

2.5.3 Compatibility of observations with the model

We are also motivated to examine moments in partial ruptures because the rate-and-state models model could reproduce the repeater scaling and, when appropriately tuned, could reproduce the overall scaling (Cattania, 2019; Chen and Lapusta, 2009).

We begin with a simple comparison with the model and note that our observations introduce two constraints:

(a) Fraction of moment accommodated by partial ruptures for $R >> R_\infty$. From a simple analytical scaling, we estimate that the lower bound moment in partial ruptures for $R >> 100R_\infty$ is 20% (see Appendix A.1),which is compatible with our observation of $5 - 40\%$. Again, repeating earthquakes in Parkfield have radii $R >> R_\infty$. A second constraint is then:

(b) that M 1-3 earthquakes have $R >> R_\infty$. From this constraint, we can estimate R_∞ to be a few metres or less. Although the rate and state model with this R_∞ can recover the scaling, it does not match the observed recurrence intervals nor explain the slip deficit. To match observed recurrence intervals, we could go back and try to tune the slip rate and stress drop (Figure 14 from Cattania and Segall, 2019). Assuming a long-term slip rate of 23 mm/yr would require a stress drop of 100 MPa or more. But observations suggest a lower stress drop, and a higher stress drop or a lower slip rate would still not account for the slip deficit for M 1-3 earthquakes.

There are, however, uncertainties in interpreting the model, as real faults are more complex than the simple homogeneous models. Real faults have complex geometries (e.g., Qiu et al., 2016), off-fault plasticity (Mia et al., 2022), and spatial variation in the frictional properties (e.g., Uchida et al., 2007). All three of these complexities could allow partial ruptures on asperities that are smaller than we would

infer given the average properties of the repeater patch. So it may still be possible to tune the model to match observed recurrence intervals, assuming stress drops of order 20 MPa and nucleation sizes of order 30 m. Future work may focus on the possible inclusion of complexity (e.g., Mia et al., 2022) in models or further testing other possible mechanisms, such as a variation in a long-term slip across the region.

2.6 Conclusion

With this work, we sought to test the hypothesis presented in the model of (Cattania and Segall, 2019) that small repeating earthquakes have exceptionally long recurrence intervals because small events occur between the time of repeating earthquakes. We identify partial ruptures in the relocated NCSN catalogue (Waldhauser and Schaff, 2008) of repeating earthquakes identified in the same way and those identified by Waldhauser and Schaff (2021). In both catalogues, we find few partial ruptures, with the repeating earthquakes accounting for >90% of the moment in each repeater and its co-located events. This suggests that partial ruptures alone cannot account for the moment deficit of small repeating earthquakes.

3

Stresses in the lunar interior: insights from slip directions in the A01 deep moonquake nest

Contents

3.1 Introduction 52
3.1.1 Motivation 53
3.1.2 Models of reversed polarity moonquakes 54
3.2 Data selection and initial processing 57
3.3 Principal component analysis of A01 moonquake waveforms 59
3.4 Qualitative analysis of principal components (G) . . . 63
3.5 Quantitative analysis of the number of slip directions 63
3.5.1 Determining number of slip directions using unbiased principal component coefficients (m') 64
3.5.2 Determining number of slip directions using the similarity of principal component vectors (G) 67
3.5.3 Partitioning of slip between directions 69
3.6 Validation 71
3.6.1 Potential influence of waveform alignment 72
3.6.2 Potential influence of scattering 73
3.7 Discussion 75
3.7.1 Explaining reversed polarity moonquakes 75
3.7.2 Implications of a small tectonic stress 76
3.7.3 Further application to moonquakes and earthquakes . . 77
3.8 Conclusion 78

Abstract

We probe the present-day stresses in the lunar interior by examining the slip directions of moonquakes in the A01 nest. In this nest, some deep moonquakes appear to slip "backwards", in the opposite direction to other events that happen in the same nest. We assess whether these changes in slip direction result from a spatial variation in the tectonic stress or from a temporal variation in the tidal stress. To test these two options, we first show that a dominant tectonic stress implies deep moonquakes can only slip in one direction on the fault plane: forwards and backwards, while a dominant tidal stress could allow moonquakes to slip in more directions on the fault plane: any combination of forwards, backwards, left, and right. Then we look for the number of slip directions; we separate the deep moonquake waveforms into slip directions using principal component analysis. We find two slip directions present in the A01 deep moonquake nest. The moonquakes slip in a variety of directions as time evolves. This observation implies that the tidal stresses drive deep moonquakes. Additionally, these results place a new constraint on the magnitude of the tectonic stresses at depth; they must be smaller than the modelled tidal stress of $\sim$0.1 MPa.

Plain Language Summary

The stresses that act in the lunar interior are not well known but are important for improving our knowledge of the interior of the Moon and its evolution. Deep inside the Moon, at depths between 700 km and 1200 km, moonquakes occur approximately every 27 days, suggesting they are influenced by the tides. Are the tides responsible for generating deep moonquakes? Or is long-term tectonic stress, in addition to the tidal stresses responsible? Using the waveforms of these deep moonquakes, we aim to determine the relative magnitudes of the tidal and tectonic stresses acting deep in the lunar interior. To do this, we look at the directions in which the moonquakes slip. We observe that deep moonquakes slip in a variety

of different directions, which can only be caused by tidal stresses. Since these deep moonquakes are generated by the tides, this observation reveals that tectonic stresses in the lunar interior must be smaller than 0.1 MPa.

Key points

- We examine why some moonquakes appear to slip in the opposite direction from the others.
- Using moonquake waveforms, we infer that slip direction changes through time because of tidal loading.
- The results indicate that the tidal stress, with magnitude 0.1 MPa, is larger than the tectonic stress.

3.1 Introduction

During the Apollo missions in the 1970s, four seismic stations were placed on the Moon's near side. These seismic stations recorded hundreds of deep moonquakes, which occur at depths of 700 - 1200 km.

Deep moonquakes tend to occur in clusters called "nests". In each nest, moonquakes occur at monthly intervals; they are seemingly influenced by the Earth-induced tidal stresses (Lammlein, 1977; Toksöz et al., 1977; Nakamura, 1978; Minshull and Goulty, 1988; Weber et al., 2009; Weber et al., 2010). However, the details of that influence remain unclear. Do tides trigger deep moonquakes by adding a small perturbation in stress on top of a large long-term tectonic stress? Or do tides generate deep moonquakes by providing most or all the stress at depth? In this study, we aim to constrain the relative magnitudes of tidal and tectonic stresses and their role in generating deep moonquakes. To do so, we theorise that if tectonic stress is dominant, a moonquake fault will always slip in one direction, while if the tidal stress is dominant, the fault can slip in a variety of directions. We use deep moonquake waveforms to determine the number of slip directions.

Previously, there have been two approaches to understanding the relationship between deep moonquakes and tidal stress: tidal modelling (e.g., Toksöz et al., 1977; Cheng and Toksöz, 1978; Weber et al., 2010; Araki, 2001) and seismological observations (e.g., Nakamura, 1978; Kawamura et al., 2017; Koyama and Nakamura, 1980; Weber et al., 2010). Some of these studies suggest that tidal stresses dominate the stress field in the deep moonquake source region. The tidal stress is large enough to account for the entire stress released in deep moonquakes (Kawamura et al., 2017). And large tidal stresses could also explain why some moonquakes appear to slip "backwards": in the opposite directions of most moonquakes in the nest. Moonquake slip directions could reverse if the tidal stresses dominate the local stress field and allow a reversal in the stress direction over their monthly oscillations (Toksöz et al., 1977; Nakamura, 1978).

However, other observations suggest that tectonic stresses dominate the local stress field. The tidal stresses may be larger than moonquake stress release, but local confining stresses are 10,000 times larger still (Minshull and Goulty, 1988). Additionally, studies that resolve the tangential tidal stress and stress rates onto candidate fault planes (described by a strike and dip) find that deep moonquakes do not always occur when the tangential tidal stress is the highest (Araki, 2001; Weber et al., 2009), suggesting that deep moonquakes must respond to some non-tidal stress.

3.1.1 Motivation

We were motivated to understand the relative magnitudes of the tidal and tectonic stresses for two reasons: (a) to provide observational constraints of the stresses in the lunar interior and, (b) to understand the mechanism of deep moonquakes.

Insights for the lunar interior

If tectonic stresses dominate the lunar stress field, they could have a variety of origins. They could be elastic stresses preserved from early lunar events (Weber et al., 2009); stresses generated by continuing weak convection (Frohlich and Nakamura, 2009); thermal stress from contraction of the lunar interior as it cools (Minshull and

Goulty, 1988; Solomon and Chaiken, 1976); volumetric stresses from phase changes (Weber et al., 2009); or stresses concentrated around compositional heterogeneities within the lunar interior (Zhao et al., 2012; Qin et al., 2012; Sakamaki et al., 2010; Steinberger et al., 2015). There are, however, few observational constraints on the stresses involved in these processes (Solomon and Chaiken, 1976). We may better constrain the long term stress magnitudes by understanding the stresses that drive deep moonquakes.

Deep moonquake mechanisms

Understanding the stresses in the lunar interior may also help us understand deep moonquakes themselves. These ruptures are enigmatic; they occur at pressures of ∼4 GPa and temperatures of 1500 to 1600 °C (Kawamura et al., 2017), where rocks are expected to deform slowly and ductilely, not in abrupt brittle failures.

Three mechanisms are commonly proposed to explain the existence of deep moonquakes: the same mechanisms proposed to generate intermediate-depth (∼100 km) and deep (> 410 km) earthquakes. Deep moonquakes may occur via (a) increased pore fluid pressure, which decreases the effective normal stress and allows for brittle failure at greater depths (e.g., Davies, 1999; Meade and Jeanloz, 1991; Hacker et al., 2003; Proctor and Hirth, 2015; Brantut et al., 2011; Dobson et al., 2002). Alternatively, they may occur via (b) thermal runaway, where a large initial shear stress and a small increase in strain rate lead to heating, runaway weakening and failure (e.g., Ogawa, 1987; Karato et al., 2001; Kelemen and Hirth, 2007; John et al., 2009; Thielmann et al., 2015; Thielmann, 2018). Or finally, moonquakes may occur via (c) a volume change and faulting associated with a mineralogical phase change (e.g., Kirby et al., 1996; Kirby, 1987; Green and Burnley, 1989; Burnley et al., 1991; Schubnel et al., 2013).

3.1.2 Models of reversed polarity moonquakes

In our search for the relative magnitudes of the tidal and tectonic stresses in the moonquake source region, we will focus on the stresses that allow reversed

polarity moonquakes. Reversed polarity moonquakes generate waveforms similar to the waveforms of normal-polarity moonquakes, just flipped (Figure 3.1a). These reversed polarity waveforms were observed at the A01 deep moonquake nest in 1972, 1973 and 1974, interspersed with normal polarity waveforms (Nakamura, 1978; Koyama and Nakamura, 1980; Frohlich and Nakamura, 2009). They originate from the same location as the normal polarity moonquakes but imply that some moonquakes in this location slip in the opposite direction to the rest. We test two models to explain this slip reversal.

Tectonic plug model

In the first proposed model, the long-term tectonic stress is larger than the oscillatory tidal stress. The shear stress at a given location is thus always in the same direction (arrows in Figure 3.1b). However, the stress may vary in space. Slip may occur on two parallel shear zones on either side of a moving plug, as sometimes observed during volcanic dyke intrusions (White et al., 2011). The motion of the plug would produce moonquakes that slip in roughly opposite directions, as observed.

Tidal model

In the second proposed model, first suggested by Nakamura (1978), the oscillatory tidal stress is larger than the long-term tectonic stress. The stress direction can thus vary with time on a fixed fault plane (Figure 3.1c). Reversed polarity moonquakes can occur on the same fault plane as normal moonquakes.

Differentiating between models for apparent slip reversal in the A01 nest

To test these models, we note that in the plug model, the stress is either forwards or backwards; there is one stress direction for each side of the plug. But in the tidal model, the stress can also rotate to different rakes along the fault plane (from the green to the blue arrow in Figure 3.1c). Since faults slip in the direction of the stress, we can make a similar statement about moonquake slip directions. In the plug model, moonquakes can slip forwards and backwards, but in the tidal model, moonquakes can slip in 2-D space, with any combination of left, right, forwards, and backwards.

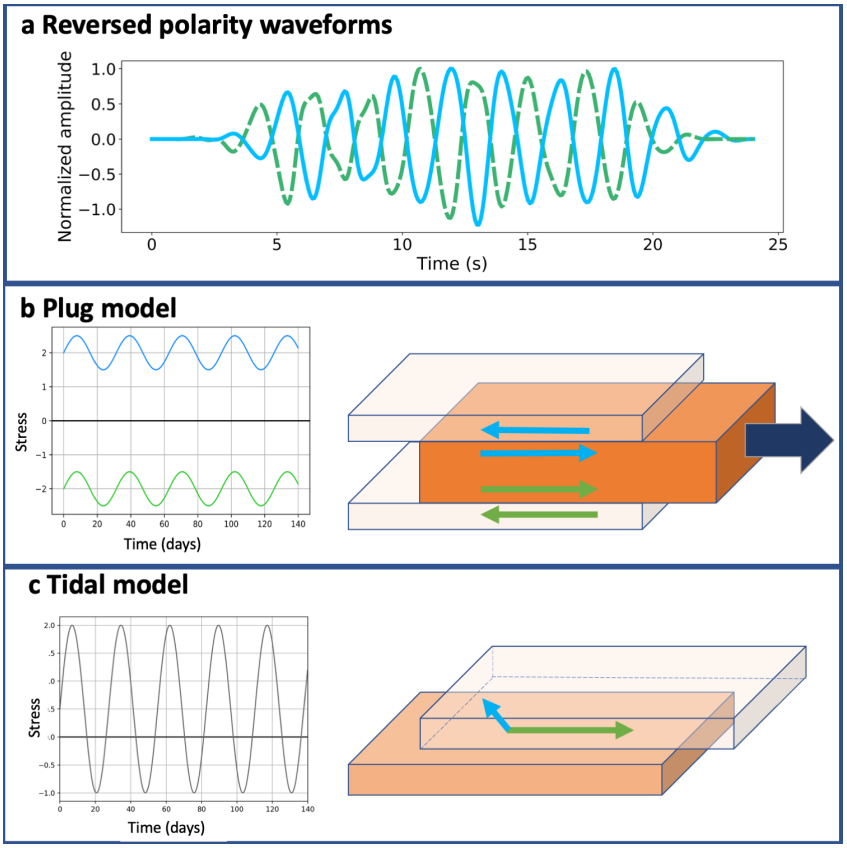


Figure 3.1: (a) A pair of moonquakes with reversed polarities, recorded on the east channel of station S16. The blue waveform was recorded on 17^{th} November 1973, and the green waveform was recorded on 5^{th} October 1975. The pair of events have a maximum cross correlation value of 0.87 in a 20 second window around the first arrival. For plotting, the windowed waveforms are bandpass filtered between 0.25 and 1.1Hz, and convolved with a 50% cosine taper.Two models have been proposed to explain the reversed polarity waveforms. In (b) the plug model, the long-term tectonic stress is larger than the oscillatory tidal stress. The stress directions (arrows) are constant in time but change from one side of the plug to the other. In (c) the tidal model, the tidal stress is larger than the tectonic stress. Slip occurs on a single fault plane, and the stress direction (arrows) changes over time, assuming a range of rakes.

We aim to determine whether the normal and reversed polarity moonquakes in the A01 nest slip along one direction (forwards and backwards) or along two directions (left, right, forwards, and backwards) and thus identify the dominant stress generating deep moonquakes. To do so, we will separate the energy in the deep moonquake waveforms into one or more slip directions with principal component analysis (PCA). We will apply a range of statistical tests to assess the slip directions' robustness.

3.2 Data selection and initial processing

In this study, we focus on the A01 deep moonquake nest. The nest is located 18° southwest of station S12 at a depth of 870 km (Nakamura, 2005b) and is the most active moonquake nest, providing enough good quality data to determine the number of slip directions.

We download the 3-component long period Apollo seismic data from the GEOSCOPE observatory through the IPGP data center (http://datacenter.ipgp.fr/). The original data was stored on magnetic tape, but it has been extracted from binary to SEED format for easier access (Nunn et al., 2017; Nunn et al., 2020a). The ground velocity data were recorded in two instrument response modes, flat and peaked mode. The peaked instrument response mode was the natural response of the seismometer, with a peak in the frequency response at about 0.45 Hz (Nunn et al., 2020b). The flat instrument mode was designed to be sensitive to a broader frequency range, from about 0.1 to 1 Hz (Nunn et al., 2020b). We consider moonquakes recorded in the two instrumental modes and at each station separately, so we leave the data as they were recorded and do not deconvolve the instrument response. When we use the uncorrected data in peaked and flat modes, they represent the convolution of the data with the two different frequency responses of the instruments. Each of the modes enhances different frequency bands while diminishing others. The signal-to-noise ratio can vary with frequency, creating differences between the two datasets. The different signal-to-noise ratios can be observed in the plotted waveforms (illustrated in Figures B.2 - B.8), where the noise amplitude in the peaked mode is lower than in the flat mode. By treating each component and instrument response mode separately, we avoid some of the issues that persist in the lunar data, such as different gains or frequency responses on different components (Nunn et al., 2020a).

To identify A01 moonquakes, we use the Nakamura (2003) catalogue with updates from Bulow et al. (2005). Each A01 moonquake recorded at station S12 is correlated with a template event for each operational mode in a 5-minute window around the first arrival (template events are given in Table B.1 and plotted in

Figure B.1). The template was chosen as an A01 event with a high amplitude and no data gaps recorded at station S12 in each operational mode. Events will be used for the PCA if they have a maximum cross-correlation value of greater than 0.3 with the template event in the cross-correlation window. The time shift of the maximum cross-correlation is also taken as the initial time shift to align the events. Finally, we check the events by eye to ensure no events with large data gaps or spikes in the time period of the first arrival. The same set of events is used on station S16. Events recorded at Stations 12 and 16 are rotated to the correct orientations given by Nunn et al. (2020b), as they were misaligned when they were installed. In principle, the rotation should have minimal effect on our analysis as we are concerned with the number of slip directions, not the absolute direction of motion. The rotated A01 event waveforms are despiked using a median filter (Bulow et al., 2005), resampled to twice the original sampling rate (0.07 samples per second) and bandpass filtered between 0.25 Hz and 1.75 Hz.

We found few good quality moonquakes with clear arrivals at stations S14 or S15 and therefore analyse data from stations S12 and S16 only. After this pre-processing, we have a dataset of waveforms at each component, station and instrument response. We consider 14 moonquakes recorded at station S12 channel MHN in the peaked operation mode (Figure 3.2). We consider between 12 - 28 waveforms recorded on each of the east channels (MHE), in flat mode, and at station S16 (illustrated in Figures B.2 - B.8). The reversed polarity waveforms recorded in each instrument mode are listed in Table B.2. In the data recorded at station S16 in the peaked mode there are 5 reversed polarity events, and in the data recorded at station S12 in the peaked mode there are 3. Due to the time the instrument was operating in flat mode, we do not identify any reversed polarity events in these subsets of the data. Nevertheless, we apply the same analysis to understand how the slip directions may vary.

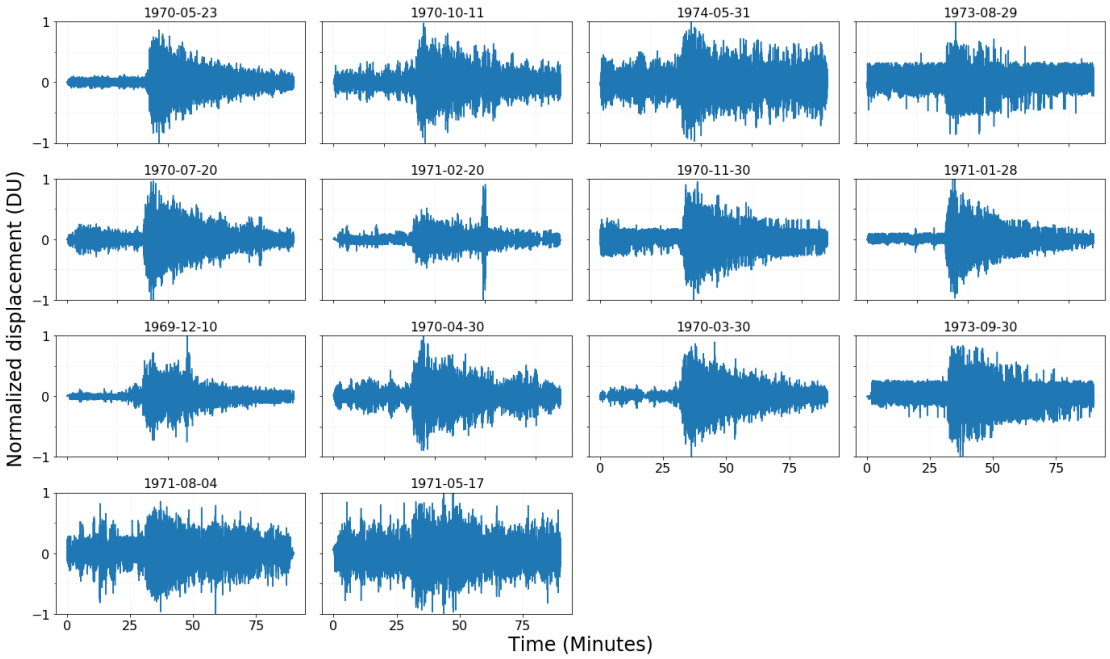


Figure 3.2: Deep moonquake waveforms used for PCA decomposition, recorded at station S12, channel MHN, in the peaked operation mode.

3.3 Principal component analysis of A01 moonquake waveforms

To assess the stress state in the deep moonquake generating region, we examine moonquake slip directions. For terrestrial problems, researchers often determine individual earthquake's focal mechanisms—their fault planes and slip directions—using the polarities or amplitudes of first arrivals recorded at a number of stations (e.g., Hardebeck and Shearer, 2002; Yang et al., 2012). Some previous studies have attempted to determine a moonquake fault plane for the A01 nest (described by a strike and dip) but were unsuccessful (Weber et al., 2009; Araki, 2001). However, moonquake slip directions are not routinely estimated; it remains challenging as moonquake seismograms have emergent onsets, as shown in Figure 3.2 and are recorded at only four stations (Nakamura, 1978; Weber et al., 2009).

Instead, then, we determine the range of moonquake slip directions by comparing waveforms of various events in the A01 nest using principal component analysis. Principal component analysis (PCA) is a statistical method that models a set of observations as a linear combination of particular basis functions: a set of linearly

uncorrelated vectors called principal components. These principal components are chosen so that the first component accommodates as much of the observed signals as possible. The second component then reconstructs as much of the remaining signal as possible, and so on until the last component accommodates only a small fraction of the signal (Bishop and Nasrabadi, 2006). PCA has previously been applied to problems in earthquake seismology. It has been used to identify dominant trends in earthquake locations (Ocaña et al., 2008), to identify similarities in recovered moment rate functions (Vasco, 1989; Vasco, 1990), and to determine moment tensors of earthquakes (Vavryčuk et al., 2017).

Let us consider all the A01 moonquake seismograms $U_k(t)$ recorded on a single channel at a single station. Since the moonquakes in a nest occur within a compact cluster, only a few km wide (Nakamura, 1978), we can model the displacement at the lunar surface created by the moonquake using a moment tensor representation as :

$$U_k(t) = \sum_{j=1}^{J} G_j(t) m_{kj}, \tag{3.1}$$

as illustrated in Figure 3.3, U_k is the waveform for event k, and G_j is the Green's function: the surface displacement produced by unit moment (slip times area times local shear modulus) applied in direction j on the fault. We assume that the moonquakes all occur on the same fault, so the fault orientation (strike and dip) is constant, which leaves two directions in which the moment can be applied in J=1 or J=2. We call m_{kj} the slip coefficient: it is the moment in direction j for event k.

If we collect the J waveforms observed from several A01 moonquakes k into the columns of the matrix $\mathbf{U}$, we may note that Equation 1 has the same form as that used in the principal component analysis: $\mathbf{U} = \mathbf{Gm}$. PCA decomposes the data matrix ($\mathbf{U}$) into a set of coefficients (rows of $\mathbf{m}$) multiplied by a set of basis vectors or principal components (columns of $\mathbf{G}$). It would thus seem that we can use a PCA decomposition to recover the slip coefficients ($\mathbf{m}$) and Green's functions ($\mathbf{G}$) from the deep moonquake waveforms. Both $\mathbf{G}$ and $\mathbf{m}$ are unknowns, but can be recovered together using PCA by also assuming the Green's functions

(**G**) are uncorrelated, ordered by the variance they explain, and that each principal component explains as much of the variance of the data as possible.

However, it is important to note that the PCA decomposition always recovers the same number of principal components as waveforms (i.e. in equation 1, J = number of events). The components are chosen such that the first components accommodate as much of the signal in the data vectors U_k as possible. Later components accommodate progressively less signal. We then interpret the principal components as the Green's functions for one or more slip directions. We expect the first few principal components to be Green's functions for the slip in one or more directions, as they can accommodate signal from multiple moonquakes. Later principal components are likely to be noise, which differs from event to event. Our challenge will be to determine which principal components represent Green's functions and which principal components represent noise (Figure 3.3).

The number of principal components representing Green's functions will let us distinguish between the two models of moonquake slip presented in Section 3.1.2. For the plug model, we hypothesise that there is a single slip direction; one principal component should have a large m_{k1} and contain signal common to multiple moonquakes, representing a real Green's function of that slip direction while all other m_{kj} should be close to zero. In contrast, the tidal model predicts two slip directions; two principal components should have two a large m_{k1} and m_{k2}, representing real Green's functions of the two slip directions, and all other m_{kj} should be close to zero (Figure 3.3).

In carrying out the PCA, we must ensure good waveform alignment. The signal in each principal component is sensitive to waveform alignment, as time-shifted traces can be mapped into different components. Before we compute the PCA decomposition, we cross-correlate each waveform with a high-quality template event to obtain a best-fitting initial time shift, as described in Section 3.2. Then we apply the principal component analysis to a 10-minute window of the A01 deep moonquake waveforms, which includes the direct P and S arrivals and scattered arrivals in the coda. Finally, we fine-tune the alignment. Our bootstrap analysis

suggests that events are initially aligned using cross-correlation within two or three samples, so we ensure the best alignment between the waveforms by searching 0.7 s (10 samples) around the cross-correlation time shifts to maximise the energy in the first component of the PCA.

The principal components determined from the PCA decomposition are plotted in Figure 3.4. We discuss their qualitative characters in Section 3.4. In Section 3.5, we examine the coefficients and principal components determined from the PCA more quantitatively.

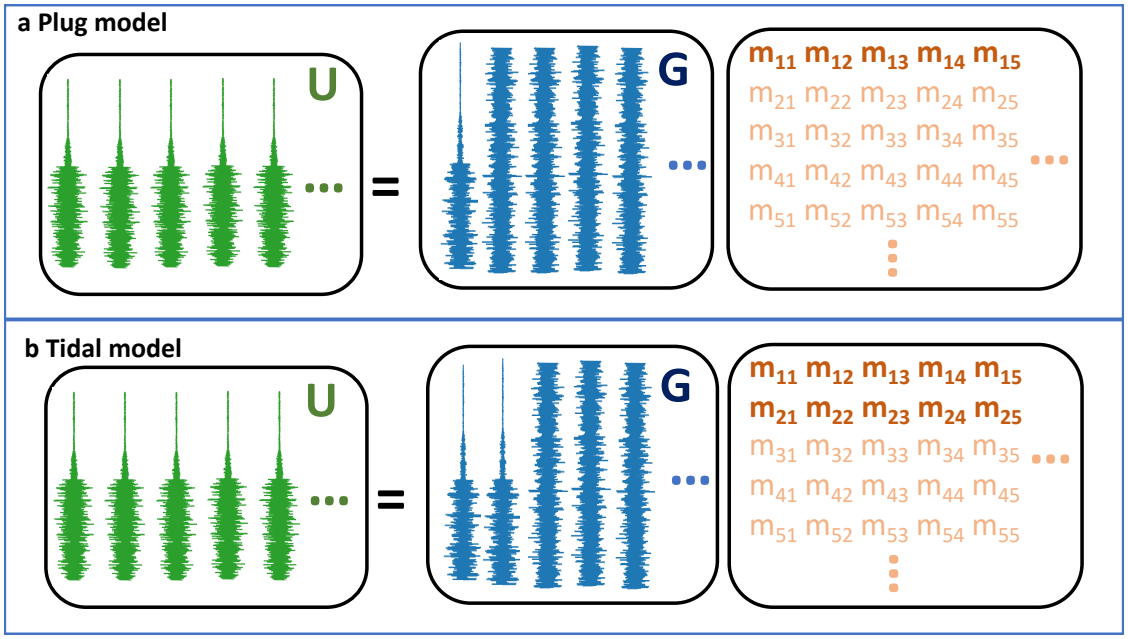


Figure 3.3: Illustration of the PCA decomposition for the A01 moonquakes. A matrix of waveforms (Green, **U**), is decomposed into the principal components (blue, **G**), and the coefficients (orange, **m**). We then interpret the principal components as slip directions. (a) For the plug model, events only slip either backwards or forwards. We expect one recovered principal component to be a real Green's function of the slip direction: one principal component will contain signal and all others will contain noise. The slip coefficients m_{k1}, will be large (shown in a darker bold orange), while all others will be small. (b) For the tidal model, events can slip in any combination of left, right, backwards and forwards. We expect two principal components to represent real Green's functions of slip: two principal components will contain signal and all others will contain noise. The slip coefficients m_{k1} and m_{k2} will be large and all others will be small.

3.4 Qualitative analysis of principal components (G)

We begin by analysing the shape of the recovered principal components. Figure 3.4 shows the 14 principal components for the peaked mode MHN records at station S12, ordered by the percentage of the data variance they explain. The first three principal components, which explain the most variance, have clear onsets in signal followed by decays. They have "moonquake-like" shapes, similar to the waveforms in Figure 3.2. These shapes suggest that the first three principal components could represent real Green's functions. Later principal components, which explain progressively less of the variance, do not have clear onsets or decaying "moonquake-like" shapes.

Using the MHE records at station S12 (Figure B.9), we also observe three moonquake-shaped principal components. However, when we analyse the flat mode MHN and MHE data (Figures B.10 and B.11), there are only two "moonquake-shaped" principal components.

When we analyse the waveforms recorded at station S16 (Figures B.13 - B.15), we again observe three moonquake-shaped components in the decomposition of the peaked mode data and two moonquake-shaped components in the flat mode data. A qualitative analysis of all the data thus suggests that two or three principal components represent Green's functions, while the rest represent noise.

3.5 Quantitative analysis of the number of slip directions

Next, we aim to more rigorously determine whether each derived principal component represents a Green's function or represents noise. We quantitatively analyse the "slip" coefficients m obtained for each principal component and event (Section 3.5.1) as well as principal component vectors G themselves (Section 3.5.2).

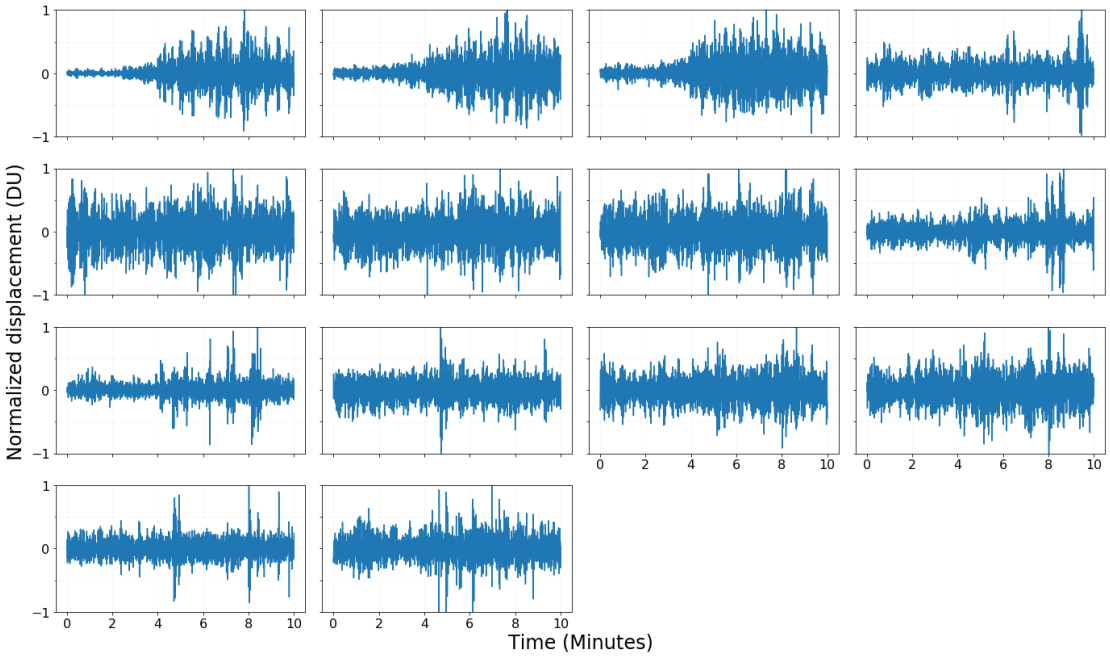


Figure 3.4: Principal components derived from the S12 MHN data in the peaked operational mode of the instrument.

3.5.1 Determining number of slip directions using unbiased principal component coefficients (m')

The "slip" coefficients m_{kj} determine how much of each principal component j is needed to reconstruct the seismogram generated by moonquake k. If a principal component $G_j(t)$ represents a real Green's function, its coefficients are likely to be large for multiple moonquakes k. We therefore aim to assess the coefficients' values.

To accurately assess the coefficients' values, we need to compare principal component vectors with "unseen" validation waveforms. We want to know how well each principal component can be used to reconstruct moonquake waveforms that were not employed in creating principal component vectors.

To achieve this, we use a method similar to "leave-one-out cross-validation" (Bishop and Nasrabadi, 2006). We calculate PCA using all but one "left-out" moonquake waveform. We project the left-out waveform onto each of principal components to obtain an unbiased coefficient m'_{kj} for component j and moonquake k:

$$m'_{jk} = Gres_j(t)u_k(t). \tag{3.2}$$

Here u_k is the waveform of the excluded moonquake, and $Gres_j$ is the jth principal component, calculated using the remaining moonquakes. We repeat this process, excluding each available moonquake k in turn, so that we have a set of unbiased coefficients m'_{kj} for each moonquake.

We use a bootstrap approach to estimate the uncertainty on the coefficients m'_{kj}. We again exclude event k and recompute principal components, but instead of using all remaining moonquakes in PCA calculation, we randomly resample the remaining moonquakes with replacement. With this new subset of moonquakes, we recompute principal components $Gres_j$ and the projected coefficients m'_{jk} 25 times.

The coloured circles in Figure 3.5b-d show these 25 projected coefficients m'_{kj} for each of the station S12 MHN moonquakes. The coefficient for the first principal component m'_{k1} is plotted on the x-axis. The coefficients of the second (m'_{k2}), third (m'_{k3}), and last (twentieth, m'_{k20}) principal components are plotted on the y axis of Panels b, c and d, respectively. Each event k is plotted in a different colour.

Figure 3.5a summarises the distribution of the coefficients of the first principal component m_{k1} for all moonquakes from the peaked mode S12 data. The distribution of the coefficients is bi-modal, with clusters around ± 12. Note that a single event can have both a positive and negative m' because the signs of G_j and m'_{kj} can trade-off; in bootstrapping, G_j can flip and be compensated by a flip in the sign of m'_{kj}. The non-zero average amplitude of the coefficients, along with the gap around zero, implies that there is a large m'_{k1} common to all moonquakes. The first principal component thus seems to represent a real Green's function.

Panel e summarises the distribution of the coefficients of the second principal component, m'_{k2}. The bi-modal distribution and non-zero average amplitude of the coefficients that imply the second principal component also represents a real Green's function.

Panel f and g summarise the distribution of coefficients for the third and last components. These distributions have only a single peak, and the average values

of the distributions are near zero. The near-zero values suggest that there is little moonquake signal in these principle components; they mostly accommodate noise that varies from event to event.

We may more quantitatively compare the coefficient distributions with a Kolmogorov-Smirnov test, a general nonparametric method used to compare two distributions. We assume that the last principal component accommodates only noise, and take its coefficient distribution, plotted in Panel g, as representative of the coefficients derived from noise. The first and second principal components' coefficients differ from this noise distribution with probabilities of near 100% and 99.1%, respectively; these coefficients are likely accommodate moonquake signals. In this analysis of the peaked mode S12 data, the third component's coefficients differ from the noise with a probability of only 30%. Later components' coefficients are also similar to the distribution of noise.

We obtain similar results when we analyse the distribution of coefficients for all other stations, components, and instrument modes. For example, Figure B.16 summarises the distribution of coefficients for the station 12 peaked mode MHE waveforms. The distributions of coefficients for the first and second principal components are again bi-modal, and the average distribution amplitude is non-zero. The distributions differ from noise with probability near 100 % and 99 %, respectively. The distribution of coefficients in the third and later slip directions have only a single peak at zero and are similar to the distribution of coefficients derived from noise.

Similar although slightly less well-resolved distributions are obtained from flat mode data at station S12 (Figures B.17 and B.18). For both the MHN and MHE records, the distributions of coefficients for the first principal components are bi-modal, and both differ from noise with probabilities near 100%. The distributions of the second principal components are not bi-modal, but they are uniform rather than Gaussian. The distributions still differ from the noise distributions with a probability of 92% and 99% for the MHN and MHE records. The third principal component also differs from noise with a probability of 99%, but it has a large peak at zero. Later components are similar to noise.

Similar results are obtained from station S16, as illustrated in Figures B.16 - B.21. The distributions from all stations and channels imply that two principal components have a large m'_{kj} common to multiple moonquakes and represent real slip directions.

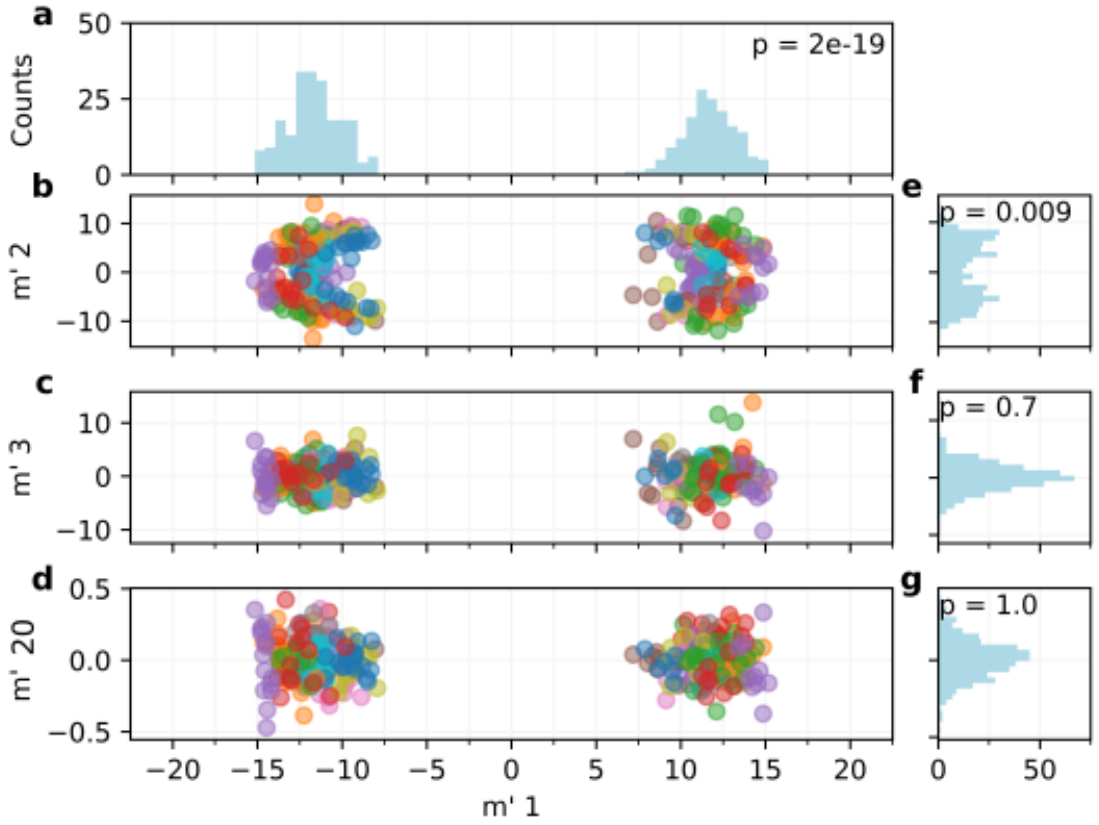


Figure 3.5: Unbiased coefficients of principal components, from the S12 MHN data in the peaked operational mode. In Panels b - d, the coefficient for the first principal component m'_{1k} is plotted on the x-axis. The coefficients of the second (m'_{2k}), third (m'_{3k}) and last (m'_{20k}) principal components are plotted on the y axis of Panels b,c and d, respectively. Each event is plotted in a different colour. Panels a, e, f, and g summarise the distribution of coefficients for each of principal components. The text in the top of Panels a, e, f, and g is the probability (p-value) that each distribution is the same as the distribution of the coefficients derived from noise. Only the first two components differ from noise.

3.5.2 Determining number of slip directions using the similarity of principal component vectors (G)

In the bootstrapping described above, we re-estimated principal components G_j and coefficients m'_{kj} for various subsets of the data, and we analysed the coefficients

m'_{kj}. In this section, we examine the variation among the estimated principal component vectors G_j.

We expect little variation in the estimates of a given principal component G_j if that component recovers a real moonquake signal common to multiple moonquake waveforms. But we expect large variation in bootstrapped estimates of a principal component G_j if that principle component recovers noise, which varies between waveforms.

We examine the similarity of the bootstrapped principal components using a modified version of the algorithm ICASAR. This algorithm was originally designed to separate ground deformation and atmospheric signals in time series of interferograms using independent component analysis (Gaddes et al., 2019), but we use it to analyse the similarity of our bootstrapped principal component estimates. The similarity between two principal component estimates is quantified as the absolute value of their cross-correlations.

The ICASAR algorithm clusters the bootstrapped principal components according to these cross-correlation values. It uses a hierarchical clustering algorithm (HBDSCAN) to identify similar principal component estimates (McInnes et al., 2017; Gaddes et al., 2019). We assess the quality of clusters using the cluster quality factor I_q: the difference between the mean intra-cluster similarity (1 for a perfect cluster) and the mean similarity between members of the cluster and all other component estimates (0 for a perfect cluster).

We would now like to visualise the similarities between principal component estimates, but without plotting the numerous computed cross-correlations. To do so, we project the set of cross-correlations into a two-dimensional space. We choose the dimension's directions according to a t-distributed neighbourhood embedding algorithm. These directions do not have any physical meaning, but they preserve a key feature of distance: points close together represent component estimates that have a high cross-correlation, while points that are far apart have a low cross-correlation (t-sne algorithm, Maaten and Hinton, 2008; Gaddes et al., 2019).

Figure 3.6 shows the clusters determined using principal components of waveforms recorded at station S12 MHN in peaked mode, projected along the first two t-sne directions. Only projections from the first four principal components are shown. Points in Figure 3.6 are coloured by the clusters identified by the HBDSCAN algorithm (McInnes et al., 2017; Gaddes et al., 2019). Principal components in the blue cluster are similar; they have an I_q of 0.87. Principal components in the orange cluster have a slightly lower similarity; $I_q = 0.74$. Points coloured grey represent principal component estimates that are not similar enough to other estimates to form a cluster.

The two clusters identified by the HBDSCAN algorithm and shown visually in Figure 3.6 suggest that two principal components contain signal common to multiple moonquakes and that these signals are repeatedly recovered in bootstrapping. We obtain similar clusters if we adjust the clustering parameters; if we perturb the minimum cluster size or the distance required to define a "neighbour". Similar clusters are obtained from other stations, components, and instrument modes (Figures B.23- B.28).

3.5.3 Partitioning of slip between directions

Our analysis in sections 3.5.1 and 3.5.2 implies that waveforms from the A01 nest can be decomposed into two principal components that are different from noise. We can now analyse the magnitude of slip in each direction, as we can now interpret the first two coefficients m' not just as coefficients of principal components but as slip coefficients. Each m'_{jk} is proportional to the amount of moment in each direction for moonquake k.

Figure 3.7 shows distributions of the $|m'_{1k}/m'_{2k}|$ ratios: the ratio of the moment the second slip direction to the moment in the first slip direction. These distributions are also shown plotted on log axis in Figure B.30. The coloured area shows the probability density of the ratio obtained at each station and component, and the white dots mark the median ratio. All distributions are consistent with significant slip in the second direction; distributions have peaks above, not at zero, and the

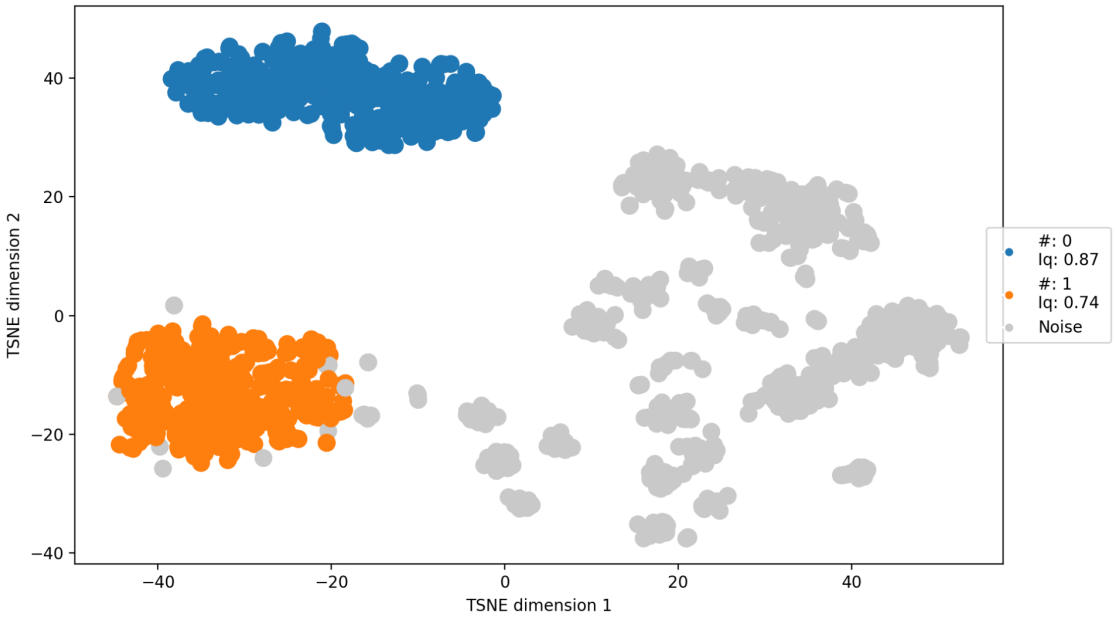


Figure 3.6: Clustering results of bootstrapped principal component vectors **G**, obtained for S12 MHN in peaked operational mode. One point is plotted for each bootstrapped estimate of a principal component, but only the first four principal components are plotted. The location of each point is determined by the t-sne algorithm, preserving the similarity of components from the higher dimensional space (Maaten and Hinton, 2008; Gaddes et al., 2019). The colour of each point is determined by the HBDSCAN clustering algorithm (McInnes et al., 2017; Gaddes et al., 2019). Two clusters are shown, in blue and orange. Grey points represent component estimates that are not assigned to a cluster.

median ratios range from 0.11 to 0.33, with a median at all stations of 0.21 . Finally, we can examine how the slip coefficients vary from moonquake to moonquake. Figure 3.8 shows the normalised $m'_{kj}/\sqrt{m'^2_{k1} + m'^2_{k2}}$ values for peaked mode MHN and MHE records at stations S12 and S16. If these recovered directions were orthogonal (e.g. cardinal directions), a vector from the origin to each point would give the slip direction. Note, however, that PCA does not necessarily identify orthogonal slip directions. It only identifies slip directions that produce different Green's functions, and those directions are the ones illustrated on the axes of Figure 3.8.

We can nevertheless interpret several features of the varying slip coefficients. First, Figure 3.8 shows both positive and negative coefficients in the first slip direction. The negative coefficients correspond to moonquakes that slip in the opposite direction of most events; they create the reversed polarity waveforms. Second, and perhaps more interesting, the slip directions do not appear clustered;

there is a variable amount of slip in the second direction. Moonquakes appear to slip in a range of directions within a 2-D plane, not in two particular directions.

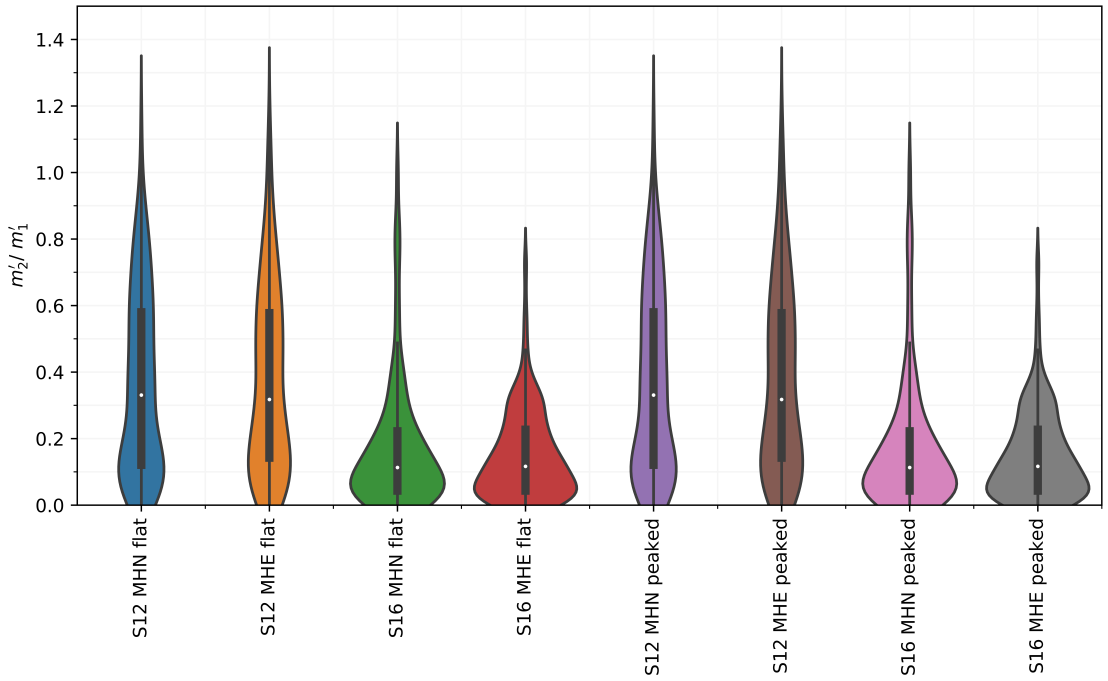


Figure 3.7: Slip coefficient ratio $|m'_{1k}/m'_{2k}|$ for each station and channel. The white dot marks the median bootstrapped ratio at each station, the black bar delimits the inter-quartile range, and the thin black line delimits 1.5 × the inter-quartile range. The coloured areas illustrate the probability density of the ratio at each station. All distributions have peaks above zero, and the median $|m'_{1k}/m'_{2k}|$ ratios range from 0.11 to 0.33.

3.6 Validation

Our analysis implies that two principal components are required to accommodate signal common to many moonquakes in the A01 nest, and when we interpret the principal components as slip direction, that these moonquakes slip in two directions. However, some errors have the potential to create artificial principal components. So here we check that the second significant principal component is a physical feature of the moonquakes and not a result of poor waveform alignment (Section 3.6.1) or scattered seismic waves (Section 3.6.2).

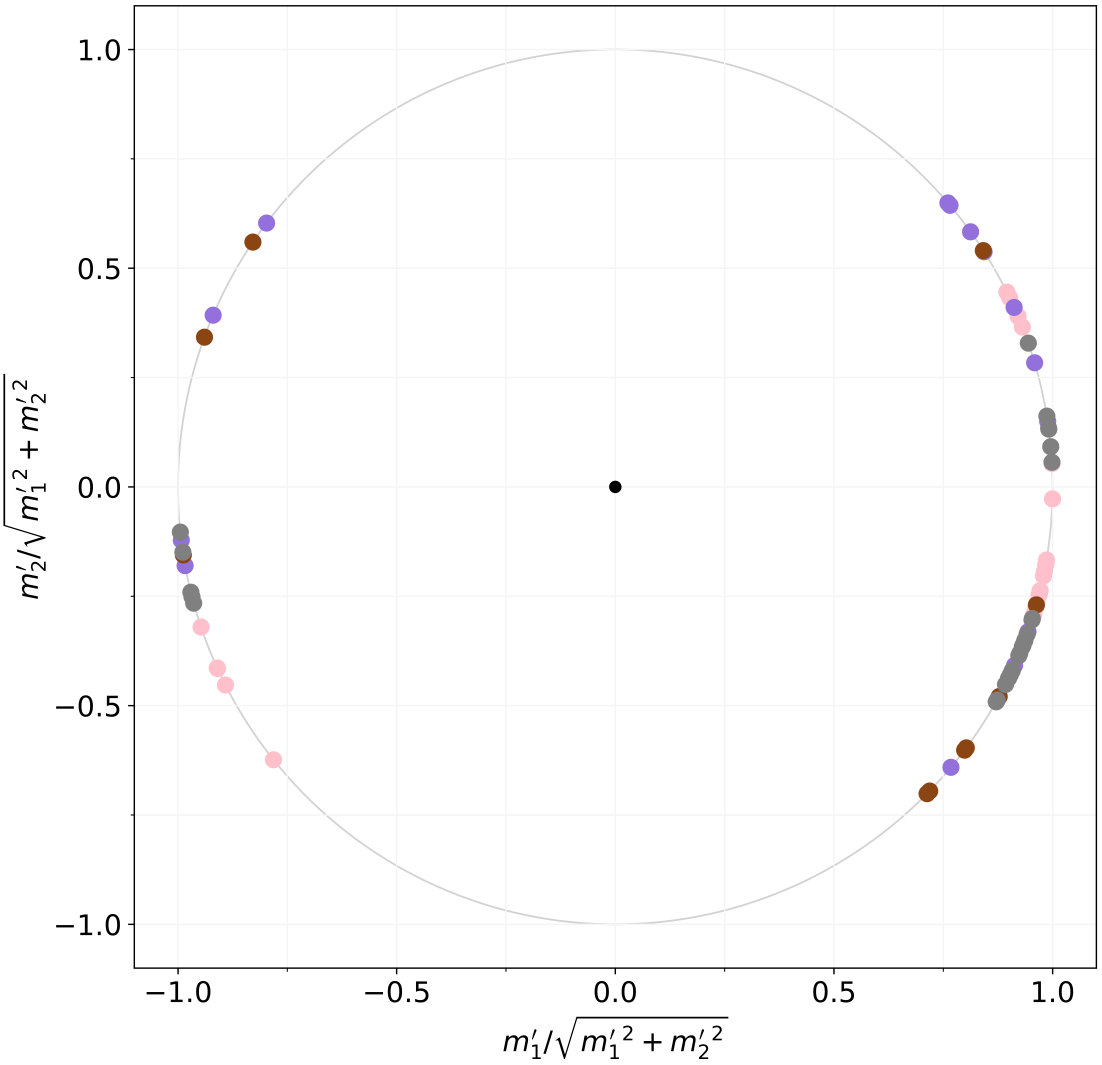


Figure 3.8: Normalised unbiased slip coefficients for the first and second Green's functions, for moonquakes recorded at both stations and components in the peaked instrument mode. If the slip directions are orthogonal as plotted here, a vector from each point to the origin would give the slip direction on the fault plane (rake). Negative coefficients in the first slip direction correspond to reversed polarity moonquakes, which slip roughly in the opposite direction of most events. Note, however, that moonquakes appear to slip in a range of direction within the m_{k1}-m_{k2} plane. The colours correspond to the station and channel considered, as used in Figure 3.7 (purple: S12 MHN peaked; brown: S12 MHE peaked; pink: S16 MHN peaked; grey: S16 MHE peaked).

3.6.1 Potential influence of waveform alignment

We first check that we have not obtained two principal components because the moonquake waveforms are poorly aligned. We verify that the second principal component is not a time-shifted version of the first component. Then we examine

how the number of significant principal components changes if we add errors in the waveform alignment – if we randomly shift each waveform by a random value drawn from a uniform distribution.

Figure 3.9 shows the percentage of the variance accommodated by principal components as we increase the maximum random shift from 0 to 1 second. For shifts up to ∼0.17 seconds, energy in the first principal component decreases as the alignment worsens, but that energy is distributed over a number of the later components; the energy in the second principal component does not increase significantly. Since the cross correlation and fine-tuning of the time-shift allows an accuracy of 0.07 seconds (the sampling rate of the traces), it seems unlikely that the significant energy we observe in the second principal component results from poor waveform alignment.

3.6.2 Potential influence of scattering

Next, we assess whether the second slip direction could result from scattering. Moonquakes in the A01 may be in slightly different locations, up to a few km of each other (Nakamura, 2003), and their seismic waves may follow slightly different paths through the Moon, especially in the near-surface scattering layer. The different paths could lead to different recorded seismograms, especially later in the coda, when the seismic waves have been more scattered.

To look for scattering, we apply PCA to 30-second windows throughout the seismogram, from the direct S wave arrival onward into the coda, as illustrated in Figure 3.10a. Figure 3.10b shows the variance explained by the first, second, and last principal components in each of the windows. The different operational modes, components, and stations also give similar results. The variance in the second component does not significantly increase later in the coda, suggesting that scattering later in the coda does not create the significant signal we observe in the second principal component.

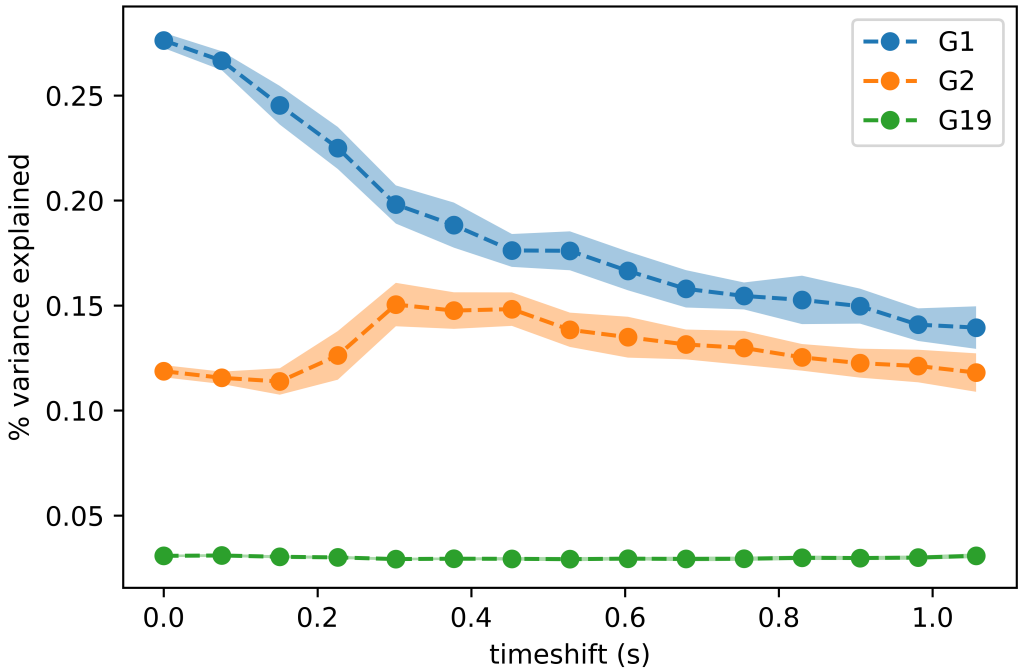


Figure 3.9: Testing the influence of inaccurate waveform alignment. We apply random time-shifts with magnitude up to 1.1s (x-axis) and determine the percentage of the data variance explained by the first (blue), second (orange), and last (nineteenth,green) principal components.

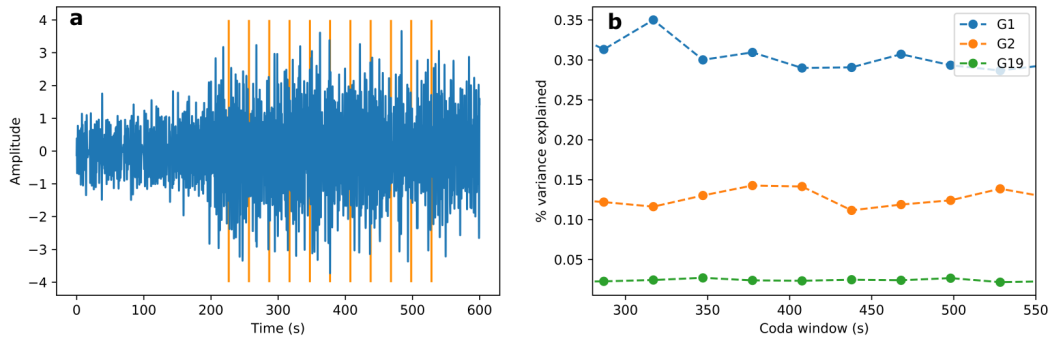


Figure 3.10: (a) A single moonquake waveform, observed at station S12 in flat mode, divided (orange lines) into 30s windows throughout the coda, starting after the high-amplitude S wave arrival. (b) Percentage variance accommodated by the first, second and last components in each time window. The variance percentages remain roughly constant as we move from the direct arrival into the more scattered coda. Scattering thus does not appear to explain the significant signal in the second component.

3.7 Discussion

In this study, we have used PCA to separate the signal in deep moonquake waveforms into principal components common to multiple moonquakes. We find that two principal components are required to reconstruct the data. These components likely reflect the signals created by slip in two different directions.

3.7.1 Explaining reversed polarity moonquakes

We were motivated to examine moonquake slip directions because some moonquakes have reversed polarity waveforms; these moonquakes appear to slip "backwards". We sought to determine whether this reversal arises because of a spatially varying tectonic stress, where stress changes direction on either side of a plug (Figure 3.1b), or whether the reversal arises because the tectonic stress is small, and a tidal stress drives moonquakes and changes direction through time (Figure 3.1c). To distinguish between these models, we note that the tectonically driven plug model implies only one slip direction: forwards or backwards, while the tidal stress model could allow two slip directions: any combination of forwards, backwards, left, or right. Our observation of two slip directions is more consistent with the tidal model of reversed polarity waveforms.

In principle, however, the plug model could also allow two slip directions. If the two sides of the plug are not parallel, we might see one slip direction (A) on one side of the plug and another direction (B) on the other side. In this case though, the two slip directions would be fixed. Slip might occur in direction A and in direction B, but not in any direction along the plane that contains directions A and B. For such a scenario, we could expect the estimated slip coefficient vectors, $[m_1, m_2]$, as decomposed using principal component analysis, to cluster around two directions, representing slip directions A and B on either side of the plug. We do not observe such clustering.

Instead, we see variation in the first and second slip coefficients (Figure 3.8); the 2-D variation is more consistent with the tidal model, which allows the slip direction to move along the fault plane as the tidal stress changes.

The variation in the slip direction we observe is also consistent with P/S amplitude variations (Nakamura, 1978) and changes in the slip direction determined from S wave polarities (Koyama and Nakamura, 1980), all of which suggest slip occurs on a fixed fault plane, but the direction of slip can vary with time.

The two slip directions we identify thus suggest that an oscillating tidal stress drives deep moonquakes in the A01 nest and that this tidal stress changes the local stress direction through time.

3.7.2 Implications of a small tectonic stress

If tidal loading changes the direction of stress in the moonquake region through time, the tidal stresses must be larger than the local tectonic stress. We thus have a new constraint on the magnitude of the tectonic stress at depth; it must be less than the maximum modelled tidal stress of ∼0.1 MPa (Toksöz et al., 1977; Minshull and Goulty, 1988; Weber et al., 2009).

Excluding a ductile mechanism for moonquakes?

We may use this cap on the tectonic stress to help constrain the enigmatic mechanism of deep moonquakes under high pressures and temperatures. Some models have suggested that moonquake slip is driven by a viscous thermal runaway (Thielmann et al., 2015). As the fault slips, the temperature increases, grains reduce in size, and melting can occur, localising and accelerating the slip on the fault. The runaway process allows ductile failure on seismic timescales. However, large initial shear stresses (∼100 MPa at high strain rates, Thielmann et al., 2015) are required to initialise localisation, and those stresses are not compatible with our 0.1 MPa upper bound on the tidal and tectonic stress in the A01 moonquake region. This allows us to rule out this mechanism for deep moonquakes.

A variety of models remain to explain the rapid failure that creates moonquakes at high pressure and temperature, though all the models remain poorly tested. One model suggests that high pore fluid pressure could reduce the effective stress on faults at depth and enable deep moonquake faults to slip. The lunar interior is wetter than

previously thought (Evans et al., 2014). However, it remains unclear whether there is enough water in the right places to account for the generation of deep moonquakes.

Alternatively, deep moonquakes could be related to a mineral phase change, as proposed for deep (> 400 km) earthquakes. However, current models of the lunar interior do not identify a suitable phase change (Garcia et al., 2011; Garcia et al., 2012) and this phase change would have to somehow occur repeatedly to create repeating moonquakes in a small volume, making this mechanism unlikely.

Lunar interior

In addition to improving our understating of the mechanism of deep moonquakes, our moonquake-derived stress bounds, which imply that the local tectonic stress is smaller than the tidal stress, also provide constraints on thermal and dynamic models of the lunar interior. This stress bound implies that any stress from thermal contraction must be less than 0.1 MPa, consistent with previous estimates (Solomon and Chaiken, 1976). We can also place an upper bound on any remaining convection. If we assume a Newtonian viscosity of 10^{21} Pa s (e.g., Li et al., 2019), a long term stress smaller the 0.1 MPa implies a local strain rate smaller than 10^{-16} s^{-1}. Future research may find other uses for our moonquake-derived stress bounds. For example, the bounds might be used to provide constraints on stress concentrations around local heterogeneity within the lunar interior (Zhao et al., 2012; Qin et al., 2012; Sakamaki et al., 2010; Steinberger et al., 2015).

3.7.3 Further application to moonquakes and earthquakes

The methodology developed in this study may also be relevant for future work. We have applied PCA methodology only to the A01 nest, but this technique could let us examine more moonquakes, as recorded in the Apollo data or in data collected by the new broadband seismometer on the Farside Seismic Suite package, expected to land on the far side of the Moon in 2025 (Panning et al., 2021).

Using PCA appears necessary on the Moon, but it could also be useful for events on Earth, particularly in situations where there is no clear first arrival or where network coverage is sparse.

3.8 Conclusion

In this work, we sought both to understand the origin of moonquakes that slip "backwards" and to constrain the relative magnitudes of tidal and tectonic stresses deep in the lunar interior. Our observation of two slip directions implies that moonquakes' reversed polarity waveforms result from an oscillating tidal stress, which encourages moonquakes to slip forwards, backwards, left, or right depending on the phase of the tide. To explain these varying slip directions, the tidal stresses, which have a magnitude around 0.1 MPa (Toksöz et al., 1977; Minshull and Goulty, 1988; Weber et al., 2009), must be larger than the local tectonic stress. Our observations thus imply that the tectonic stress near the A01 nest, at 900 km depth, is less than 0.1 MPa. That small tectonic stress may be employed in future modelling of the lunar interior. Further, the small stress implies that viscous thermal runaway, which requires a large stress for initiation (Thielmann et al., 2015), is unlikely to explain the existence of deep moonquakes.

4

Using principal component analysis to improve relative arrival times of deep moonquakes

Contents

4.1 Introduction 81
4.2 Searching for relative time-shifts of deep moonquakes 83
4.2.1 Applying principal component analysis to deep moonquake waveforms 83
4.2.2 Assumptions 85
4.2.3 Solving a minimisation problem for time-shifts 86
4.2.4 Testing waveform alignment 88
4.3 Synthetic verification 89
4.3.1 Generating synthetics 89
4.3.2 Aligning identical waveforms 89
4.3.3 Aligning similar waveforms 90
4.4 Real deep moonquakes 94
4.4.1 Selecting deep moonquake stacks 94
4.4.2 Aligning deep moonquake stacks 95
4.5 Discussion 96
4.5.1 Implications for moonquake locations 96
4.5.2 Implications for lunar interior 98
4.6 Conclusion 99

Abstract

The scattered nature of the lunar waveforms often makes picking P- or S-arrivals challenging, meaning that the uncertainty on the arrival times can be up to ∼10 seconds for P-arrivals and ∼4 seconds for S-arrivals. The uncertainty of the arrival times limits our ability to use this data to locate deep moonquakes and image the lunar interior. In order to reduce the uncertainty of the arrival times, we align deep moonquakes to a reference event using principal component analysis. We hypothesise that even though recorded moonquakes occur at different locations and their seismic waves take different paths, some parts of the paths and therefore the seismic signal are similar. We search for the time-shift between waveforms that will maximise the coefficient of the first principal component, which contains the signal common to many moonquakes. Not all real deep moonquake stacks can be aligned, which could be because our search for relative time-shifts is not converging or because the waveforms are different for stacks of waveforms from nests in different locations. However, the method aligns the P-arrivals of 20 - 40 % of the real deep moonquakes to within 1.5 seconds of the reference event – a significant improvement relative to the original absolute error of up to 10 seconds. Using these new arrival times with reduced uncertainty to relocate deep moonquakes could reduces the uncertainty in epicentral distance from ∼35° to ∼2°.

Plain language summary

Deep moonquakes repeatedly happen in the same locations, referred to as “nests”. Locating these deep moonquake nests requires an accurate velocity model of the lunar interior and accurate arrival times of seismic phases. But accurately determining the arrival times of seismic phases remains challenging because of the scattered nature of lunar waveforms. In this study, we aim to reduce the uncertainty of the arrival times of deep moonquakes by aligning them to a reference event. We hypothesise that if deep moonquakes from different locations have similar waveforms, we can use principal component analysis to recover this similarity between waveforms and

use this to align them. We search for the time-shift that maximises the coefficient of the first principal component, which can accommodate the signal that is common to many moonquakes. We find that principal component analysis can align the P-arrivals of ∼20 - 40 % of real deep moonquakes to within 1.5 seconds of the reference event, which is an improvement on the original error for deep moonquakes.

Key points

- The uncertainty of the P-arrivals of deep moonquakes can be up to 10 seconds.
- To reduce the uncertainty on arrival times, we align deep moonquakes to a reference event using principal component analysis.
- The P-arrivals of ∼20 - 40% of the real deep moonquakes are aligned to the reference event within 1.5 seconds.

4.1 Introduction

Deep moonquakes occur at near monthly intervals at depths between 700 and 1200 km, in discrete regions called "nests" (e.g., Nakamura et al., 1982; Nakamura, 2005a; Nakamura, 1978; Bulow et al., 2005; Lognonné et al., 2003). Of the ∼300 identified deep moonquake nests, only ∼100 have been located (Frohlich and Nakamura, 2009). Most of the nests that have been located are on the nearside of the Moon, where the Apollo seismic stations are also situated (Frohlich and Nakamura, 2009; Bulow et al., 2007; Nakamura, 2005a; Hempel et al., 2012). Only around 30 of the nests are likely to be on the farside (mostly on the lunar limbs) and no nests are found within 40 degrees of the antipode of the seismic network. It is still unclear if the asymmetric distribution of deep moonquakes results from a lack of seismicity on the farside of the Moon or a failure to detect or accurately locate them (Nakamura, 2005a; Qin et al., 2012; Lammlein, 1977).

One possible explanation for the observed distribution of deep moonquakes is that the farside, within 40 degrees of the antipode, is aseismic (Nakamura, 2005a; Wieczorek et al., 2006; Wieczorek et al., 2006). This would imply that the

lunar interior is structurally and dynamically asymmetric. Such a hypothesis is plausible, especially due to the crustal dichotomy that is observed on the Moon; the crust on the farside is almost 20 km thicker than the nearside (Wieczorek et al., 2013) and lacks the dark mare basalts and heat-producing elements of the nearside (Lawrence et al., 2003).

Alternatively, researchers may not have identified farside deep moonquakes. Structures deep in the lunar interior could prevent us from observing deep moonquakes on the farside from the seismometers on the nearside. One proposed structure which could be responsible for this is a highly attenuating layer at a depth of around 1000 km. This layer would effectively mask deep moonquakes within 40 degrees of the antipode (Weber et al., 2009; Nakamura, 2005a).

To better understand the distribution of lunar seismicity, we need to locate deep moonquakes accurately. Deep moonquakes are located using a velocity model of the lunar interior and the arrival times of seismic phases. But accurately picking out these phases in the lunar waveforms is non-trivial (Nunn et al., 2020b). The lunar waveforms are characterised by emergent arrivals and an extended decaying coda that can last up to 2 hours, caused by the intense scattering of the waves in the lunar crust (Latham et al., 1970b; Latham et al., 1972; Dainty et al., 1974). The highly scattered waveforms effectively mask the arriving phases. Additionally, moonquake seismic signals are small; the largest recorded deep moonquake was only equivalent to a terrestrial M_w 3 (Goins et al., 1981), so it is often hard to identify the low amplitude seismic phases. Further complications arise because the arrival times of seismic waves are a function of both the event location and the lunar seismic velocity structure. When both the moonquake location and velocity structure are unknown, there is a trade-off: poor event location leads to error in the seismic velocity model, and error in the seismic velocity model leads to uncertainty in the event locations (Nunn et al., 2020b; Garcia et al., 2019).

To overcome some of the challenges associated with accurately picking the arrival times of seismic phases from the lunar waveforms, researchers use the repeated nature of deep moonquakes. As all the events from the same nest will have similar

waveforms, aligning and then stacking these similar waveforms will amplify the coherent signal over the noise (Bulow et al., 2007; Nakamura, 2005a; Lognonné et al., 2003; Yuan et al., 2021). From these stacks, the seismic phases can then be picked by eye. However, arrival times of the amplified seismic phases on stacked data show variation: by up to ∼10s for the P-arrival of deep moonquakes and ∼4s for the S- arrivals (Nunn et al., 2020b). For a deep moonquake with a hypocentre of 1200 km, an uncertainty of ∼10s for the P-arrival equates to an uncertainty in the epicentral distance of up to ∼35°.

In this study, we aim to reduce the uncertainty of the arrival times of deep moonquakes by using principal component analysis to align the waveforms relative to a reference event. First, we test this method on synthetic seismograms before applying it to real deep moonquake data.

4.2 Searching for relative time-shifts of deep moonquakes

We search for the time-shifts of deep moonquakes relative to a reference event. We do so by decomposing the deep moonquake waveforms using principal component analysis and searching for the time-shift between waveforms that maximises the coefficient of the first recovered principal component. Here, we describe applying principal component analysis to deep moonquake waveforms (Section 4.2.1), the assumptions we make to apply this to deep moonquakes from different locations (Section 4.2.2), and the algorithm we use to search for the best relative time-shifts between waveforms (Section 4.2.3).

4.2.1 Applying principal component analysis to deep moonquake waveforms

Principal component analysis (PCA) is a statistical method that transforms a set of possibly correlated observations into a set of linearly uncorrelated vectors called principal components (Bishop and Nasrabadi, 2006).

4. Using principal component analysis to improve relative arrival times of deep moonquakes

PCA has previously been applied to problems in earthquake seismology. It has been used to identify dominant trends in earthquake locations (Ocaña et al., 2008), to identify similarities in recovered moment rate functions (Vasco, 1989; Vasco, 1990), and to determine moment tensors of earthquakes (Vavryčuk et al., 2017). But as yet PCA has not been applied to the common problem of aligning waveforms.

To align the waveforms, we consider a data matrix **U**. Each of the J columns of **U** contains a t-second long waveform of a deep moonquake. Principal component analysis decomposes the matrix **U** such that each of the J waveforms (U_k) can be written as a weighted sum of the principal components:

$$U_k(t) = \sum_{j=1}^{J} G_j(t) m_{kj}, \tag{4.1}$$

where J is the number of input waveforms, k is the moonquake index, j is the principal component index, and t is time. **G** is a matrix where each row contains an orthogonal principal component that is a function of time t and has as many rows as input waveforms (J). The rows are ordered by their ability to explain the observations; the first principal component will contain the signal common to many of the deep moonquake waveforms. **m** is a matrix containing the principal component "coefficients": m_{kj} is the multiplication factor – the amount of principal component j needed to reconstruct waveform k.

When applying PCA to the waveforms, the alignment strongly influences the decomposition. A pair of identical waveforms that are perfectly aligned requires only a single principal component to fully reconstruct both waveforms. In contrast, for the same pair of identical waveforms with time-shifts between them, two principal components would be required to reconstruct both original waveforms and the time-shift between them. In this case, the second principal component would be a time-shifted version of the first. As such, we can align the waveforms by searching for the time-shift that maximises the coefficient of the first principal component.

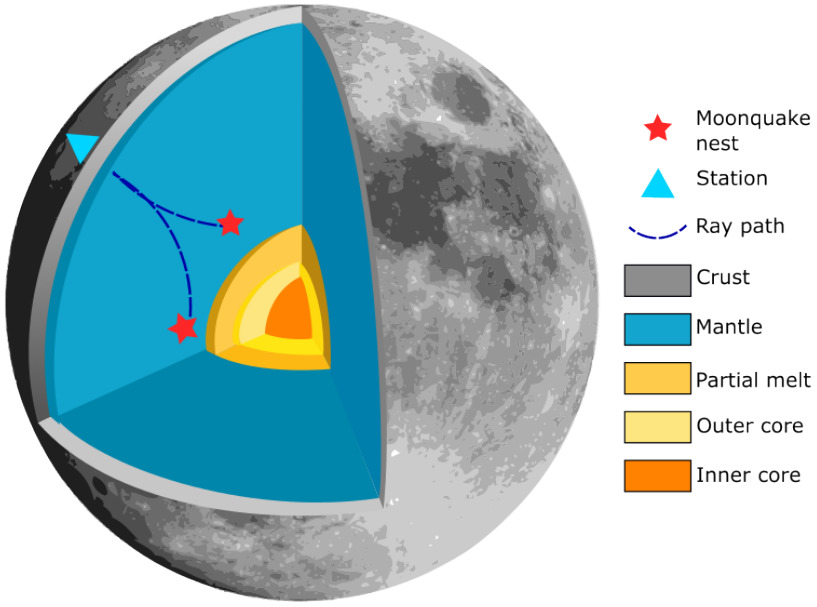


Figure 4.1: The ray paths of two deep moonquake nests (red stars) through the lunar mantle are illustrated by the dashed lines. The lunar mantle is illustrated in blue, the partial melt layer in orange, the outer core in yellow and the inner core in dark orange.

4.2.2 Assumptions

To align waveforms using PCA, we must assume that moonquakes from different nests have similar waveforms. We hypothesise that the lunar mantle is compositionally homogeneous, with seismic velocities increasing with depth as pressure and temperature increase (Figure 4.1). This is supported by 1-D velocity models of the interior of the moon (e.g., Nakamura, 1983; Toksöz et al., 1974; Lognonné et al., 2003; Khan and Mosegaard, 2002; Gagnepain-Beyneix et al., 2006; Weber et al., 2011). We also assume that the deep moonquakes have a simple source and short duration, leading to an impulsive moment rate function. Additionally, because their hypocentre is 700 - 1200 km below the surface, seismic rays arrive at the base of the thin "scattering layer" with a near-vertical incidence angle, as modelled using TauP (Crotwell et al., 1999), and illustrated in Figure C.1. The scattering layer is the uppermost layer of the moon consisting of fragmented eject blocks and a highly fractured crust (Blanchette-Guertin et al., 2012), called the "megaregolith". The range of published estimates of the thickness of the megaregolith layer is large – from a few hundreds of meters (Latham et al., 1972) up to 200 km thick (Gillet

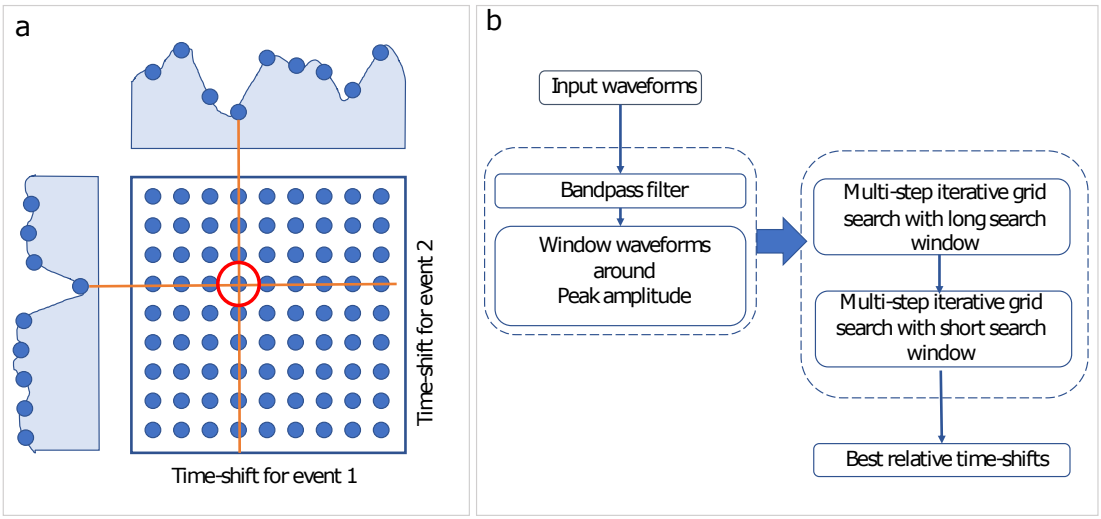


Figure 4.2: (a) Illustration of the multi-step iterative grid search in two dimensions. Each of the blue curves illustrates the objective function, which is sampled at each of the blue dots. We find the minimum of the objective function for event 1, and move the event to the time shift corresponding to this minimum. We then sample the objective function of event 2, find the minimum and move the event. (b) The steps needed to process the data and apply the multi-step iterative grid search.

et al., 2017). We assume a scattering layer of a few km thick, to allow us to assume a near-vertical incidence angle and a simple impulsive signal applied to the base of this layer as described above. When the simple impulsive signal from a deep moonquake reaches the top of the mantle, a stress is applied to the base of the scattering layer. The emergent arrivals, and long decaying coda of the waveforms results from intense scattering in this surface layer. We can then assume that the the deep moonquake waveforms recorded at a station at the surface are a linear combination of the same six stress tensor elements applied at the base of the scattering layer, which leads to similarities between the deep moonquakes from different locations.

4.2.3 Solving a minimisation problem for time-shifts

We formulate the search for the best time-shifts as a minimisation problem. The waveforms will be optimally aligned when the coefficient of the first principal component is maximised relative to the coefficients for all other principal components, allowing us to define an optimisation function at each time-shift (τ) between waveforms as:

$$L(\tau) = 1 - \frac{\sum_{k=1}^{J} |m_{k1}|(\tau)}{\sum_{j=1}^{J} \sum_{k=1}^{J} |m_{kj}|(\tau)}, \tag{4.2}$$

where m_{kj} is the principal component coefficient from Equation 4.1.

The minimisation of this function to align the waveforms is a high-dimensional problem. The number of possible solutions scales with the number of time-shifts to the power of the number of waveforms. As a result, a traditional grid search is computationally expensive even for a small number of waveforms. We also find that random search methods struggle to converge due to the complexity of the objective function – the value of the objective function can vary significantly over just a fraction of a second, the dominant period in the seismograms (as shown in the bottom row of Figure 4.4).

Consequently, we attempt to solve this complex multi-dimensional problem using a multi-step iterative grid search. We search for the best time-shift to align each event separately. A single event's waveform is shifted in time with steps of 0.15 seconds (1 sample), while all others remain fixed. At each time step, we calculate the value of the objective function (Equation 4.2). Once we have calculated the objective function for all time-shifts, we smooth the objective function using a Gaussian filter and take the minimum. The event's waveform is moved to the time-shift which corresponds to the minimum in the objective function. This process is repeated individually for each of the waveforms (Figure 4.2). The process is then iterated until the time-shifts for all of the waveforms are stable; normally around ten iterations.

We then repeat the steps with a smaller time window and smoothing kernel. We start with a search window of 750 samples and a Gaussian smoothing kernel filter width of 50 samples. We then repeat this with a reduced search window of 400 samples and a less smooth Gaussian filter with a filter width of 20 samples. Although we test different filter lengths and window lengths, we choose these parameters as they give satisfactory convergence in a reasonable amount of time (around 20 minutes on a desktop machine).

4. Using principal component analysis to improve relative arrival times of deep moonquakes

Although the multi-step iterative grid search is a time-consuming process, the advantages are that we can fine-tune the time window size or Gaussian filter and can test the convergence of the method robustly.

4.2.4 Testing waveform alignment

To assess the method, we quantify the improvement in the alignment of the waveforms. First, we apply the multi-step iterative grid search to waveforms recorded on the x-channel of the seismic instruments. We then test the resulting alignment using the waveforms recorded on the perpendicular instrument channel (the y-channel). The waveforms recorded on the y-channel should have the same relative time-shifts between waveforms, and so we take the best time-shifts determined from our PCA of the x-channel and apply them to the waveforms recorded on the y-channel. If there is an improvement in alignment, the coefficient of the first component determined from data recorded on the y-component will increase relative to the unaligned waveforms.

Next, we determine which waveforms are "well-aligned" and which are "poorly aligned". To do so, we compare the value of the objective function of the aligned waveforms to the value that would occur by chance, determined by adding a random shift to each event. We add random time-shifts between 0 and 1.5 or 10 seconds to each waveform recorded on the y-channel, keeping all others fixed to the best-aligned position. We then take the difference between the value of the objective function for the best-aligned waveforms and the objective function when a random shift has been added. If we add a random shift to a waveform that is well aligned, we should observe a large difference in the objective function (Equation 4.2). If we add a random shift to a poorly aligned waveform, we should observe a smaller difference in the objective function. We add a random shift to each event 1000 times and take the mean and the standard deviation (70^{th} percentile) of all the objective function differences for each event. This is illustrated by the blue line and shaded region in Figures 4.5 - 4.9.

Finally, we quantify what a "large" or "small" difference in the objective function is. To do so, we add a random shifts to unaligned waveforms, and measure the influence this has on the objective function. The difference in the objective function between the two random states essentially describes the improvement in waveform alignment by chance. Again, we repeat this 1000 times and take the mean. This is illustrated by the black dashed line in Figures 4.5 - 4.9. We can then use this to tell if a waveform is well aligned; if the change in the objective function calculated from adding a random shift to the aligned waveforms is larger than we expect by chance, then the waveform is well aligned.

4.3 Synthetic verification

We begin our analysis by testing PCA alignment on synthetic waveforms, where we know the relative time-shifts between the waveforms.

4.3.1 Generating synthetics

We create 100-second-long synthetic waveforms by combining principal components and coefficients. First, we generate random time series, which act as the principal components. Next, a random coefficient for each component for each synthetic waveform is generated. We then create the synthetic waveforms by multiplying the components with the coefficients. The synethtics are tapered with a Hanning taper of 60 seconds to simulate the emergent signals of the moonquakes and random noise is added to these signals. Finally, the synthetics are bandpass filtered between 0.25 - 1.75 Hz. Figure 4.3 shows an example synthetic waveform. These synthetic waveforms are then "misaligned", ready to be re-aligned.

4.3.2 Aligning identical waveforms

We start with a very simple case of identical synthetic waveforms generated from a single component, which have been shifted by a maximum of 15 seconds. The first panel in Figure 4.4 shows the objective function for synthetics generated from a single component. There is a clear minimum in the objective function

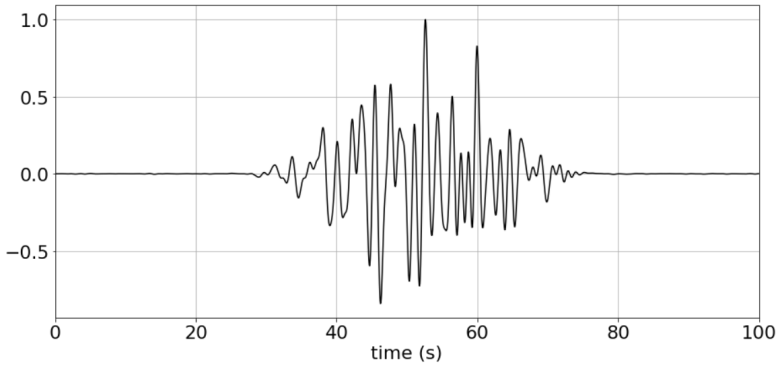


Figure 4.3: Top: Example of synthetic waveform created by combining coefficients of 6 principal components. In this example, the signal is 600 times larger than the noise.

at the correct time-shift – the waveforms can be aligned to an accuracy of 0.15 seconds (the signal's sample rate).

4.3.3 Aligning similar waveforms

Having aligned identical waveforms successfully, we now aim to align non-identical but similar waveforms. We generate synthetics using six principal components. The six components model the six stress tensor elements we hypothesise are applied to the base of the scattering layer (Section 4.2.2).

Figure 4.4 shows the shape of objective functions for synthetics generated using between 1 and 6 components, with the objective function for one component on the top left, and six on the bottom right. As we include more components, the minima become broader, leading to less accuracy in the alignment. Including more components also increases the size of the local minima, making optimising the problem more challenging.

Figure 4.5 shows a synthetic example generated using six principal components, where the true shifts between the waveforms are recovered within 0.5 seconds. The top panel shows the original unaligned waveforms recorded on the x-channel. The second panel shows the aligned waveforms on the x-channel. The third panel shows waveforms recorded on the y-channel, aligned using the shifts from the x-channel. Finally, the bottom panel shows the difference between the value of the objective function for the best-aligned waveforms and the objective function when a random

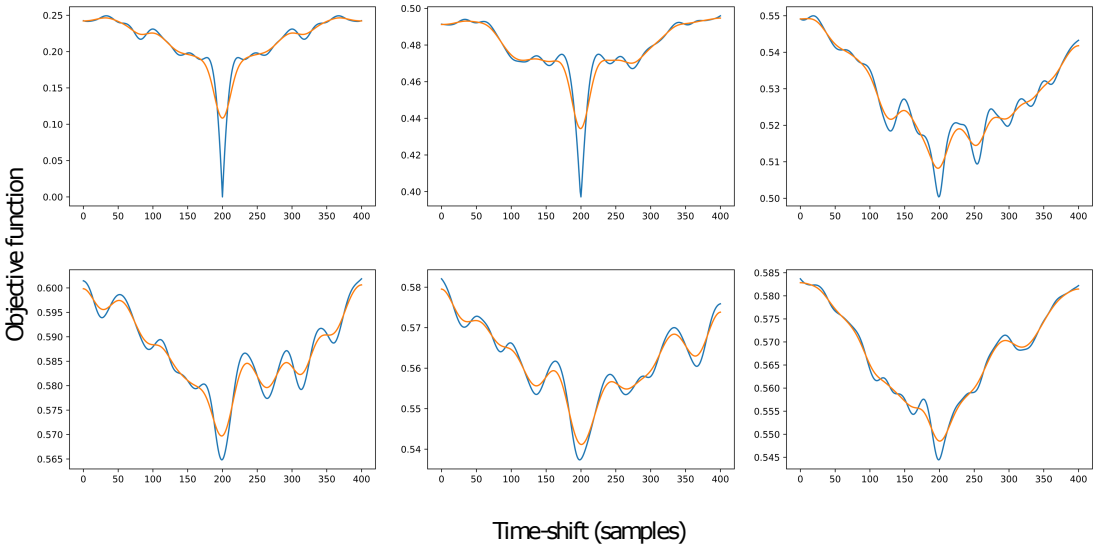


Figure 4.4: Objective functions for the relative time-shifts between synthetic waveforms. Each panel has synthetics generated using 1, 2, 3, 4, 5, and 6 principal components (from left to right and top to bottom). The search window is 400 samples long. The blue line in each panel is the unsmoothed objective function, and the orange line is the smoothed objective function calculated using a Gaussian filter with a width of 20 samples.

shift of between 0 and 1.5 seconds is added to each waveform. The light blue region is the standard deviation (70^{th} percentile) of the difference between the minimum objective function and the average value of the objective function when each event is randomly shifted. The black dashed line is the difference between the value of the objective function for the randomly aligned waveforms and the objective function when a random shift of between 0 and 1.5 seconds is added to each randomly aligned waveform. Since the blue shaded region is above the black dashed line for all waveforms, they are all well aligned within 1.5 seconds.

Figure 4.6 shows a synthetic example where three waveforms are poorly aligned. The highlighted orange waveforms are unaligned by 8 seconds. In the bottom panel, the difference in the objective function, shaded in blue, falls below the alignment expected from a random shift for the poorly aligned waveforms (black dashed line). We can therefore distinguish between waveforms that are well aligned relative to one another and those that are poorly aligned.

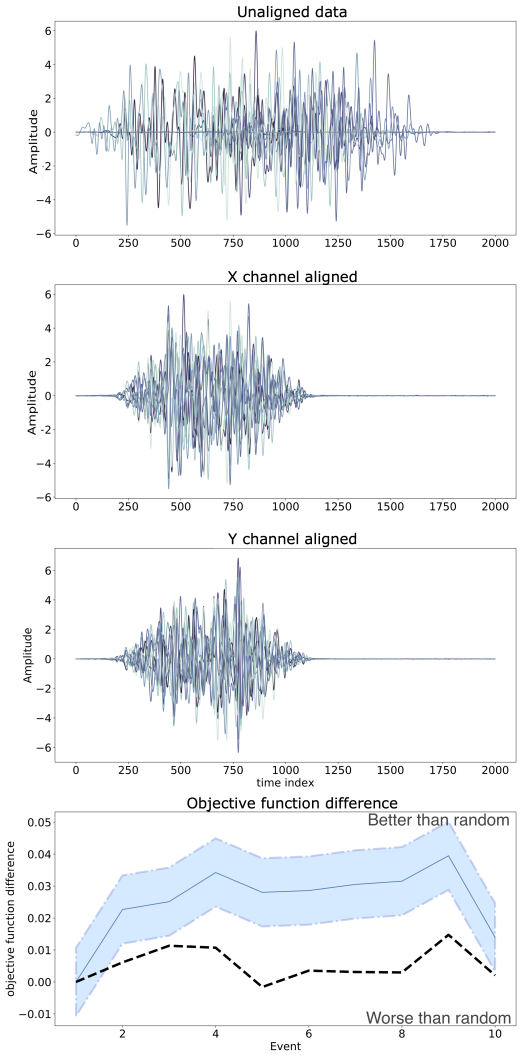


Figure 4.5: Top: The unaligned synthetic waveforms recorded on the x-channel. Each event is coloured in a different shade of blue. **Second:** The aligned synthetic waveforms recorded on the x-channel. The recovered shifts are within 0.5 seconds of the true shift. **Third:** The synthetic waveforms recorded on the y-channel aligned using the time-shifts recovered from the x-channel. **Bottom:** Y-channel objective function changes. Blue line shows the difference between the minimum objective function and the average value of the objective function when each event is randomly shifted by between 0 and 1.5 seconds. The blue line is calculated from the average 1000 random shifts for each event. The light blue region is the standard deviation (70^{th} percentile) of the difference between the minimum objective function and the average value of the objective function when each event is randomly shifted. The black dashed line is the difference between the objective function of randomly aligned waveforms and when each waveform is again randomly shifted.

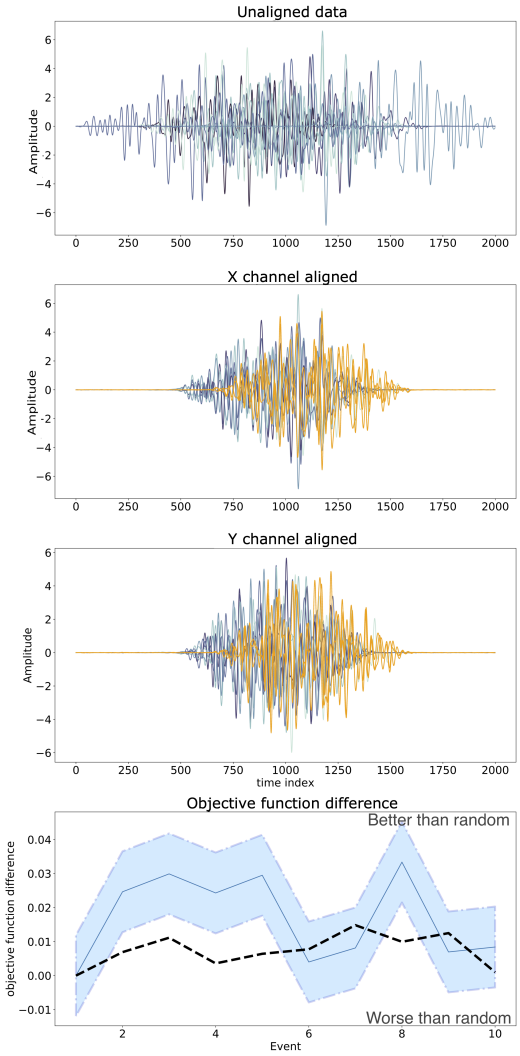


Figure 4.6: Top: The unaligned synthetic waveforms recorded on the x-channel. Each event is coloured in a different shade of blue. **Second:** The aligned synthetic waveforms recorded on the x-channel. The orange waveforms are misaligned from the true shift by up to 8 seconds. **Third:** The synthetic waveforms recorded on the y-channel aligned using the time-shifts recovered from the x-channel. **Bottom:** Y-channel objective function changes. Blue line shows the difference between the minimum objective function and the average value of the objective function when each event is randomly shifted by between 0 and 1.5 seconds. The blue line is calculated from the average 1000 random shifts for each event. The light blue region is the standard deviation (70^{th} percentile) of the difference between the minimum objective function and the value of the objective function when each event is randomly shifted. The black dashed line is the difference between the objective function of randomly aligned waveform and when each waveform is again randomly shifted. The orange events (waveforms 6, 7, and 9) fall below the threshold and are poorly aligned.

4.4 Real deep moonquakes

Having verified that PCA can be used to align synthetic waveforms, we now apply the method to real deep moonquake data.

4.4.1 Selecting deep moonquake stacks

We use deep moonquake stacks, which combine many deep moonquakes from a single nest to create an "average" trace with reduced noise. Nunn et al. (2020b) published 3 sets of deep moonquake stacks in miniSEED format (Bulow et al., 2007; Nakamura, 2005a; Lognonné et al., 2003). We use the most recent stacks created by Bulow et al. (2007). The stacks are an hour and 10 minutes long and include the more recent deep moonquakes identified in Bulow et al. (2005). An example stack is illustrated in Figure 4.7. At stations S12 and S16 we pick high amplitude stacks with clear onsets and no large spikes for this analysis. At station S12, we test the method on 11 stacks, and at station S16 on 8 stacks. Figure 4.8 shows the locations of the deep moonquake nests that produce the events used to create the stacks. The stacks are bandpass filtered between 0.25 - 1.75 Hz. We cut the stacks to an 80-second window, starting 100 seconds before the maximum amplitude. We choose this window intending to isolate the first arrivals, and we confirm that this window includes an arrival for the reference event. In this analysis, we align all the real deep moonquakes relative to the A022 nest. For this initial test, we

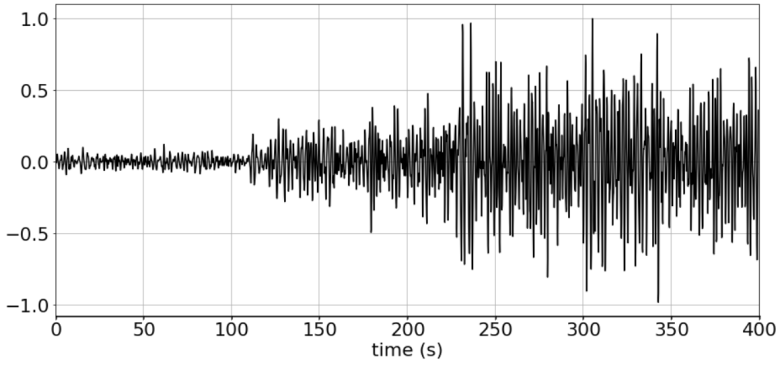


Figure 4.7: Example of the Bulow et al. (2007) stack for the A96 nest. The waveform has been bandpass filtered between 0.25 - 1.75 Hz.

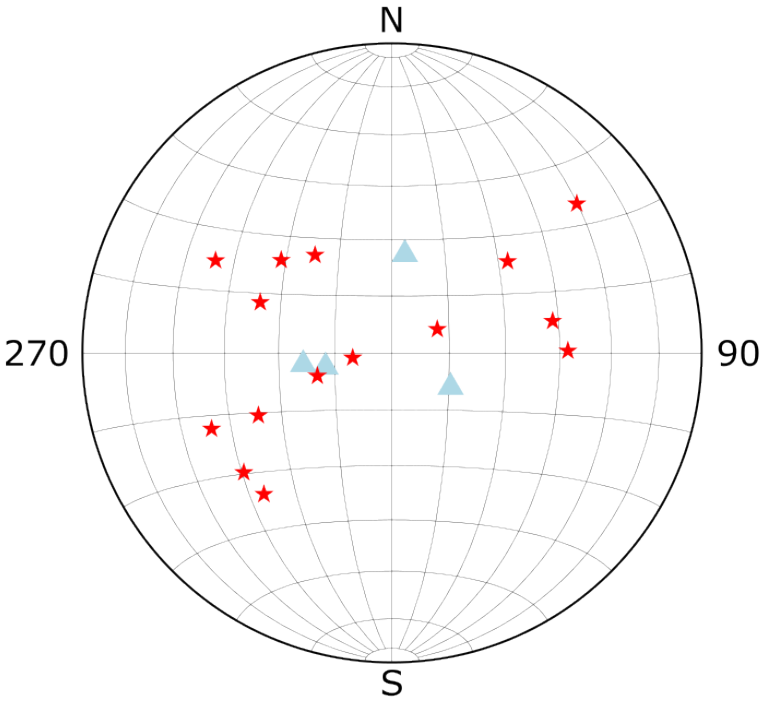


Figure 4.8: Location of the deep moonquake stacks used in this study. The blue triangles are the Apollo seismic stations and the red stars are the locations of the deep moonquakes from Nakamura (2005a).

also limit our analysis to waveforms that have some similarity with the template event, measured by a cross-correlation of greater than 0.5 in a 3 minute window around the maximum amplitude arrival. We find that aligning the waveforms using a different template does not significantly change our results.

4.4.2 Aligning deep moonquake stacks

First, we apply the multi-step iterative grid search to the eight high amplitude deep moonquake stacks recorded on the x-channel of station S16.

The top panel of Figure 4.9 shows the original unaligned data on the x-channel. The second panel shows the aligned waveforms on the x-channel. The third panel shows the y-channel data, aligned using the shifts from the x-channel. Visually there seems to be an improvement in the relative alignment of the waveforms in both of these panels. The coefficient of the first component determined from the y-channel increases by ∼15%, quantitatively suggesting an improvement in the alignment.

Finally, the bottom panel shows the difference in the objective function between the final best alignment for the y-channel and the objective function when we randomly shift each event by 10 seconds. Three waveforms are aligned to better than 10 seconds with 70% confidence, as illustrated by the shaded blue region in Figure 4.9 above the black dashed line. All but two of the waveforms are aligned by better than 10 seconds, as illustrated by the solid blue line being equal to or above the black dashed line. We also test random shifts of 0 - 1.5 seconds (Figure C.2). Three of the stacked waveforms seem to align to within 1.5 seconds. Of the three stacks aligned to better than 10 seconds with 70% confidence, one event aligns within 1.5 seconds with 70% confidence. However, none are aligned to sample accuracy.

Similar results are obtained using 11 high-quality deep moonquakes recorded at station S12 (Figure C.3) – 6 out of the 11 chosen stacked waveform are aligned by better than 1.5 s, and three are aligned by better than 1.5 seconds with 70% confidence.

4.5 Discussion

In this study, we have shown that principal component analysis can successfully align complex waveforms. The analysis works even for synthetic waveforms with lower similarity generated from 6 principal components. When applying this method to real deep moonquake stacks, the P-arrivals of ∼20 - 40 % of the real deep moonquakes are aligned to the reference event within 1.5 seconds. A relative alignment of 1.5 seconds is better than adding a random shift and an improvement on the possible 10-second error for these waveforms.

4.5.1 Implications for moonquake locations

Using these new arrival times with reduced uncertainty to relocate deep moonquakes could reduces the uncertainty in epicentral distance from ∼35° to ∼2°. However, to improve deep moonquake locations, we would need to reduce the error on phase picks of many moonquakes at the stations across the network.Currently, we observe that many moonquakes remain unaligned, limiting this method's current ability

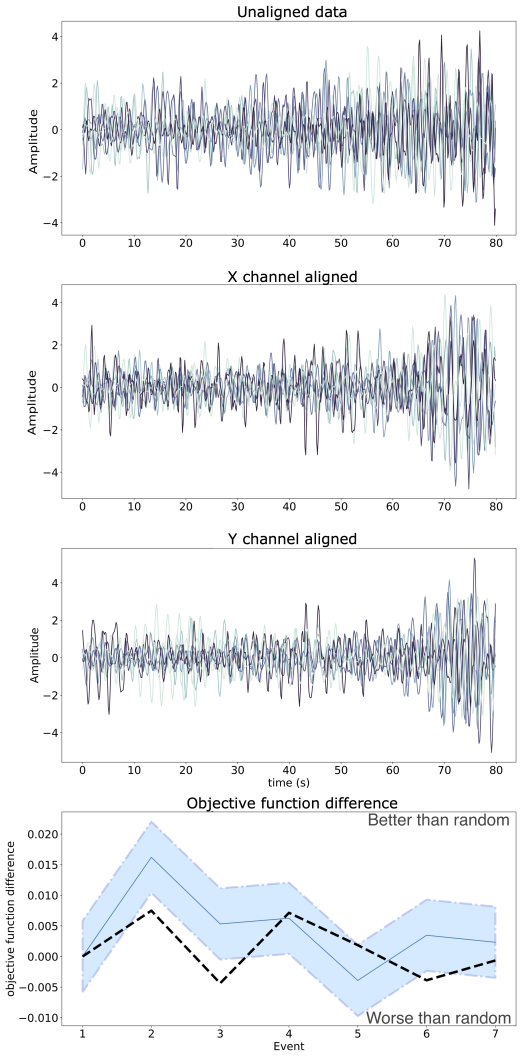


Figure 4.9: Top: 8 unaligned deep moonquake stacks recorded on the x-channel at station S16. Each event is coloured in a different shade of blue. **Second:** Waveform recorded on the x-channel aligned relative to the A022 stack. **Third:** Waveform recorded on the y-channel aligned using the time-shifts recovered from the x-channel. **Bottom:** Y-channel objective function changes. Blue line shows the difference between the minimum objective function and the value of the objective function when each event is randomly shifted by 10 seconds. The blue line is calculated from the average 1000 random shifts for each event. The light blue region is the standard deviation (70^{th} percentile) of the difference between the minimum objective function and the value of the objective function when each event is randomly shifted. The black dashed line is the difference between the objective function of randomly aligned waveforms and when each waveform is again randomly shifted.

to relocate deep moonquakes. We suggest two reasons here why the waveform alignment is unsuccessful for some of the real deep moonquakes.

First, it could be that the iterative grid search is not converging. If the objective function in high dimensional space is too complex, the global minimum may not be found with our multi-step iterative grid search. For example, suppose the amplitude of the waveforms has a larger influence on the objective function than the phase. In that case, the waveforms may align to the maximum amplitude instead of the true relative shift. With access to a high performance computing cluster, a full grid search with a newly defined objective function could be carried out on a small number of high-quality stacked waveforms for the optimum relative shift. From these well-aligned stacks, other stacks could be iteratively aligned.

A second possibility is that our assumption about the Moon's interior is incorrect. We previously assumed that the lunar interior is compositionally homogeneous, which means that moonquakes from different locations will have similar path effects. Hence, the deep moonquake waveforms can be modelled as a linear combination of 6 stress tensors applied to the base of the scattering layer. However, if this assumption is incorrect (i.e., if the lunar interior is heterogeneous), there may be a path effect introduced before the seismic waves reach the base of the scattering layer. Therefore, the waveforms may not be not similar enough for us to assume that they can be modelled by a linear combination of 6 stress tensors applied to the base of the scattering layer; only pairs of closely spaced deep moonquakes could be aligned in this way.

4.5.2 Implications for lunar interior

If poorly aligned stacked waveforms result from differences in the waveform, we may be able to interpret this in terms of structure in the interior of the Moon. There is only one event recorded at station S16 that we cannot align to less than 10 seconds error with 70% confidence (Event 5 in Figure 4.9). This is the A096 deep moonquake nest on the Moon's farside at the south pole. Our inability to

align this event could suggest a significantly different waveform, possibly due to a locally different structure at the lunar south pole.

However, those that are aligned well are not closely spaced, as shown in Figure 4.8. The well-aligned deep moonquakes are not clustered and span the whole nearside of the Moon, implying that the lunar interior is mostly homogeneous in the frequency band studied, at least on the nearside.

4.6 Conclusion

We use principal component analysis to align waveforms from different locations in the Moon. We first verify this method with simple synthetic waveforms. We show that by searching for time-shifts between waveforms that maximised the energy in the first principal component, we can successfully align complex waveforms, even those with lower similarity, such as the synthetic waveforms generated from 6 principal components. When we apply this new principal component analysis alignment technique to real moonquake data, not all the moonquakes can be aligned. The stacks we cannot align could be because our iterative grid search for relative time-shifts is not converging. Alternatively, unaligned stacks may be related to waveform differences from stacks of events from nests that occur in different locations on the Moon. However, we still find that we can align the P-arrivals of ∼20 - 40% of the real deep moonquakes to within 1.5 seconds of the reference event – a significant improvement on the absolute error of up to 10 seconds. Although we would need more relative time-shifts across the network to relocate the deep moonquakes, the method has shown promising results for reducing the arrival time error of deep moonquakes. Using these new arrival times with reduced uncertainty to relocate deep moonquakes could reduces the uncertainty in epicentral distance from ∼35° to ∼2°.

5

General conclusions and perspectives

Contents

5.1 Chapter aims 101
5.1.1 Chapter 2: Searching for partial ruptures in Parkfield, California 101
5.1.2 Chapter 3: Stresses in the lunar interior: insights from slip directions in the A01 deep moonquake nest 102
5.1.3 Chapter 4: Using principal component analysis to improve relative arrival times of deep moonquakes 103
5.2 Future work 104
5.3 Broader outlook 106
5.3.1 Repeating earthquakes 106
5.3.2 Lunar seismology 107
5.3.3 Earth analogues for deep moonquakes 109
5.4 Concluding remarks 110

In this thesis, I have used seismic observations to understand the processes that create and control repeaters in a range of environments across the Earth and the Moon. In this concluding chapter, I reflect on the work presented in this thesis, and present future avenues for research. In Section 5.1, I return to the aims for each chapter outlined in Chapter 1. In Section 5.2, I discuss some suggestions for future steps to build upon the work presented in this thesis, and in Section 5.3, I present a broader outlook on the field. Finally, in Section 5.4, I present my concluding remarks.

5.1 Chapter aims

In the introduction, I outlined 2-3 aims for each chapter. In this section, I reflect on these aims.

5.1.1 Chapter 2: Searching for partial ruptures in Parkfield, California

In Chapter 2, I focused on repeating earthquakes on the San Andreas Fault in Parkfield. These small magnitude repeating earthquakes happen less frequently than we expect if the earthquakes were accommodating all of the long term geodetic slip on the fault, which creates a slip deficit. I tested if this slip deficit could be explained by small magnitude events happening between repeaters (called "partial ruptures"). The first aim of this chapter was:

> *To use a simple location-based method to identify repeating earthquakes and partial ruptures.*

I identified co-located earthquakes without using waveform correlation. Instead, I considered two earthquakes to be a repeating pair when they were co-located within one rupture radius and had magnitudes within 0.3 magnitude units of each other. I considered a partial rupture to be an earthquake co-located within one rupture radius of a repeater, but with a magnitude at least 0.3 magnitude units smaller. I tested this method against a catalogue of repeating earthquakes identified using the more common waveform correlation criteria (Waldhauser and Schaff, 2021). I identified 77% of events in this catalogue. I then applied this method to address a scientific aim:

> *To test if partial ruptures can explain why repeating earthquakes happen less often than expected.*

I searched for repeating earthquakes and partial ruptures in Parkfield using the simple location method described above. Although I found that partial ruptures could accommodate up to ∼40% of the slip on the fault in each repeating earthquake cycle, it is not sufficient to account for the slip deficit for M 1-3 earthquakes.

Without additional complexity, models that use partial ruptures to account for the slip deficit are not viable.

5.1.2 Chapter 3: Stresses in the lunar interior: insights from slip directions in the A01 deep moonquake nest

In Chapter 3, I moved from analysing repeaters on Earth to analysing repeaters on the Moon. The monthly periodicities of most moonquakes suggest that they are at least partly excited by tidal stresses, but the exact relationship between the tidal stress and deep moonquakes is unclear. Are deep moonquakes driven by tidal stresses alone? Or do the tides act as a triggering mechanism on top of some long-term non-tidal ("tectonic") stress? In this chapter, I used deep moonquake observations to constrain the relative magnitudes of the tidal and tectonic stresses in the Moon. The first aim was:

> *To apply principal component analysis (PCA) to deep moonquake waveforms from a single nest.*

I decomposed deep moonquake waveforms using PCA into components that contain signals common to many moonquakes and components that just contain noise. I developed both quantitative and qualitative methods to separate components that contain signals from those that are noise. I found two of the recovered principal components contain signals common to many moonquakes, while the remaining components are noise. I then applied PCA to address the scientific aim:

> *To determine if moonquakes are driven by tidal or tectonic stress.*

To understand the driving stress of deep moonquakes, I focused on a subset of deep moonquakes which appear to slip backwards. The backwards-slipping events have waveforms which are flipped relative to other moonquakes in the same nest. I theorised that if tectonic stress is dominant, deep moonquakes from the same nest would only slip in a single direction (forwards and backwards). If the tidal stress is dominant, the fault can slip in any combination of forwards, backwards, left and right. I then interpreted the recovered principal components as slip directions. For a single slip direction indicative of a large tectonic stress, PCA would recover

only a single component common to many moonquakes. For many slip directions indicative of a large tidal stress, PCA would separate the waveforms into two principal components. I observed two principal components that differ from noise, which implied that the tidal stress is larger than the tectonic stress and is the cause of deep moonquakes. Using this result, I then constrained the tectonic stress to be smaller than the modelled tidal stress of 0.1 MPa. I hope this new constraint may be helpful for future studies, such as numerical models of cooling of the lunar magma ocean (e.g., Li et al., 2019), or to understand heterogeneity within the lunar interior (Qin et al., 2012; Zhao et al., 2008). Finally, I used this constraint on the magnitude of the lunar tectonic stress to address the final aim of Chapter 3:

> *To discriminate between possible mechanisms that could generate deep moonquakes*

I explored the possibility that the mechanism of deep moonquakes may be similar to that of intermediate-depth earthquakes (Frohlich and Nakamura, 2009). The possible mechanisms for deep moonquakes and intermediate-depth earthquakes include: fluids (Frohlich and Nakamura, 2009); thermal runaway (Thielmann et al., 2015); or a phase change (Weber et al., 2009). Using the new constraint on the size of the present-day stress in the lunar interior, I excluded thermal runway as a possible mechanism, as the present-day stresses in the lunar interior are too small.

5.1.3 Chapter 4: Using principal component analysis to improve relative arrival times of deep moonquakes

Finally, in Chapter 4, I continued my work on deep moonquakes. Lunar seismic signals are characterised by emergent arrivals and a long decaying coda that can last up to 2 hours, caused by intense scattering in the uppermost layers of the lunar crust. These highly scattered waveforms often make it challenging to pick distinct P- or S-arrivals and mask reflected phases and surface waves. The large uncertainty on the arrival times limits our ability to accurately locate deep moonquakes or image the lunar interior. In this chapter, I aimed to improve the relative timings of deep moonquakes from different locations in the moon. The first aim I addressed was:

To use principal component analysis to align waveforms

I found PCA could effectively align synthetic waveforms to within 1.5 seconds of the template waveform. The waveforms were optimally aligned when the coefficient of the first component was maximised. I was motivated to use PCA to meet the second aim of Chapter 4:

To improve the relative time-shift between deep moonquakes from different nests.

To apply this method to real deep moonquakes, we needed to assume that deep moonquakes from different locations in the moon produce similar waveforms. I hypothesised that when a simple impulsive signal from a deep moonquake reaches the top of the mantle, a stress is applied to the base of the scattering layer. This allows us to assume that there are similarities between the deep moonquakes from different locations, as they are a linear combination of the same six stress tensor elements applied at the base of the scattering layer. When I applied the method to real deep moonquake data, not all events could be aligned, which could be because our search for relative time-shifts is not converging, or because the waveforms are different for events from different locations. However, the method can align the P-arrivals of 20 - 40 % of the real deep moonquakes to within 1.5 seconds of the reference event – a significant improvement relative to the original absolute error of up to 10 seconds.

5.2 Future work

The research presented in each chapter has natural extensions, some of which I outline here:

- **Apply the slip direction method described in Chapter 3 to other moonquake nests.** In Chapter 3, I applied PCA to determine the slip direction of the A01 nest. The A01 nest contains the largest number of deep moonquakes, some of which are reversed polarity (Koyama and Nakamura, 1980; Weber et al., 2010; Goulty, 1979). Although in Chapter 3, I focused on these reversed polarity events, the method could also be used to infer the

slip directions in nests that do not contain reversed polarity events. This method could provide insights into the distribution of stresses across the lunar interior.

- **Extend the alignment of deep moonquake nests to map principal components to real Green's functions.** We still do not know the fault plane solution for individual deep moonquakes – an important tool to assess the stress state in the deep moonquake generating region. In Chapter 4, I hypothesised that there was some similarity between waveforms from different locations in the moon because they were composed of a linear combination of 6 stresses that were applied to the base of the scattering layer by the seismic waves. I then decomposed the waveforms into principal components – the signal common to many moonquakes. These principal components are theoretically the 6 stress components applied to the base of the scattering layer. It may be possible to map principal components to real Green's functions. The transformed weights of these Green's functions will then be equivalent to the relative moment tensor elements.

- **Apply principal component analysis to other datasets.** In this thesis, I have demonstrated PCA can be effectively applied to the lunar data to gain new insight. Therefore PCA may be a useful tool for analysis of other datasets, which could include:

  - The marsquake data– PCA could be used to align the marsquake data and look for similarities within the waveforms. PCA may be useful in relatively relocating the events at Cerberus Fossae Graben System on Mars (Drilleau et al., 2022).
  - The new lunar data – The Farside Seismic Suite will land at the lunar south pole in 2025, and will provide new lunar seismic data. PCA carried out in this thesis on the Apollo data may be useful for the new data, especially as it has been shown to work on single components and single stations.

– Repeating icequakes – Outside of extra-terrestrial seismology, PCA could be used to look for similarities in the repeating icequake sources, such as changes in slip direction, to further understand glacial dynamics.

5.3 Broader outlook

In this section, I provide a more general outlook on the state of the field for both repeating earthquakes in California and for repeating deep moonquakes and lunar seismology more generally. I draw upon the recommendations made in the SCEC 2022 science plan (Vidale et al., 2017), the EarthScope Science plan (Williams et al., 2010) and the Planetary Science and Astrology Decadal Survey (National Academies of Sciences, Engineering, and Medicine, 2022), which outline long-term science goals for the fields of fault mechanics and planetary science, respectively.

5.3.1 Repeating earthquakes

It has been nearly 25 years since Nadeau and Johnson (1998) first observed that repeating earthquakes happen less often than expected. Here, I make suggestions that I think could lead to progress towards the goal of understanding the recurrence of repeating earthquakes. I think that we may discover the answer to this problem in the next 10-15 years.

I believe that progress will likely be driven by 'the validation of model-based predictions against data' – a goal of the SCEC science plan. This comprises two parts – models of repeating earthquakes with additional complexity and new detailed observations of repeating earthquakes.

More complex models of repeating earthquakes could incorporate dynamic weakening (Thomas et al., 2014; Chen and Lapusta, 2019). Dynamic weakening is a range of proposed fault zone processes that decrease the strength of the fault as slip accelerates. Recent models suggest dynamic weakening may promote full ruptures over partial ruptures (Thomas et al., 2014). Seismic

observations that could help to test this model could be the recurrence-magnitude scaling recovered from repeating earthquakes, the predicted ratio of partial ruptures, and the stress drops of repeating earthquakes. A second complexity that modellers could incorporate is off-fault plasticity (Mia et al., 2022). Off-fault plasticity is where the region surrounding the fault is not elastic but can accumulate damage. Recent models suggest that fault plasticity may promote partial ruptures, but these partial ruptures can occur for earthquakes of all magnitudes. Seismic observations that could be used to test this model include the recurrence-magnitude scaling of repeating earthquakes, the predicted ratio of partial ruptures, or more complex temporal clustering of co-located earthquakes.

Along with more complex models, I think that these advancements will also be driven by a greater number and more complex observations of small-magnitude repeating earthquakes. An excellent example is the the high-resolution catalogue of repeating earthquakes carefully curated by Waldhauser and Schaff (2021). Additionally, we may gain greater insight and availability to test these models from observations of the finite source, such as stress drops or directivity estimates (e.g., Abercrombie, 2014; Dreger et al., 2007).

If we understand the physics that controls the recurrence times of repeating earthquakes, researchers may more robustly apply repeating earthquakes to geophysical applications. This includes tracking slip on faults and working towards the Earthscope aim of testing strain rate models along the San Andreas Fault.

5.3.2 Lunar seismology

The Apollo dataset is over 50 years old, and its importance cannot be overestimated. It has been pivotal in our understanding of the Moon's interior and dynamics. Nevertheless, many questions about the Moon remain unanswered and are key science questions outlined in the decadal survey

(National Academies of Sciences, Engineering, and Medicine, 2022). These include questions about the imaging the seismic structure of the lunar interior, the distribution of deep moonquakes and the mechanism of deep moonquakes.

Imaging the interior and the distribution of farside deep moonquakes are key goals of the Farside Seismic Suite (FSS, Panning et al., 2021). The FSS will be sent to the Schrodinger crater at the lunar south pole and is expected to land in 2025. The seismic package will comprise a 3-component short-period instrument and a vertical-component broadband instrument deployed on the lander's deck. It is estimated to operate for four months. The farside location of the new seismic instrument will likely have a high impact on providing new seismic paths through the deep lunar mantle needed to understand the structure of the lunar interior and will clearly define the farside seismicity rate. But the impact of this instrument on answering the key question about deep moonquake mechanisms is likely to be lower. It is a single station operating for only a short period of time, and the characteristics of the lunar data will remain the same.

An extensive geophysical network, with at least four nodes operating for 10 - 15 years, would open up many more possibilities for lunar seismicity (Yamada et al., 2011; Haviland et al., 2021; Kawamura et al., 2022). But until the lunar seismic network is operational, the Apollo data will likely remain a key dataset for researchers aiming to understand the mechanisms for deep moonquakes.

I suggest that a continued effort to recover these source properties of deep moonquakes from the Apollo era data may gain insight into the mechanism of these deep moonquakes. Currently, there are few estimates of the source properties of deep moonquakes. Only 3 events have estimated stress drops (Kawamura et al., 2017), only one nest has an estimated spatial extent (Nakamura, 2005b), and no deep moonquakes have robust estimates of focal mechanisms. Methods and codes that can be applied to the original Apollo

data and the new data collected by the FSS will be helpful for self-consistent estimates across the two datasets.

Similar to repeating earthquakes on Earth, I suggest that progress could be made by creating a simple model of tidally driven deep moonquakes. There are simple block models of the tidal triggering of earthquakes (Beeler and Lockner, 2003; Perfettini et al., 2001; Perfettini and Schmittbuhl, 2001), but in these models, the tectonic stress is many times larger than the tidal stress. These could be altered to the low-stress state of the Moon. But modelling stick-slip behaviour when the stress is close to zero could be challenging. Basic observations such as the timing of modelled moonquakes could easily be compared with real lunar observations.

5.3.3 Earth analogues for deep moonquakes

As highlighted throughout this thesis, intermediate focus earthquakes in subduction zones occur at similar pressures and temperatures to deep moonquakes and could make good Earth-analogues for deep moonquakes (Frohlich and Nakamura, 2009). Searching for the tidal triggering and understanding the mechanism of isolated clusters of intermediate-depth earthquakes could provide insight into deep moonquakes.

Deep moonquakes also have repeated slip, possibly making the faults smooth and weak. Mature crustal faults seem weak due to smoothing from large cumulative slip (Perrin et al., 2021), and may be a good Earth analogue for weak faults, albeit nowhere near as weak as moonquake faults. As yet, no quantitative comparison between earthquakes and deep moonquakes has been made, but combined research on the properties of Earth analogues and moonquakes may help us understand the physics of both.

5.4 Concluding remarks

In this thesis, I have analysed two types of repeating seismicity: repeating earthquakes in California and repeating deep moonquakes on the Moon. By identifying repeating earthquakes and partial ruptures from their locations, I found that partial ruptures cannot explain the slip deficit for M 1-3 earthquakes. Without additional complexity, a model that uses partial ruptures to explain the slip deficit is not viable. For repeating deep moonquakes, I applied principal component analysis to this 50-year-old data set. I have used PCA on waveforms from a single nest to recover the slip directions. I found two slip directions and infer deep moonquakes are tidally driven. I placed a new constraint that present day tectonic stress in the lunar interior must be smaller than the modelled tidal stress of 0.1 MPa. From this constraint, I ruled out thermal runaway as a generative mechanism of deep moonquakes. Finally, I applied PCA to deep moonquakes across the lunar interior to improve the relative timing. I have aligned the P-arrivals of 20 - 40 % of the real deep moonquakes to within 1.5 seconds of the reference event – a significant improvement relative to the original absolute error of up to 10 seconds.

In this thesis, I have tested theoretical models of repeating moonquakes and earthquakes and used observations to place new constraints on these models. The problems addressed in this thesis are decades old. Nevertheless, new careful analysis, partly due to the careful preservation and digital conversion of the Apollo seismic data, has generated new insights.

Appendices

A

Supporting information for "Searching for partial ruptures in Parkfield, California"

A.1 Derivation of slip in partial ruptures

From the model (Cattania and Segall, 2019), we wish to determine the predicted slip in partial ruptures. To do so, we again consider repeating earthquakes and partial ruptures occurring on locked patches loaded by the surrounding creeping fault. The slip in each earthquake (S) should match the surrounding fault creep (V_{creep}) that has been loading the asperity in the time since the last event (T_r): $S = V_{creep}T_r$. We follow the arguments of Cattania (2019), that the behaviour of the repeating earthquakes is controlled by the ratio of the slip required to nucleate an event (S_n) and the slip required for the earthquake to rupture the full patch (S_{full}). S_n increases as the nucleation size (R_∞) increases, whereas S_{full} increases with the size of the patch (R). If the slip required to nucleate an event is larger than the slip required for a full rupture, $S_n > S_{full}$, all ruptures are full ruptures. If the slip required to nucleate an event is smaller than the slip required for a full rupture, $S_n < S_{full}$, partial ruptures can occur. We define the ratio:

$$\frac{S_n}{S_{full}} \propto \sqrt{\frac{R_{inf}}{R}}. \tag{A.1}$$

When this ratio is less than 1, partial ruptures can occur. The minimum slip for a partial rupture is S_n, although in each cycle, there may be more than one partial rupture, therefore more slip. Therefore, the ratio $\frac{S_n}{S_{full}}$, gives the minimum ratio of partial slip to full slip. Partial ruptures occur from R $\sim 4.3R_\infty$ to $100R_\infty$, so in this parameter range, the slip ratio varies from $\sim$ 0.7 to 0.2.

A. Supporting information for "Searching for partial ruptures in Parkfield, California"

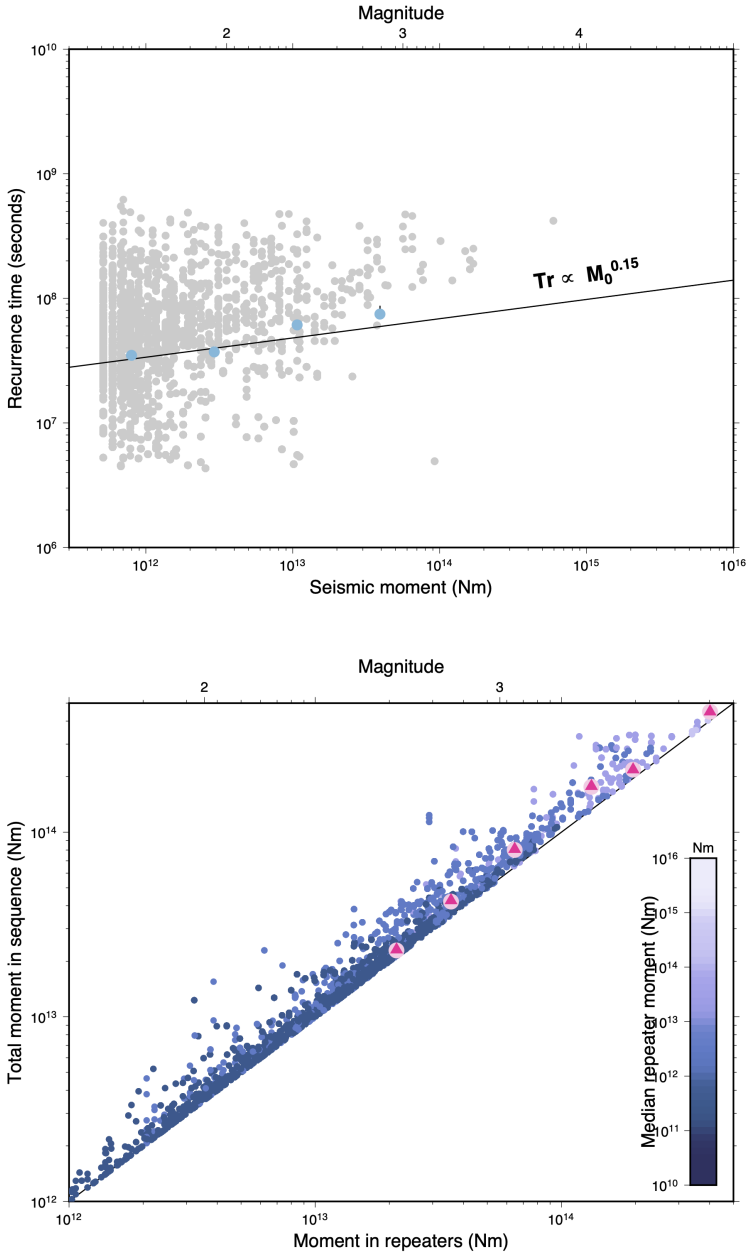


Figure A.1: Top: Median recurrence interval versus median moment for pairs of repeating earthquakes from the relocated Northern California catalogue (Waldhauser, 2013) on a log-log scale assuming a stress drop of 3 MPa. Individual values are plotted as grey circles, with medians for moment bins shown as blue circles. The error bars on the medians indicate 95% confidence limits, which were estimated via bootstrapping (details in the text). The best-fitting line is plotted in solid black with a gradient of 0.15. **Bottom:** The total moment in repeating earthquakes compared to the total moment in each repeater and its co-located events, including repeating earthquakes and partial ruptures. Each point is coloured by the median moment of the co-located repeating earthquakes. Light pink points are the binned means. The dark pink triangles are the binned means corrected for missing small events (see text for more details).

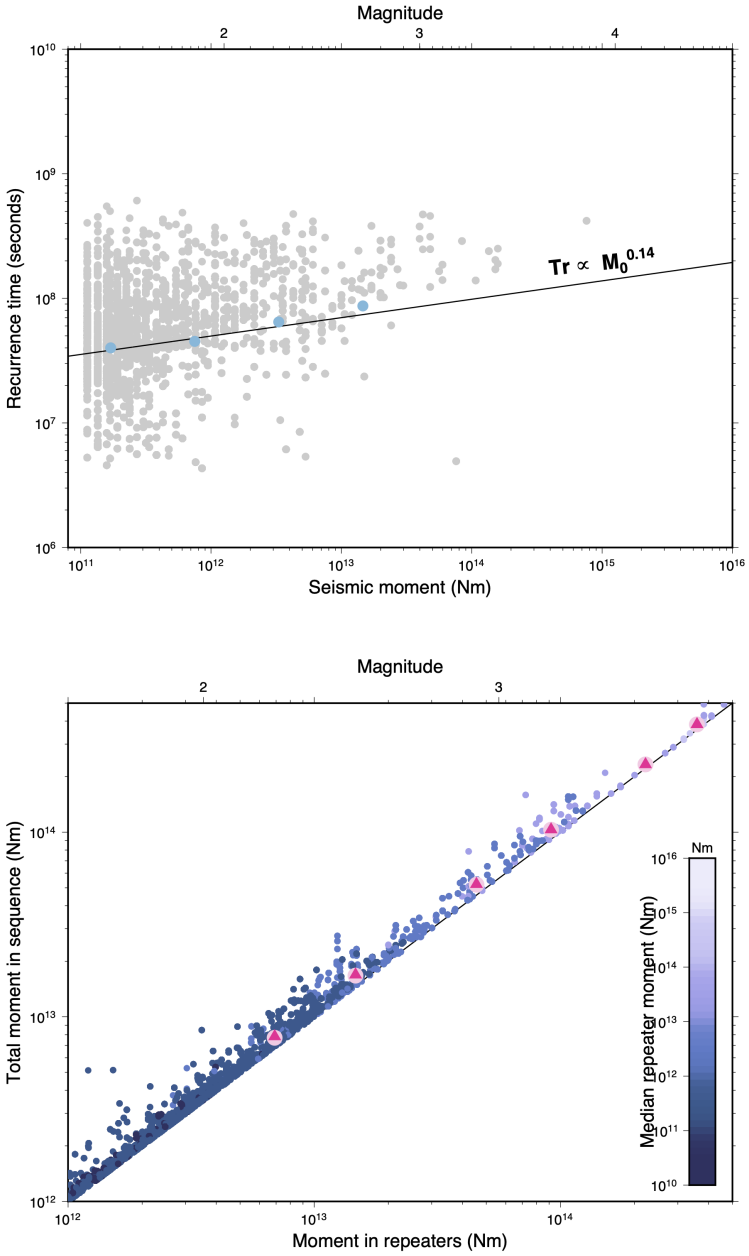


Figure A.2: Same as Figure A.1, but assuming a stress drop of 10 MPa, and a local magnitude scaling of $M_0 = 10^{1.51M+16.1}$.

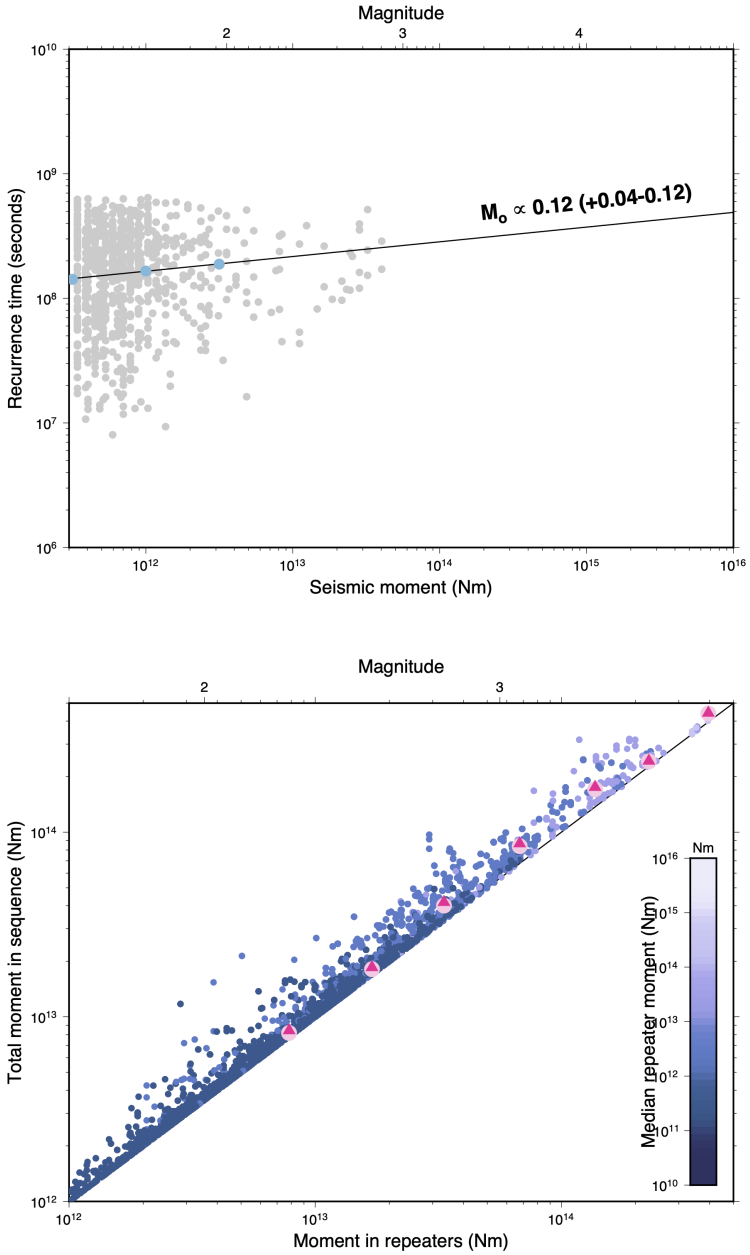


Figure A.3: Same as Figure A.1 but using the location error ellipse reported in the NCEC catalog. Repeating earthquakes and partial ruptures are only identified when the maximum error is located within the rupture radius.

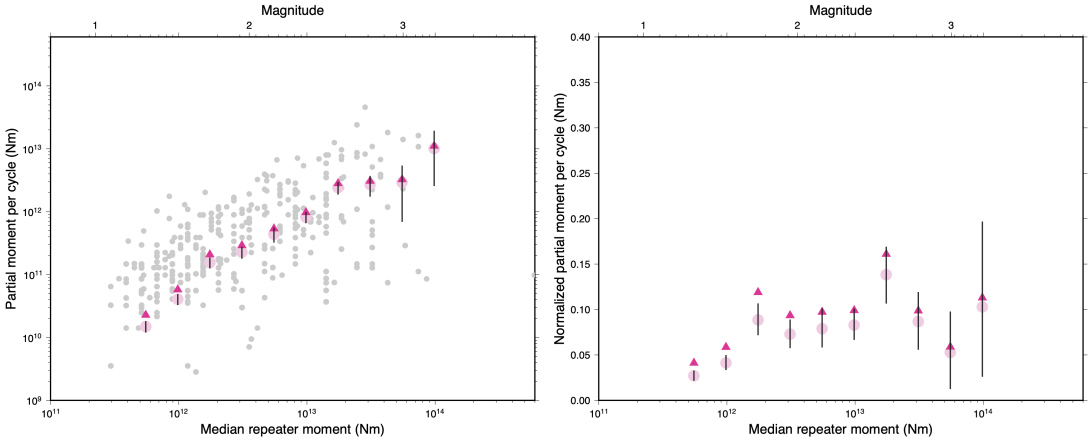


Figure A.4: Left: Total moment in repeating earthquakes to the total moment to partial ruptures, normalised by the number of repeating earthquakes of each repeater and its co-located events, identified using the 95^{th} percentile error ellipse in the NCEC catalogue (See main text for further description of method). Light pink dots show the binned averages from bootstrapping, following the same bootstrapping procedure described in the text. The grey lines show the 5^{th} and 95^{th} percentiles of these binned medians. The dark pink triangles are the corrected bin values, following the same correction described in the text. **Right:** Total moment in repeating earthquakes to the total moment to partial ruptures per cycle, normalised by the total moment in partial ruptures.

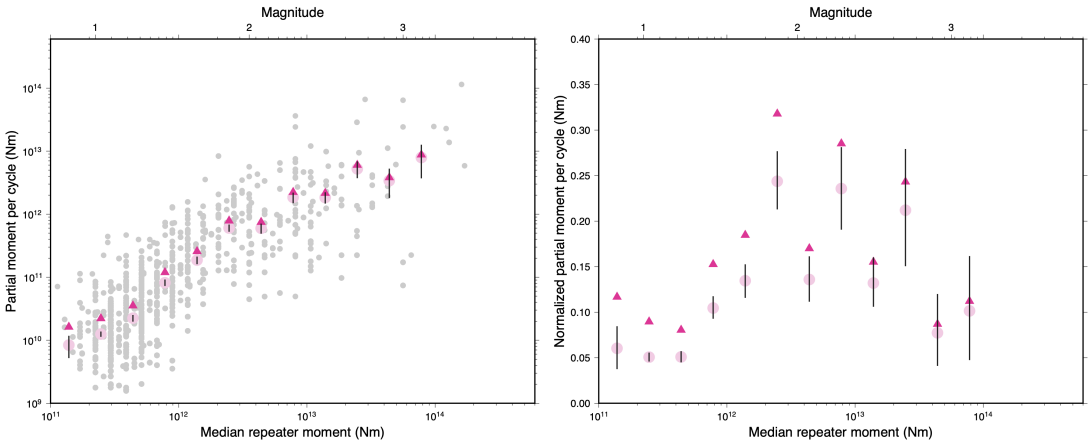


Figure A.5: Same as FigureA.4, but using partial ruptures of repeating earthquakes identified by Waldhauser and Schaff (2021).

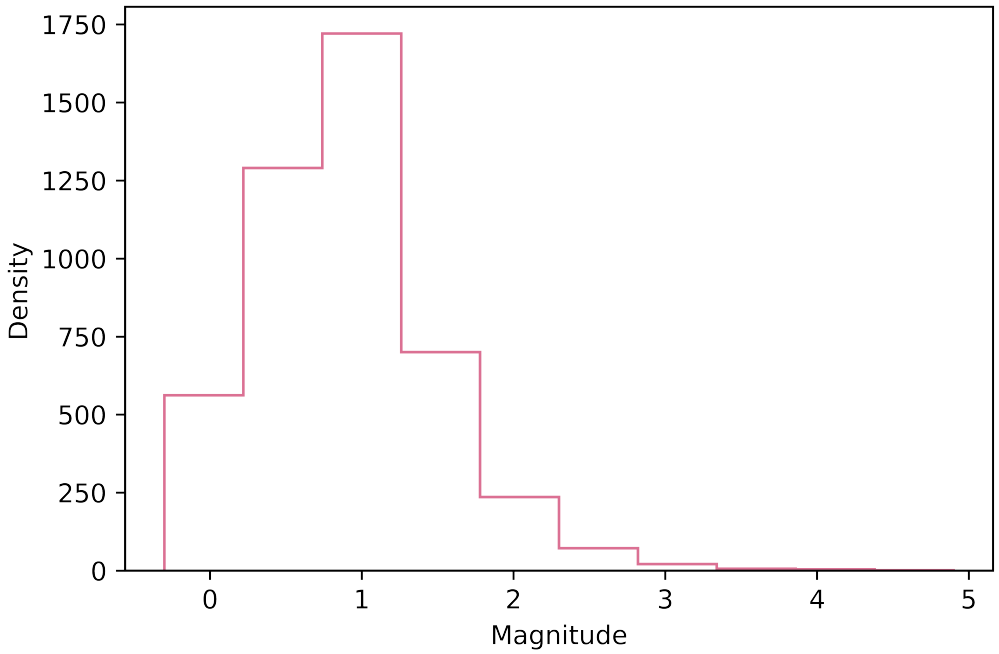


Figure A.6: Distribution of the magnitudes of events from the Waldhauser and Schaff (2021) repeating catalogue that were not identified in the catalogue of repeating earthquakes from the NCEC catalogue.

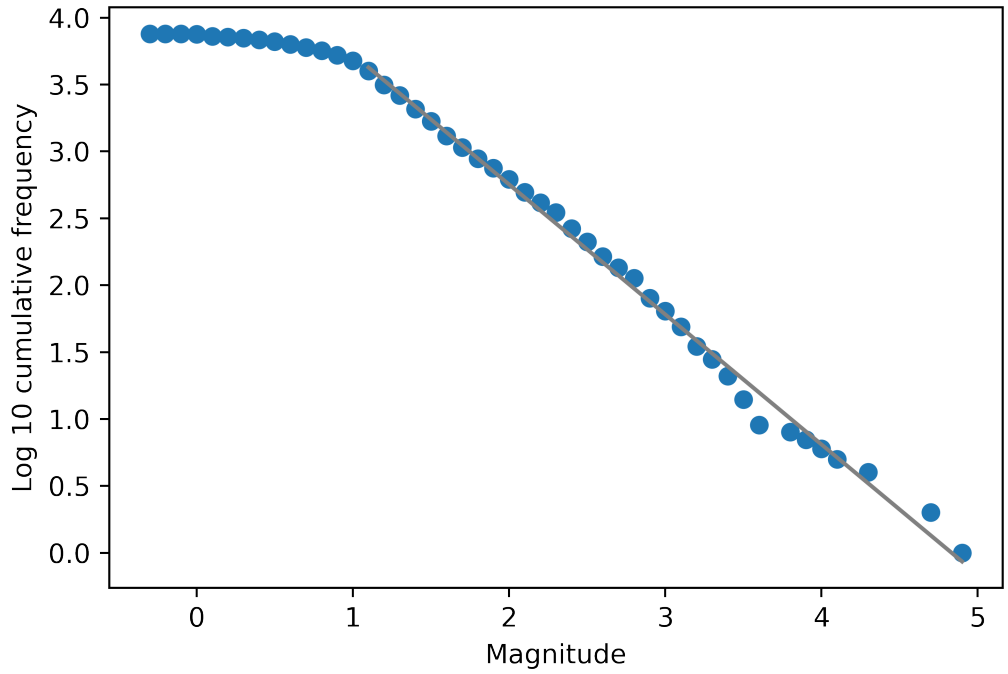


Figure A.7: Linear Gutenberg-Richter distribution for earthquakes in Parkfield.

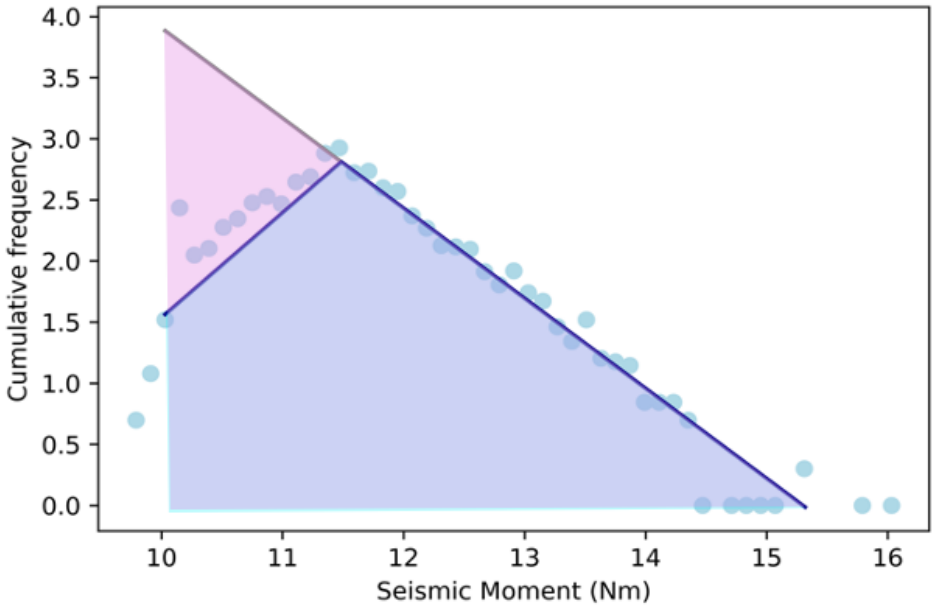


Figure A.8: Correction for the NCSN catalogues detection bias. Blue dots show the cumulative frequency of events in each magnitude. The blue line is the observed magnitude-frequency distribution, which has a positive slope below the magnitude of completeness. The grey line is the theoretical distribution – the distribution is extended to smaller magnitudes. To calculate the correction, for each magnitude repeater, we take the ratio of the area beneath the observed curve (blue) to the area below the theoretical curve (pink).

B

Supporting information for "Stresses in the lunar interior: insights from slip directions in the A01 deep moonquake nest"

Station	Instrument mode	Date and time of template event
S12	Peaked	23/04/1975 11:25
S12	Flat	20/01/1976 08:58

Table B.1: Template deep moonquake waveforms. Events are cross correlated with these template events in a 5 minute window around the first arrival. We choose events that have a maximum cross correlation value of greater than 0.3 in this window. The maximum cross correlation is then taken as the initial time shift to align the events. Finally, we check the events by eye to ensure no events with large data gaps in the time period of the first arrival. The same set of events are used on station S16.

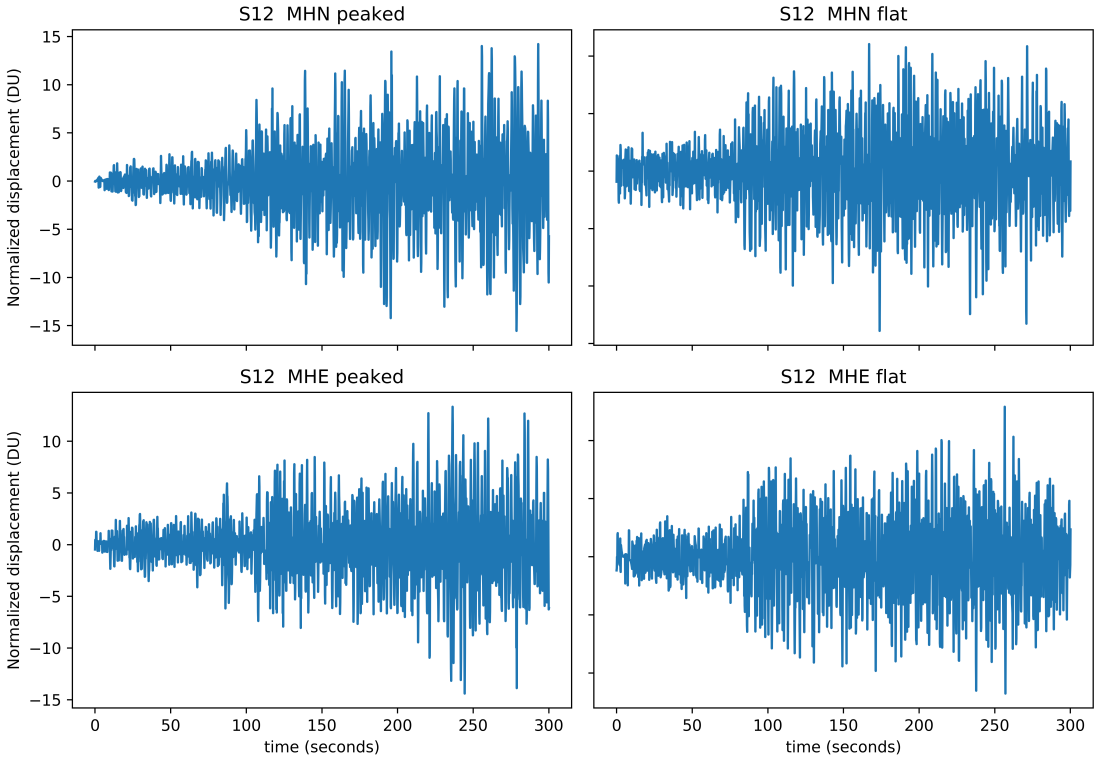


Figure B.1: Events used as the template event for each station and operational mode. Events are cross correlated with these template events in a 5 minute window around the first arrival. We choose events that have a maximum cross correlation value of greater than 0.3 in this window. The maximum cross correlation is then taken as the initial time shift to align the events. Finally, we check the events by eye to ensure no events with large data gaps in the time period of the first arrival. The same set of events are used on station S16.

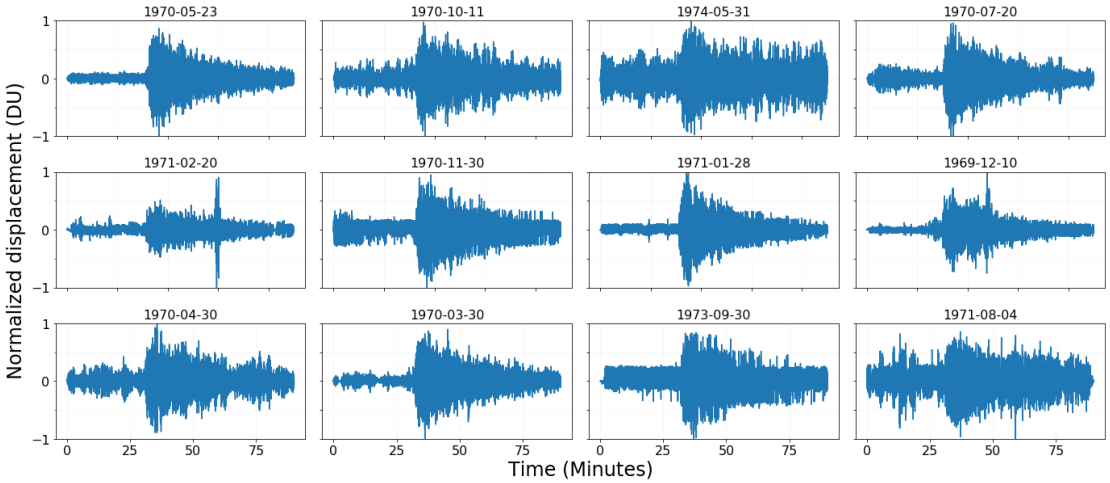


Figure B.2: Deep moonquake waveforms used for PCA decomposition, recorded at station S12, channel MHE, in the peaked operation mode.

Instrument mode	Reversed polarity events (date)
S12 MHN peaked	1974-05-31
	1973-08-29
	1973-09-30
S12 MHE peaked	1974-05-31
	1973-09-30
S16 MHN peaked	1973-01-20
	1977-05-29
	1977-03-31
	1977-05-27
	1977-08-17
S16 MHE peaked	1977-05-29
	1977-03-31
	1977-05-27
	1975-03-27
	1977-08-17

Table B.2: Reversed polarity waveforms. In the data recorded at station S16 in the peaked mode there are 5 reversed polarity events. In the data recorded at station S12 in the peaked mode, there are 3 reversed polarity events. Due to the time the instrument was operating in flat mode, we do not identify any reversed polarity events in these subsets of the data. Nevertheless, we apply the same analysis to understand how the slip direction vary.

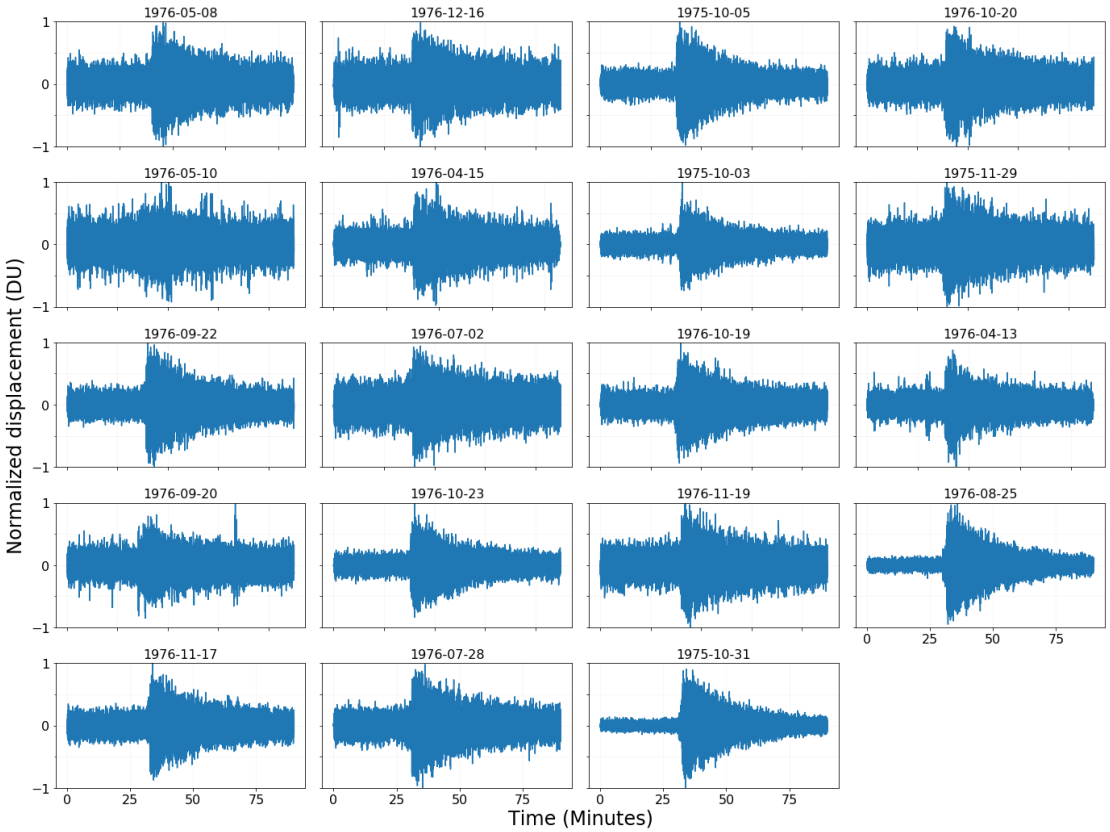


Figure B.3: Deep moonquake waveforms used for PCA decomposition, recorded at station S12, channel MHN, in the flat operation mode.

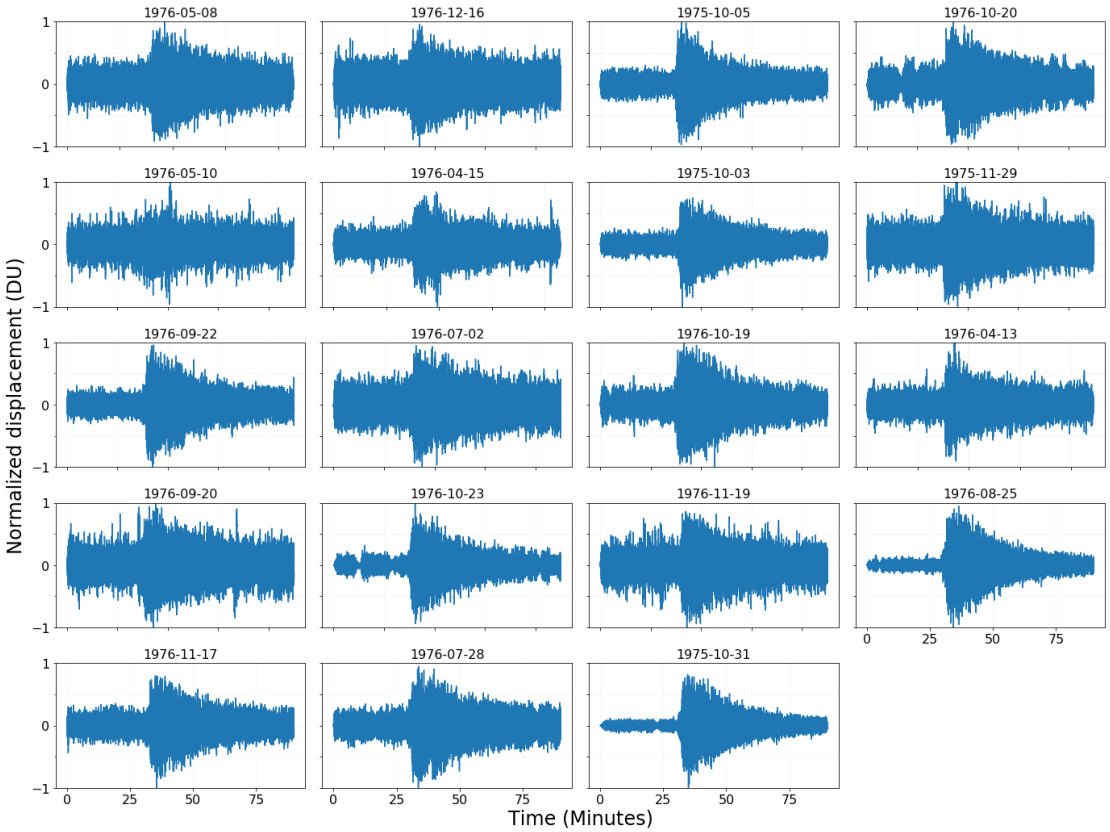


Figure B.4: Deep moonquake waveforms used for PCA decomposition, recorded at station S12, channel MHE, in the flat operation mode.

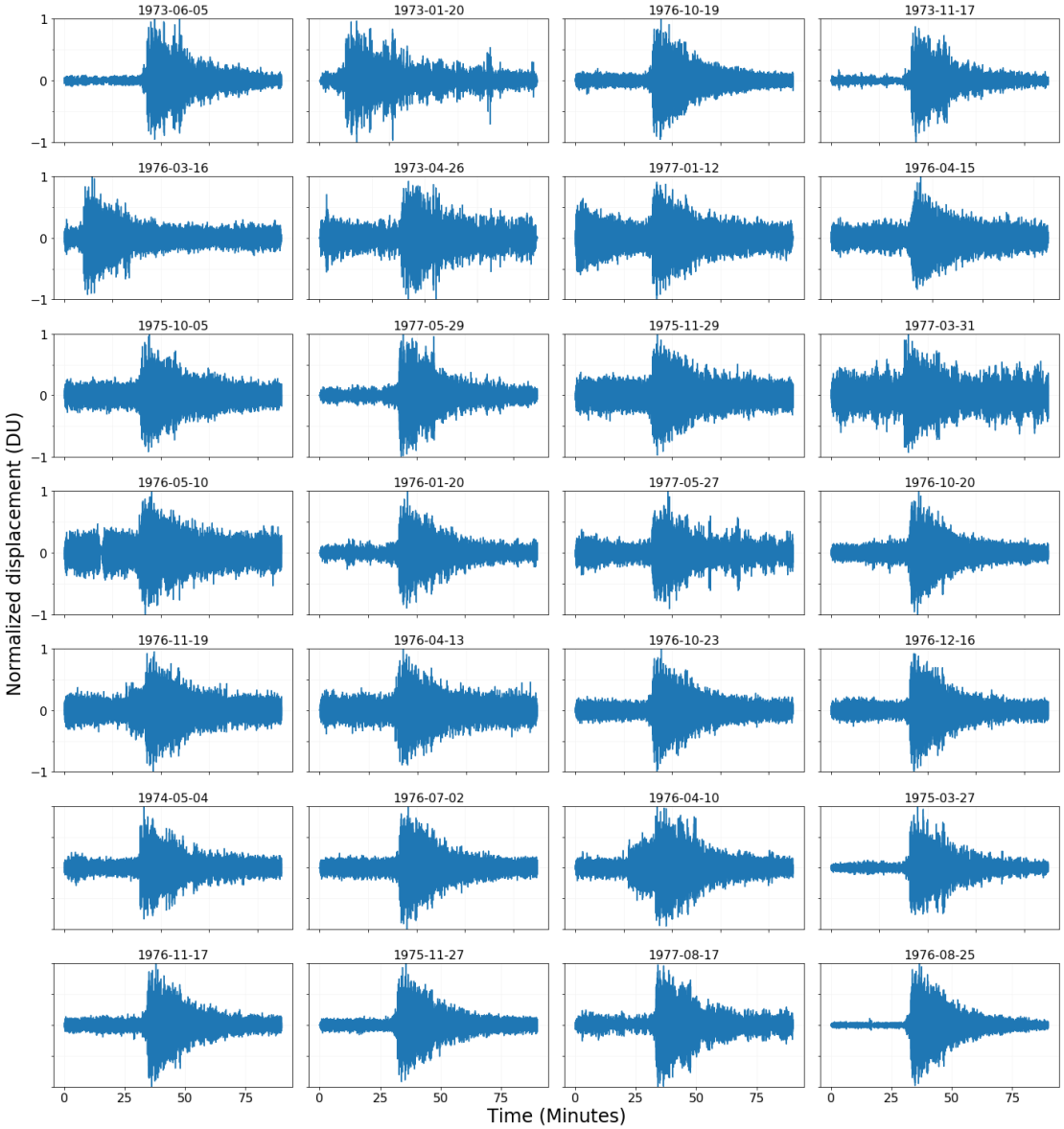


Figure B.5: Deep moonquake waveforms used for PCA decomposition, recorded at station S16, channel MHN, in the peaked operation mode.

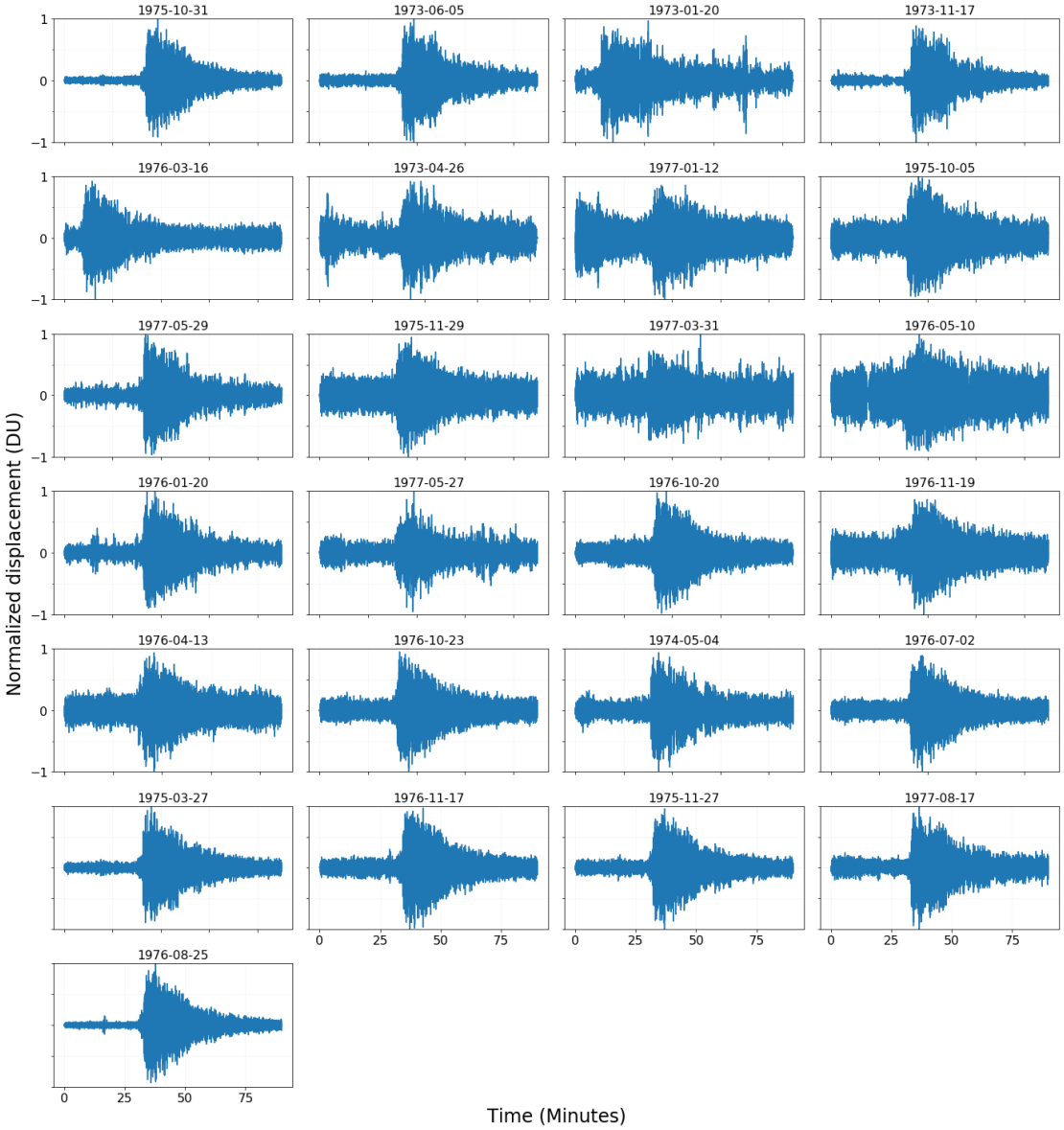


Figure B.6: Deep moonquake waveforms used for PCA decomposition, recorded at station S16, channel MHE, in the peaked operation mode.

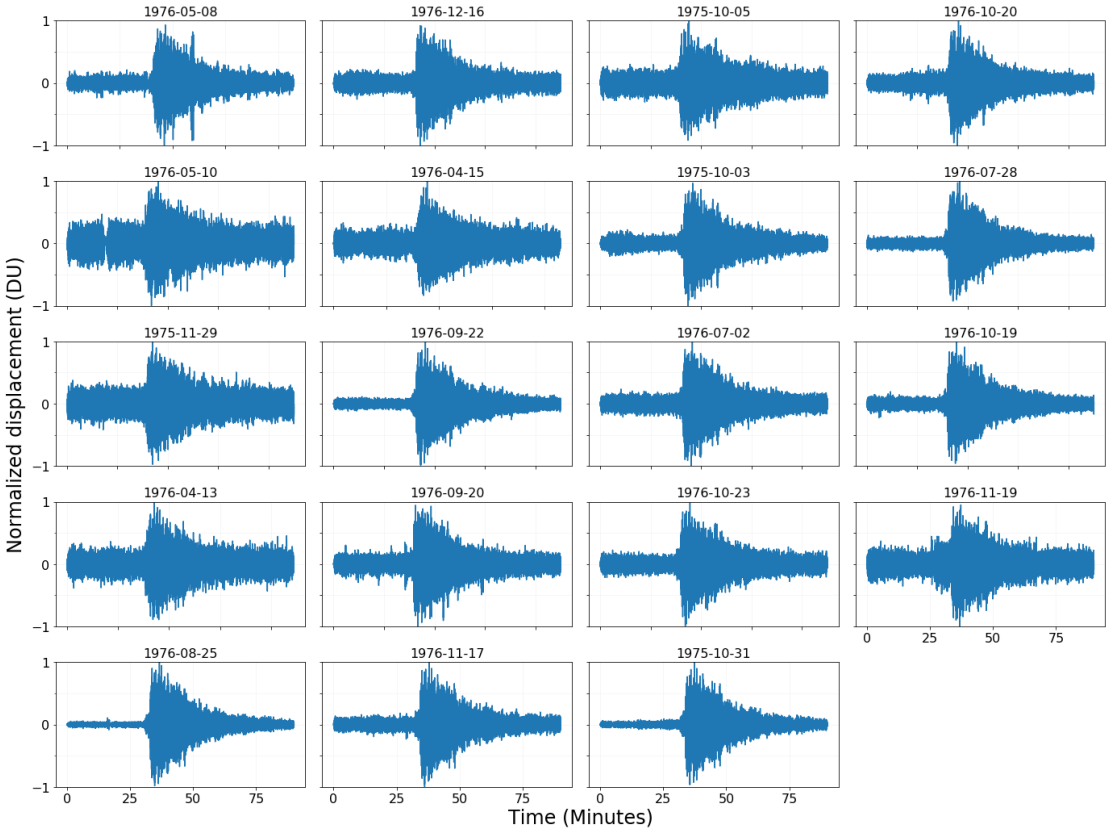


Figure B.7: Deep moonquake waveforms used for PCA decomposition, recorded at station S16, channel MHN, in the flat operation mode.

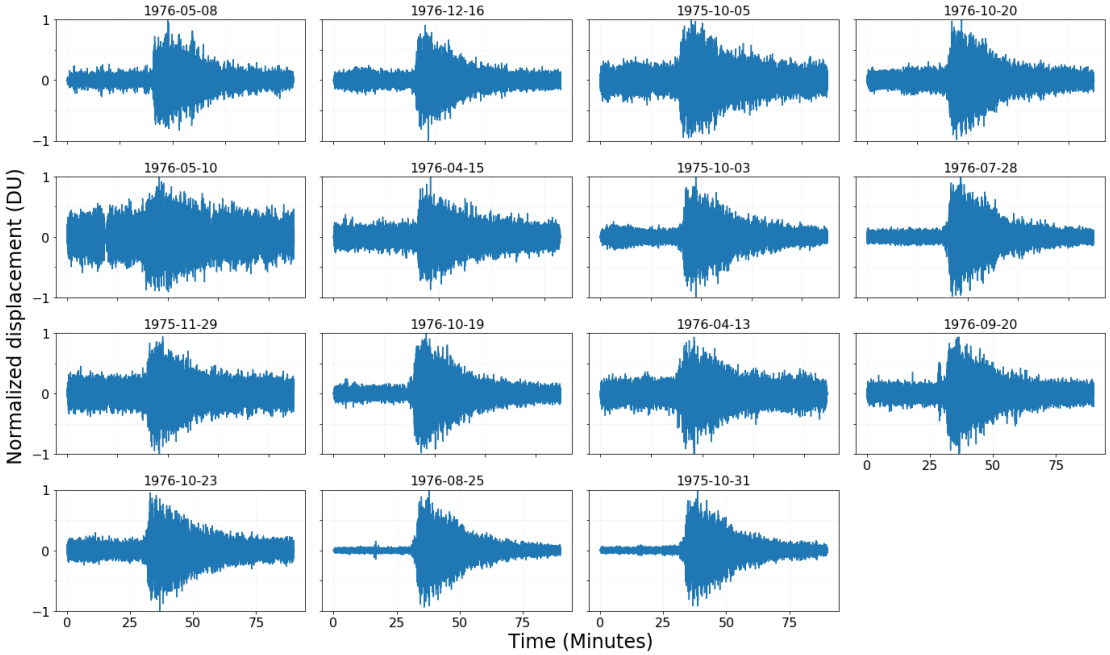


Figure B.8: Deep moonquake waveforms used for PCA decomposition, recorded at station S16, channel MHE, in the flat operation mode.

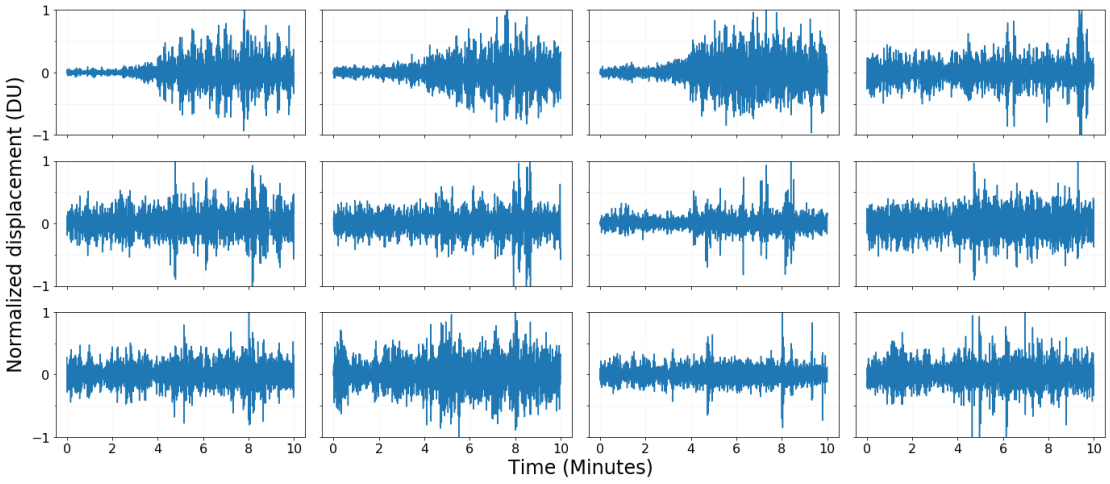


Figure B.9: Principal components derived from the S12 MHE data in the peaked operational mode of the instrument.

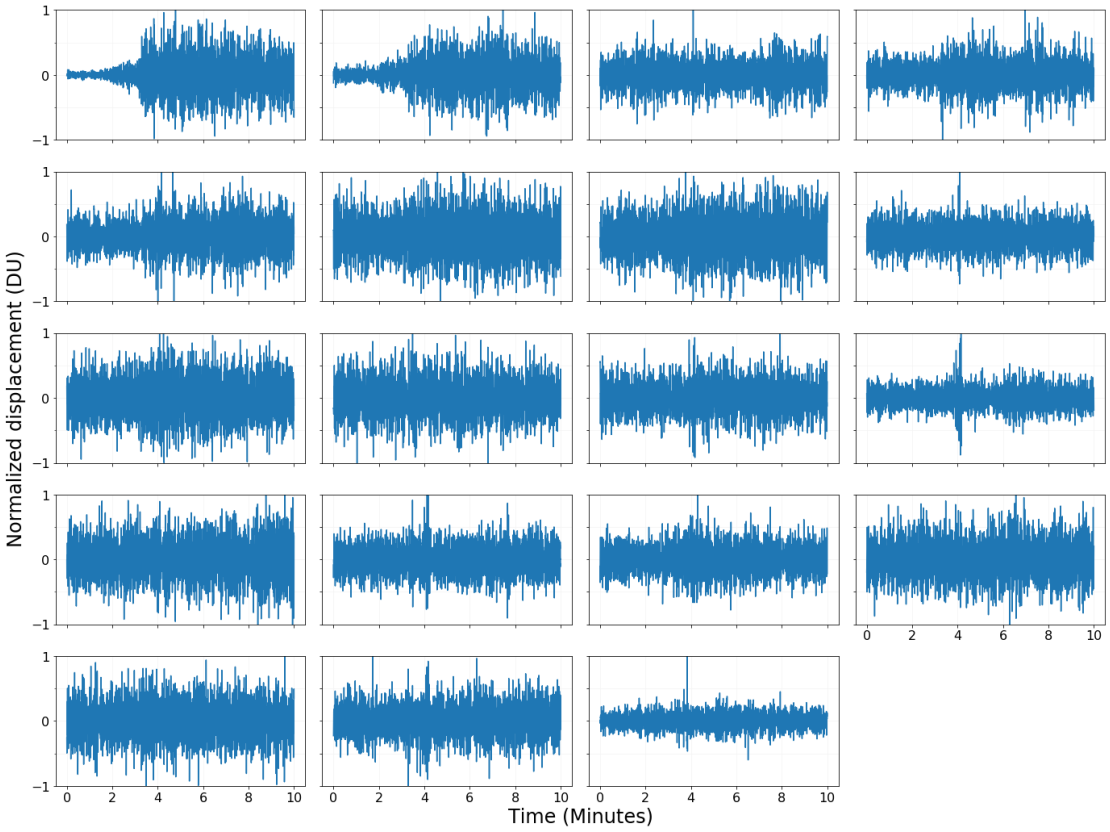


Figure B.10: Principal components derived from the S12 MHN data in the flat operational mode of the instrument.

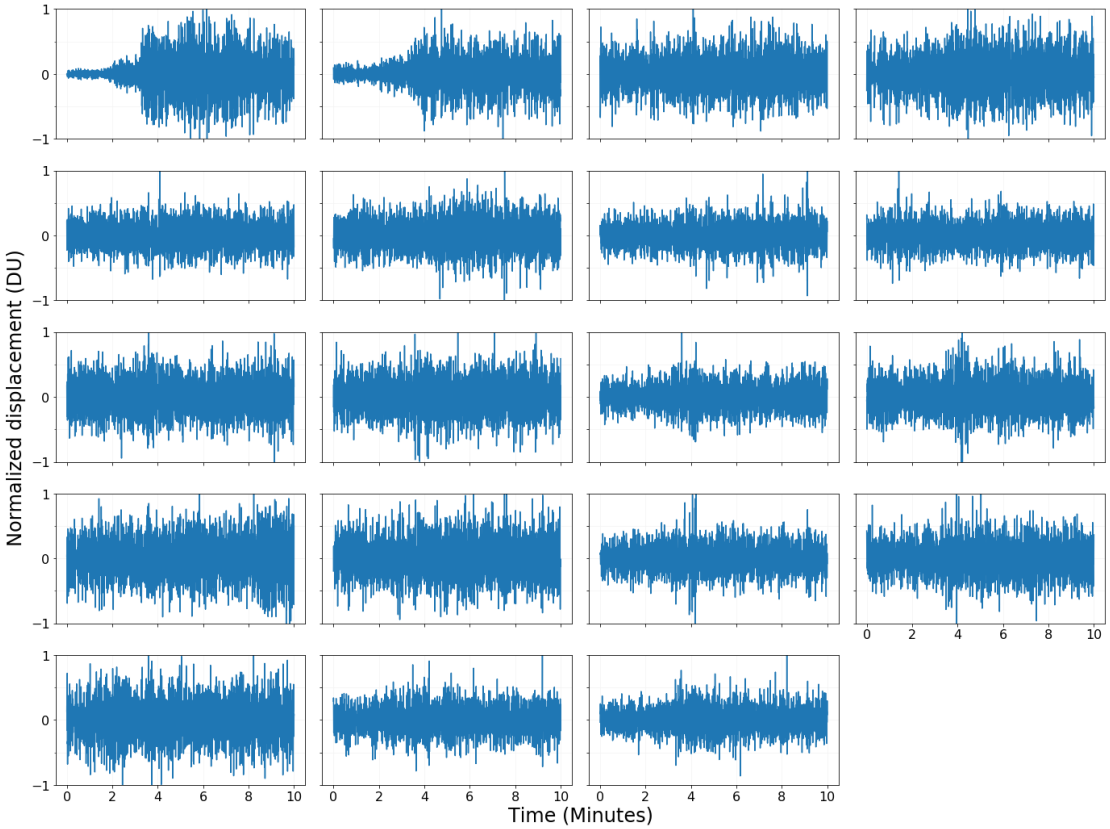


Figure B.11: Principal components derived from the S12 MHE data in the flat operational mode of the instrument.

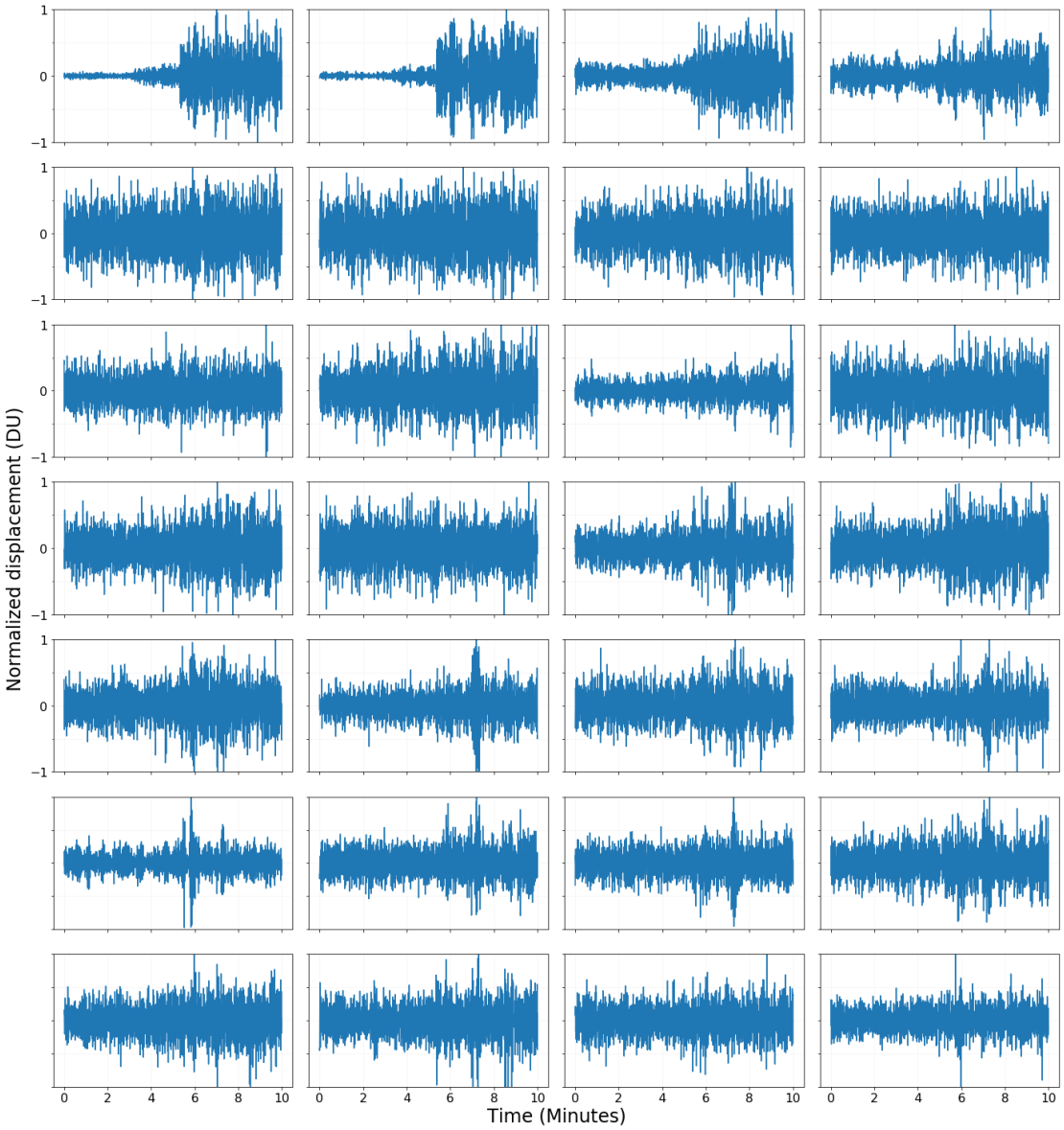


Figure B.12: Principal components derived from the S16 MHN data in the peaked operational mode of the instrument.

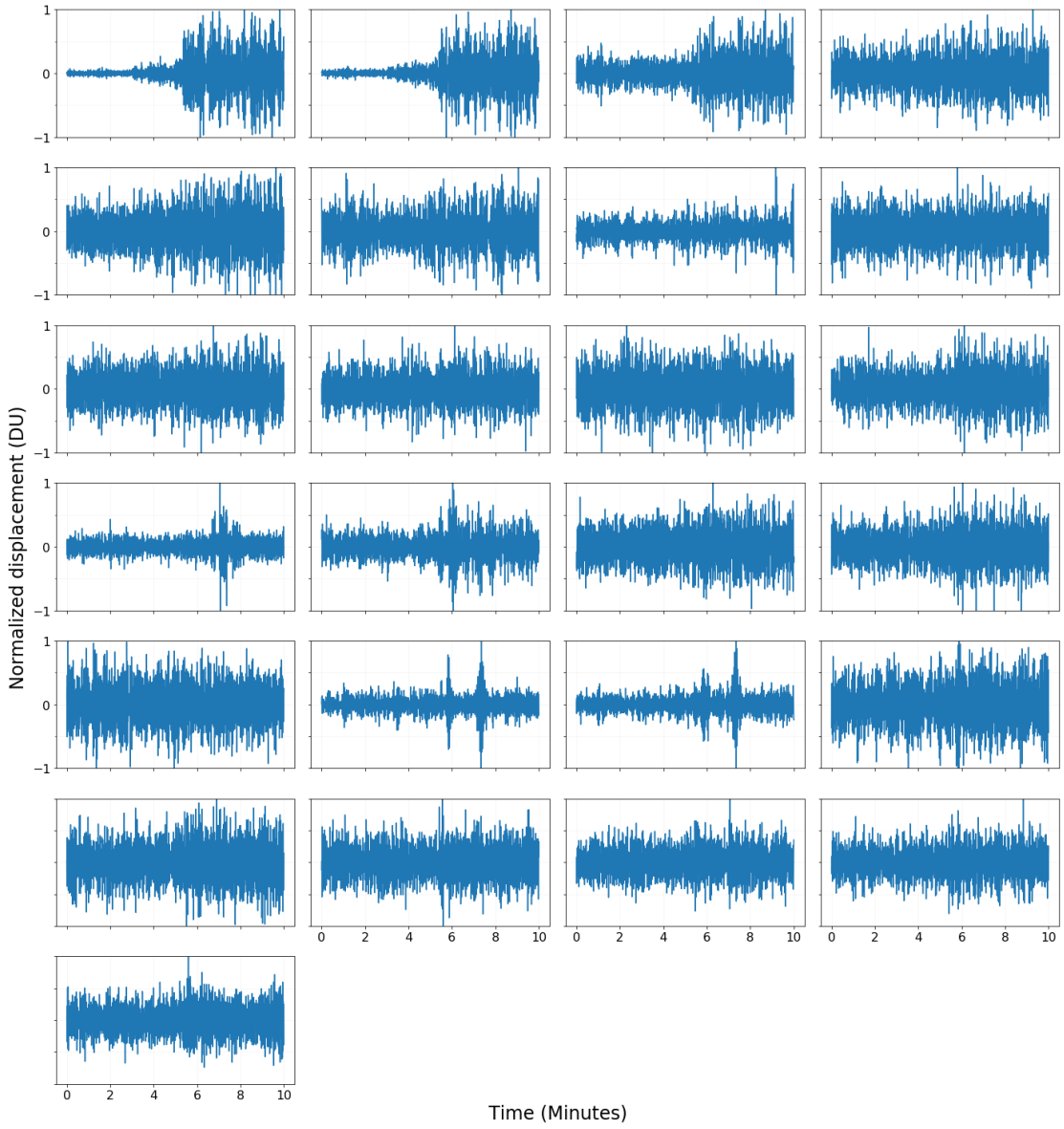


Figure B.13: Principal components derived from the S16 MHE data in the peaked operational mode of the instrument.

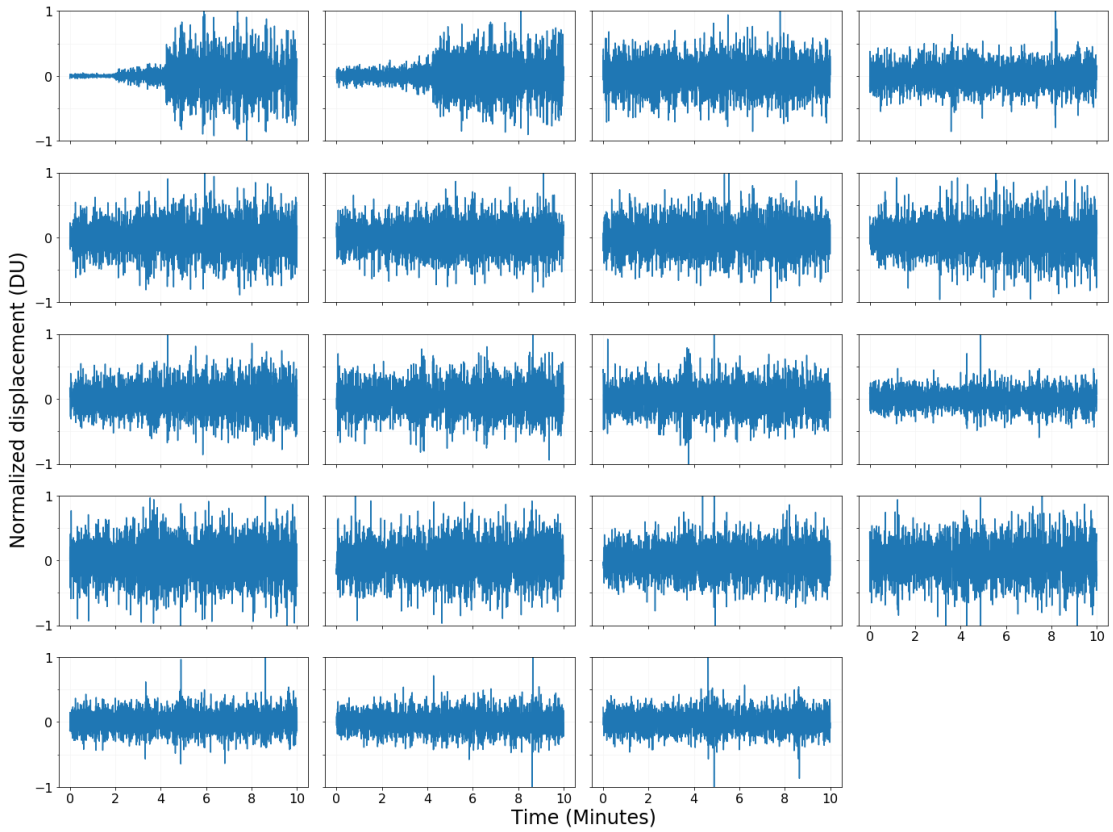


Figure B.14: Principal components derived from the S16 MHN data in the flat operational mode of the instrument.

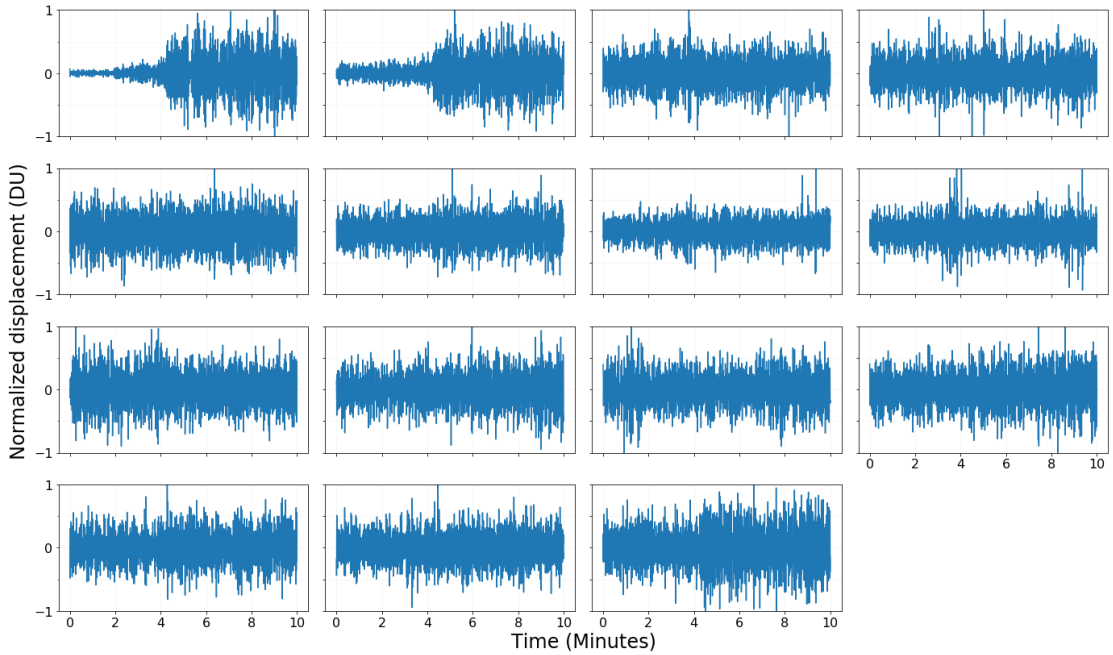


Figure B.15: Principal components derived from the S16 MHE data in the flat operational mode of the instrument.

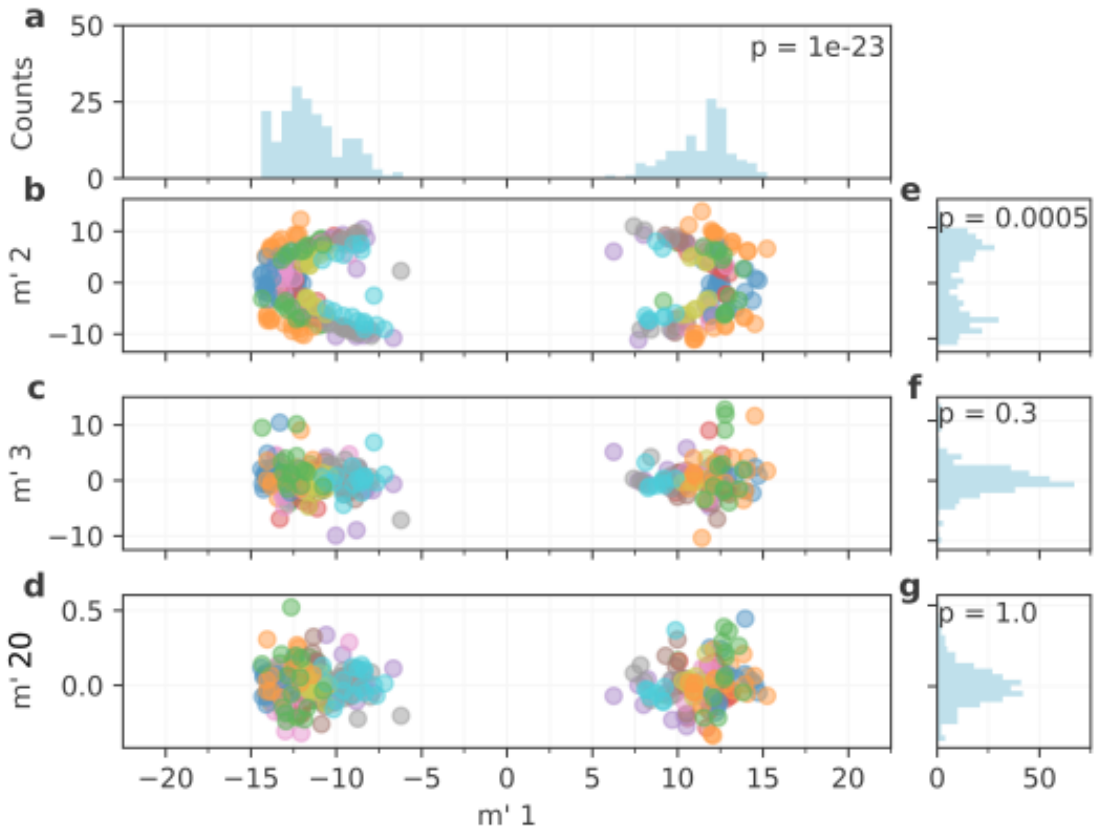


Figure B.16: Unbiased coefficients of the principal components, from the S12 MHE data in the peaked operational mode. In panels b-d, the coefficient for the first principal component m'_{1k} is plotted on the x-axis. The coefficients of the second (m'_{2k}), third (m'_{2k}) and last (m'_{20k}) principal components are plotted on the y axis of panels b,c and d, respectively. Each event is plotted in a different colour. Panels a, e, f, and g summarise the distribution of coefficients for each of the principal components. The text in the top of panels a, e, f, and g is the probability (p-value) that each distribution is the same as the distribution of the coefficients derived from noise. Only the first two components differ from noise.

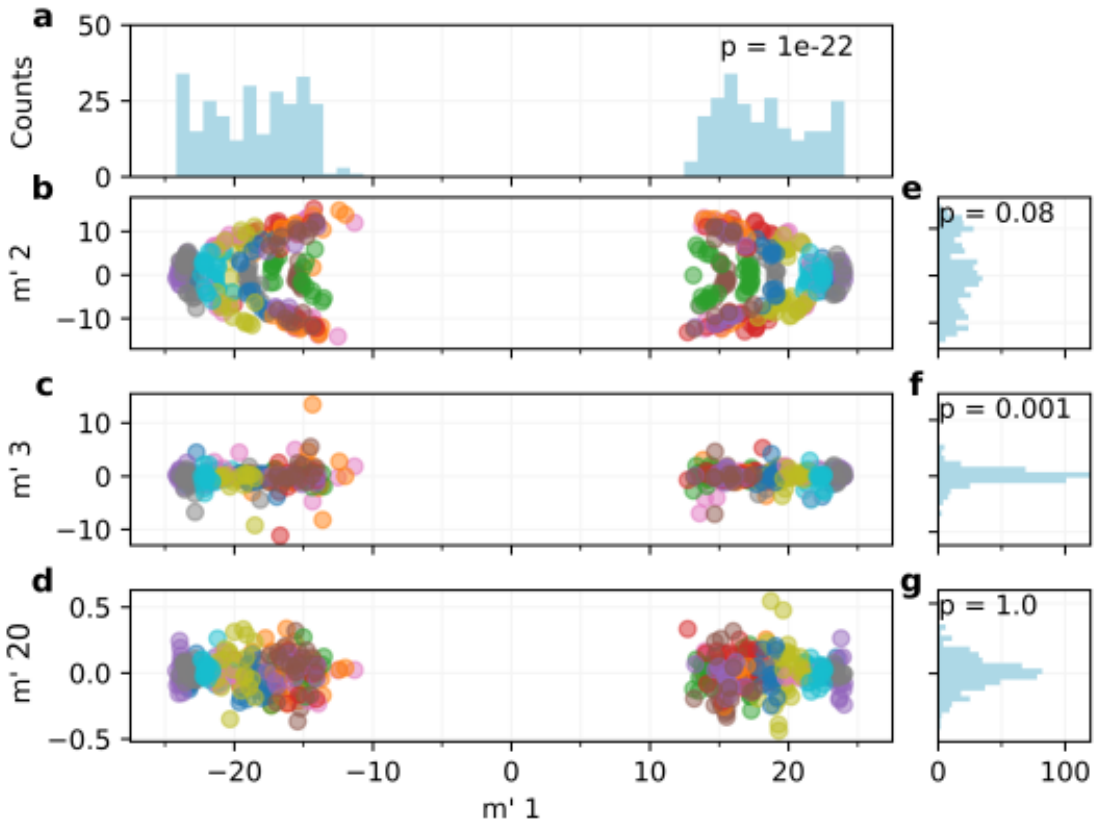


Figure B.17: Same as Figure B.16 from the S12 MHN data in the flat operational mode.

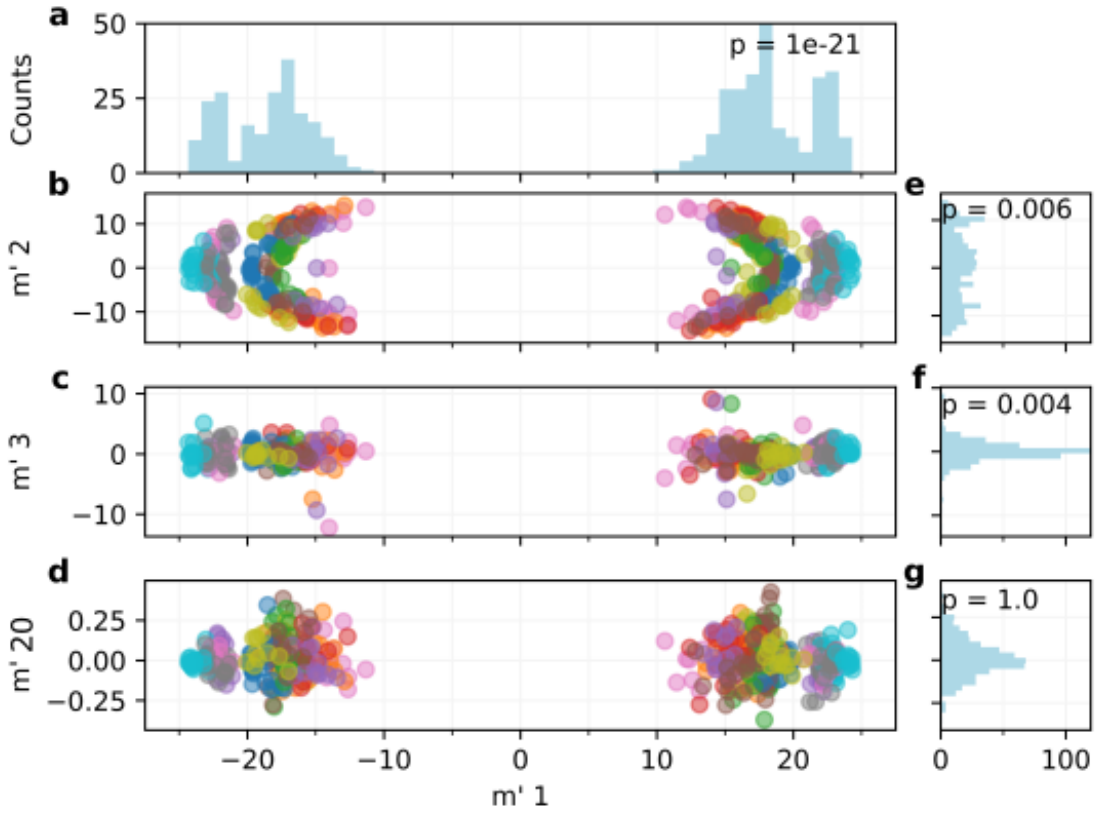


Figure B.18: Same as Figure B.16 from the S12 MHE data in the flat operational mode.

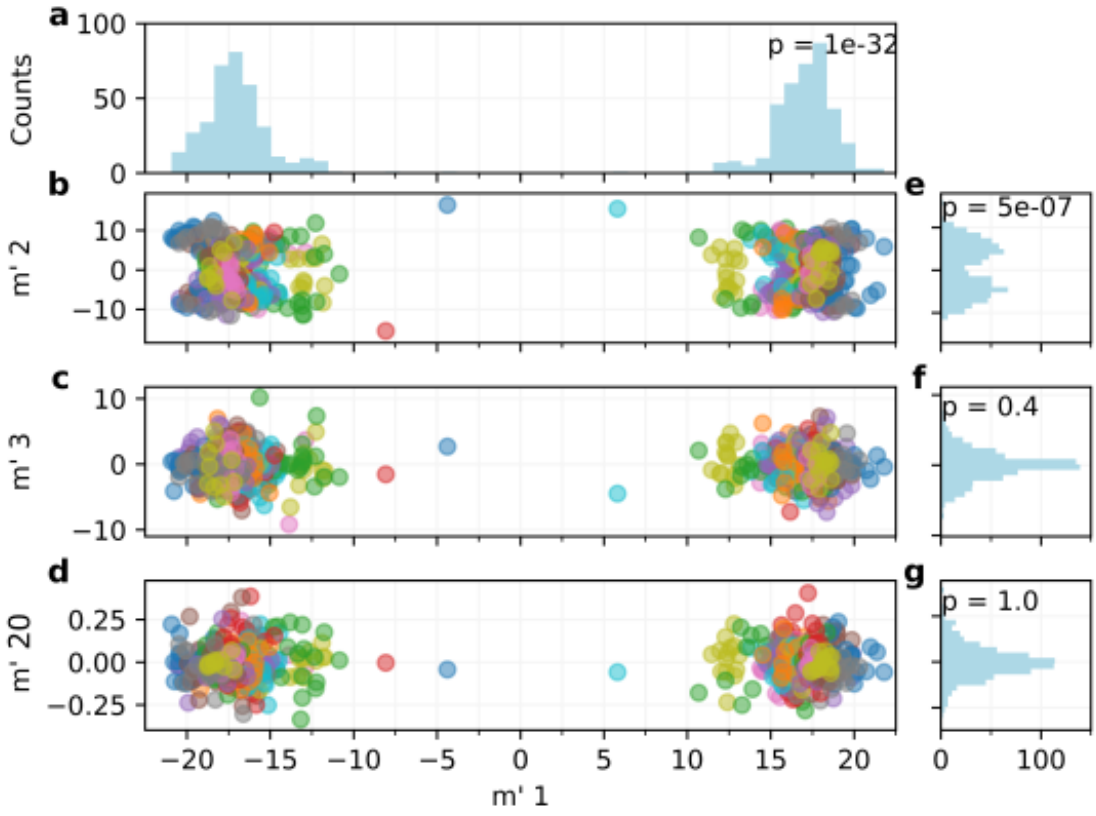


Figure B.19: Same as Figure B.16 from the S16 MHN data in the peaked operational mode.

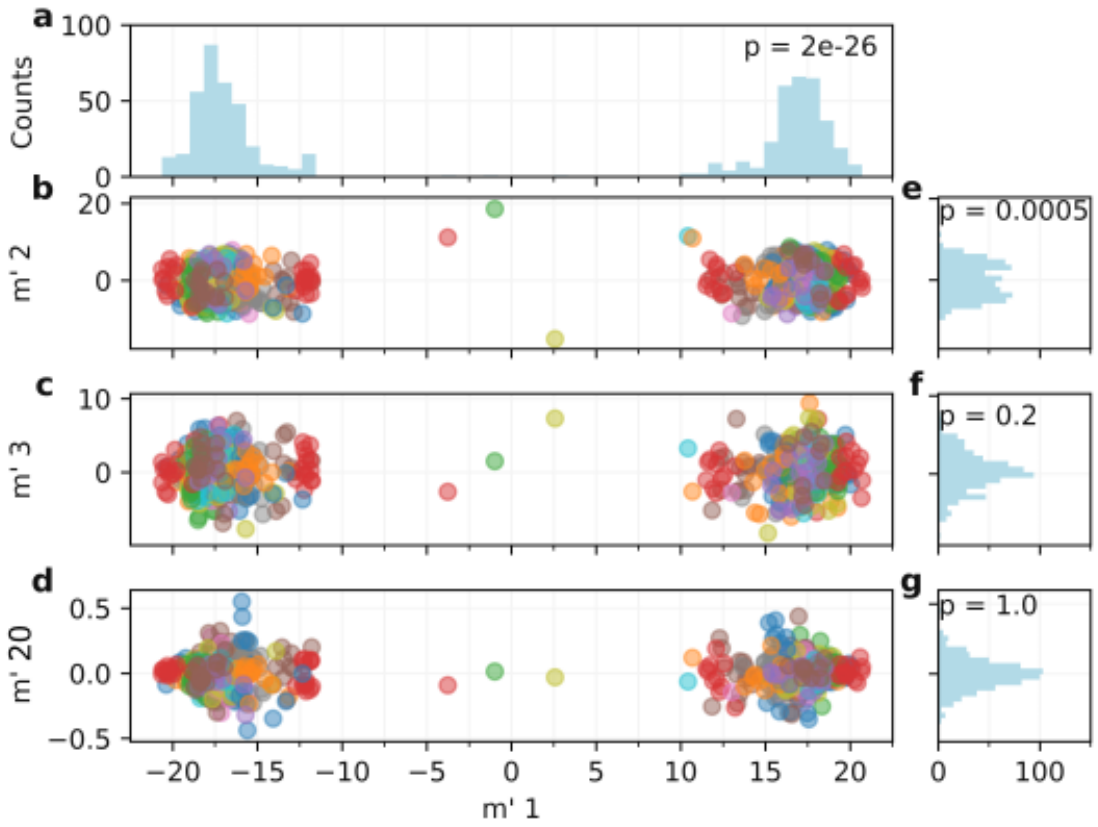


Figure B.20: Same as Figure B.16 from the S16 MHE data in the peaked operational mode.

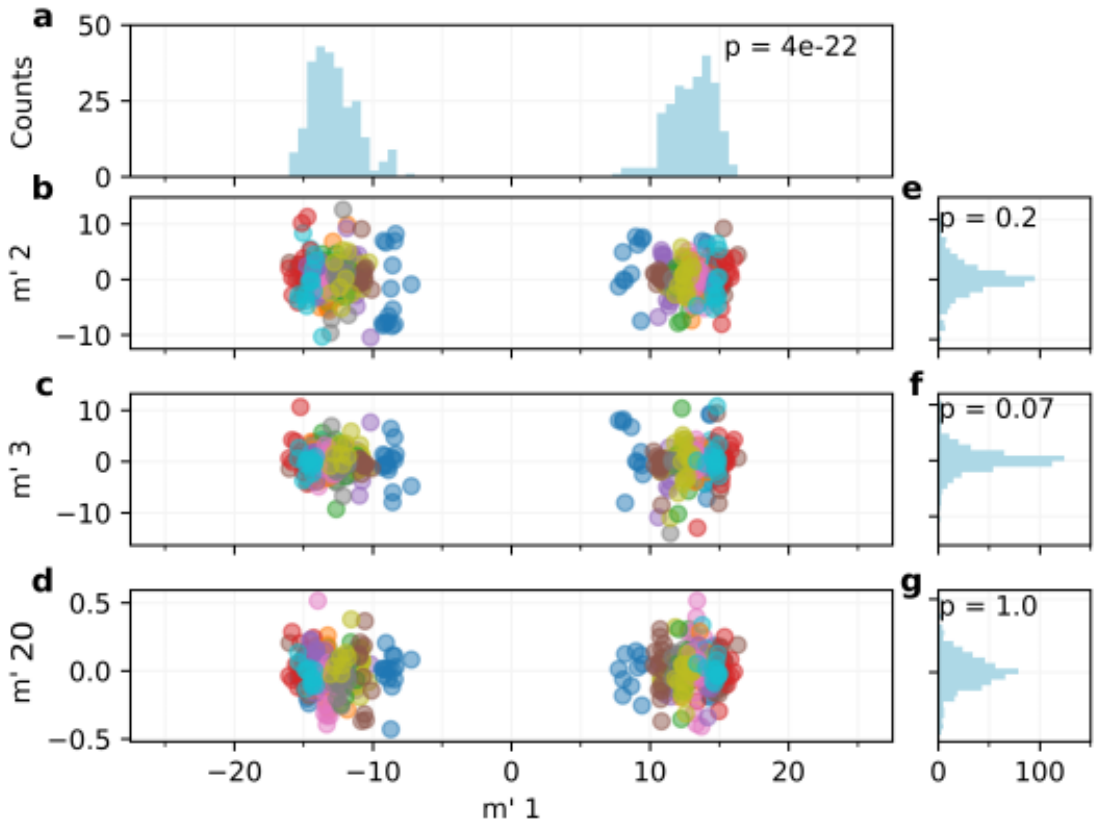


Figure B.21: Same as Figure B.16 from the S16 MHN data in the flat operational mode.

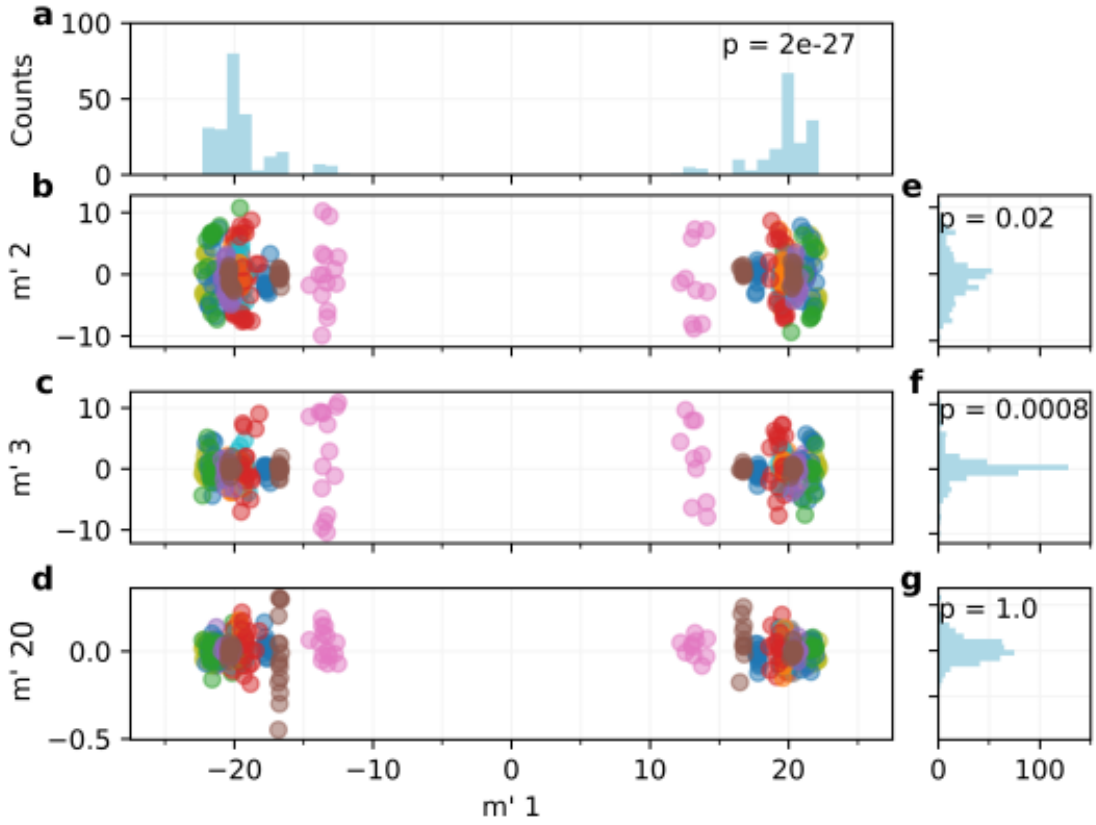


Figure B.22: Same as Figure B.16 from the S16 MHE data in the flat operational mode.

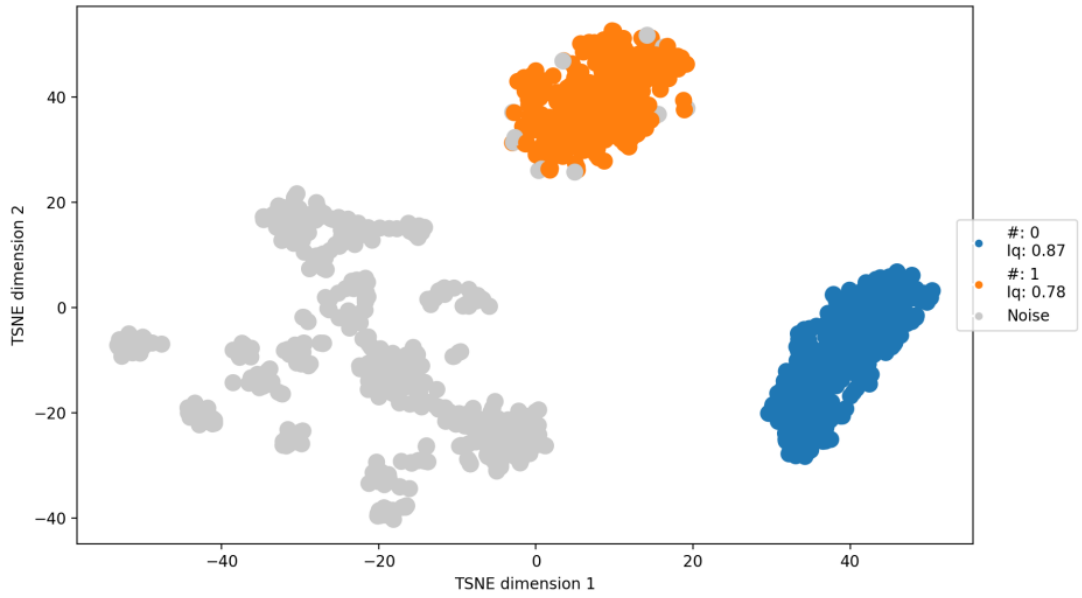


Figure B.23: Clustering results of bootstrapped **G**, obtained for S12 MHE in peaked operational mode. One point is plotted for each bootstrapped estimate of a principal component, but only the first four principal components are plotted. The location of each point is determined by the t-sne algorithm, preserving the similarity of components from the higher dimensional space (Maaten and Hinton, 2008; Gaddes et al., 2019). The colour of each point is determined by the HBDSCAN clustering algorithm (McInnes et al., 2017; Gaddes et al., 2019). Grey points represent component estimates that are not assigned to a cluster.

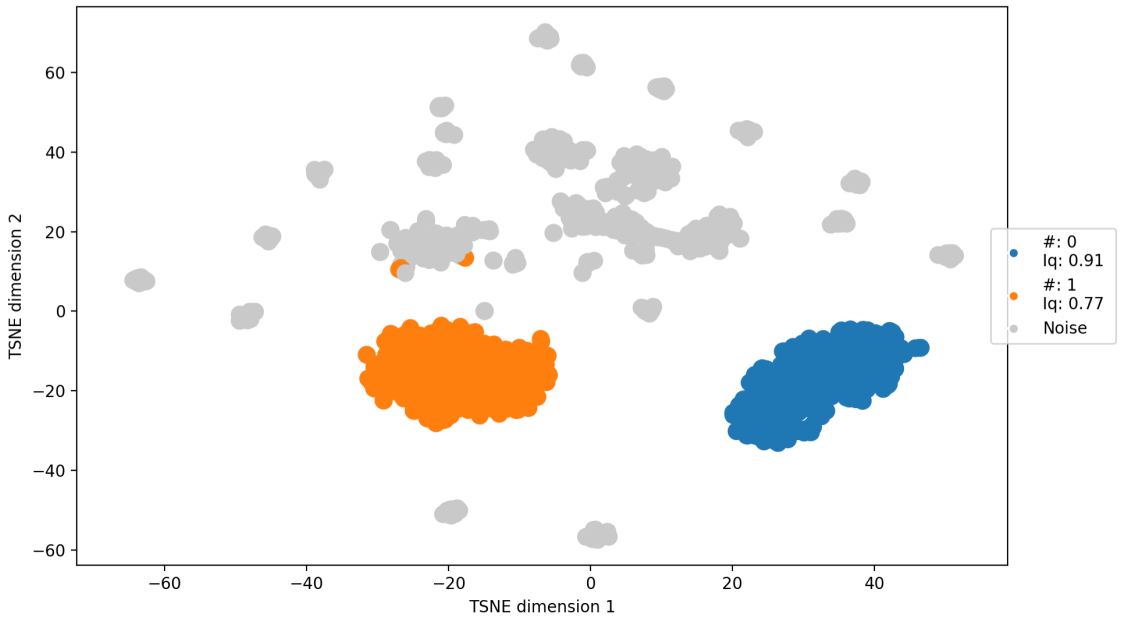


Figure B.24: Same as Figure B.23 obtained for S12 MHN in flat operational mode.

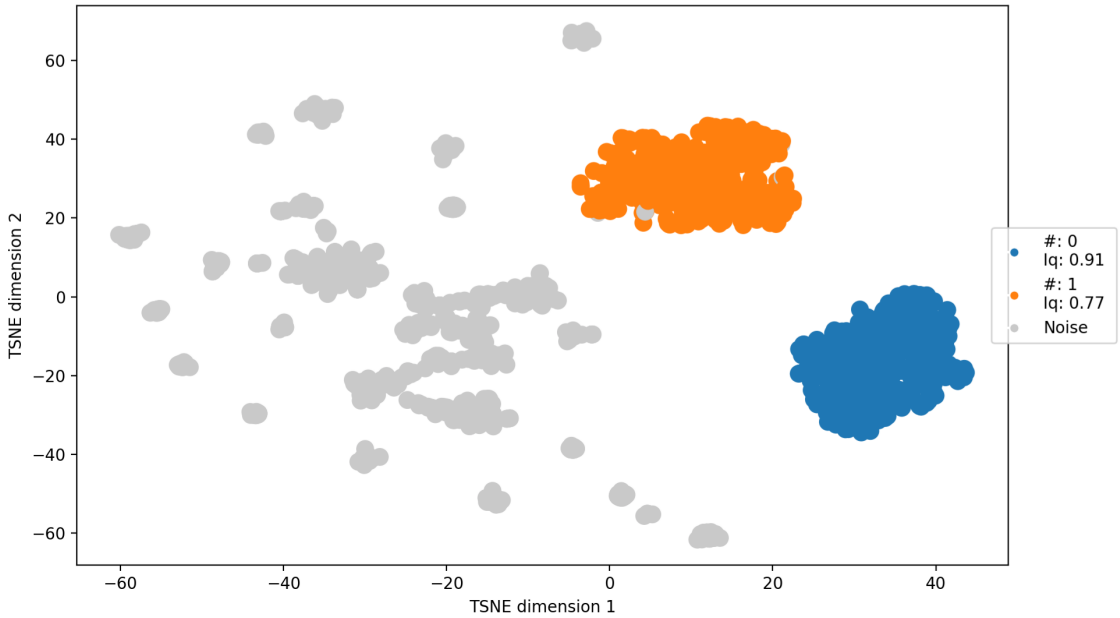


Figure B.25: Same as Figure B.23 obtained for S12 MHE in flat operational mode.

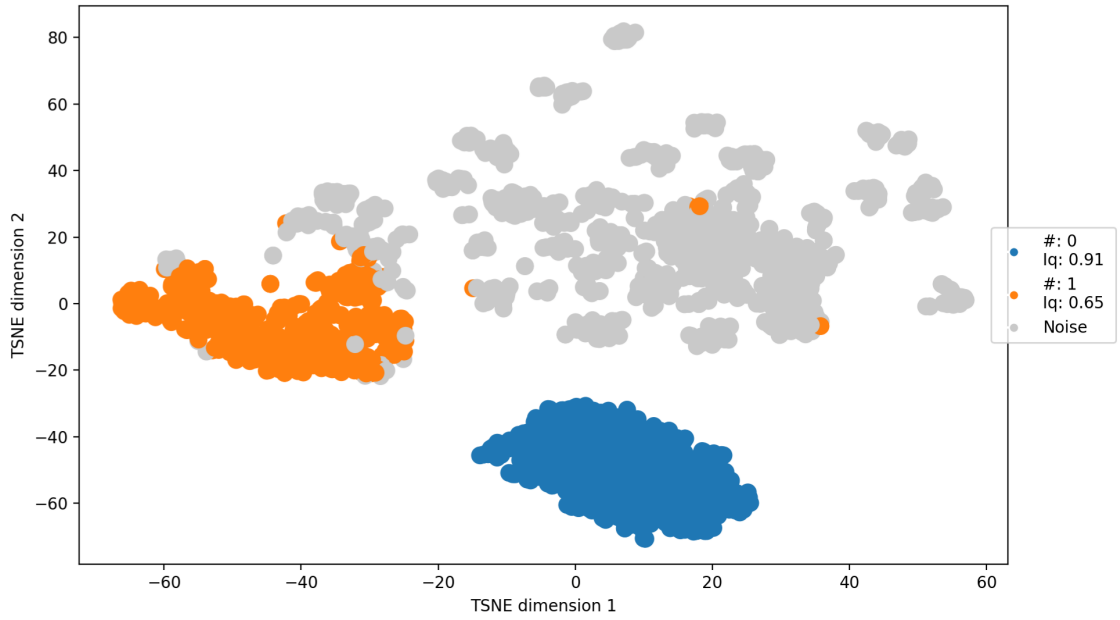


Figure B.26: Same as Figure B.23 obtained for S16 MHN in peaked operational mode.

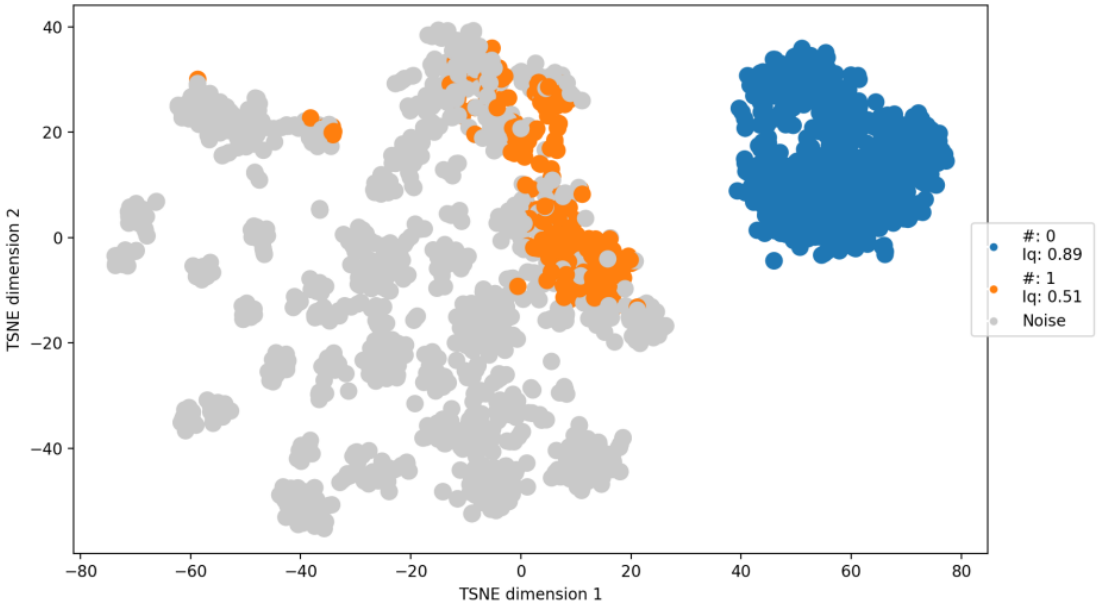


Figure B.27: Same as Figure B.23 obtained for S16 MHE in peaked operational mode.

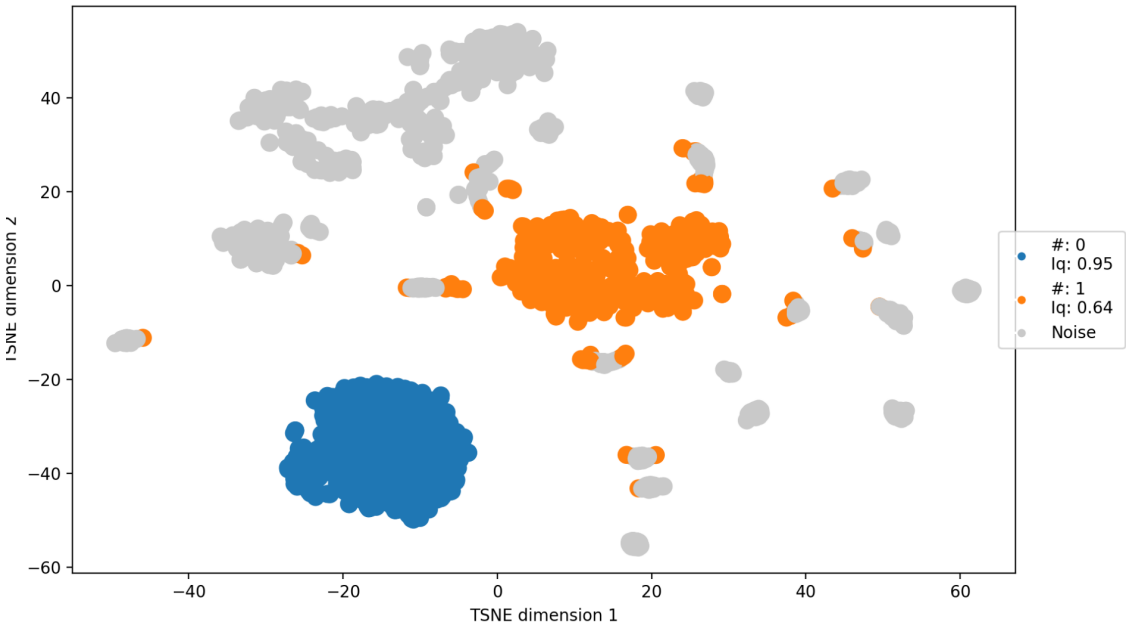


Figure B.28: Same as Figure B.23 obtained for S16 MHN in flat operational mode.

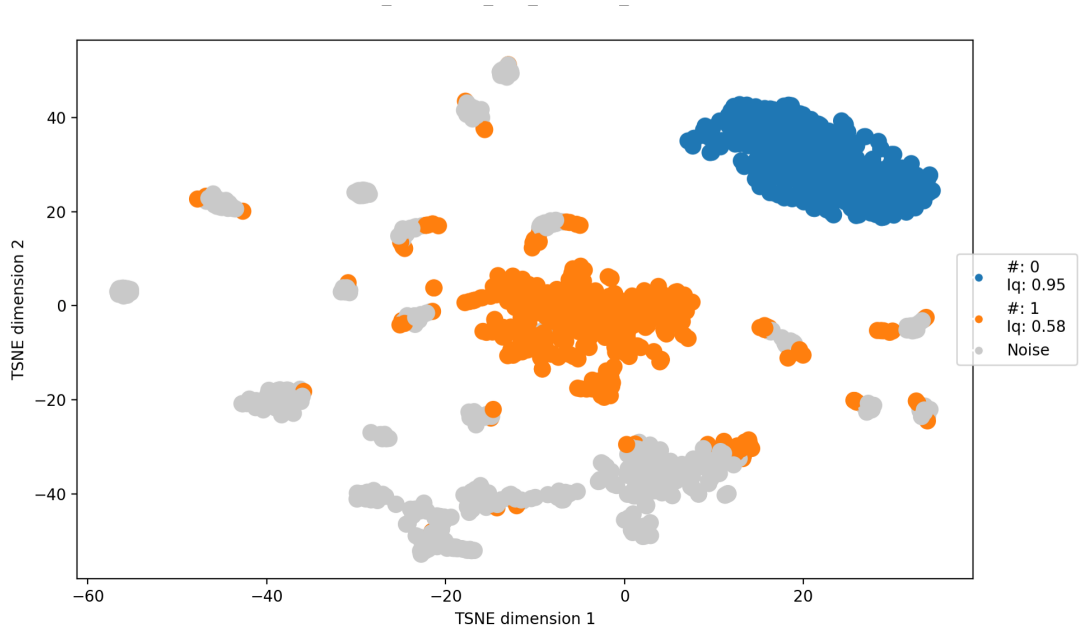


Figure B.29: Same as Figure B.23 obtained for S16 MHE in flat operational mode.

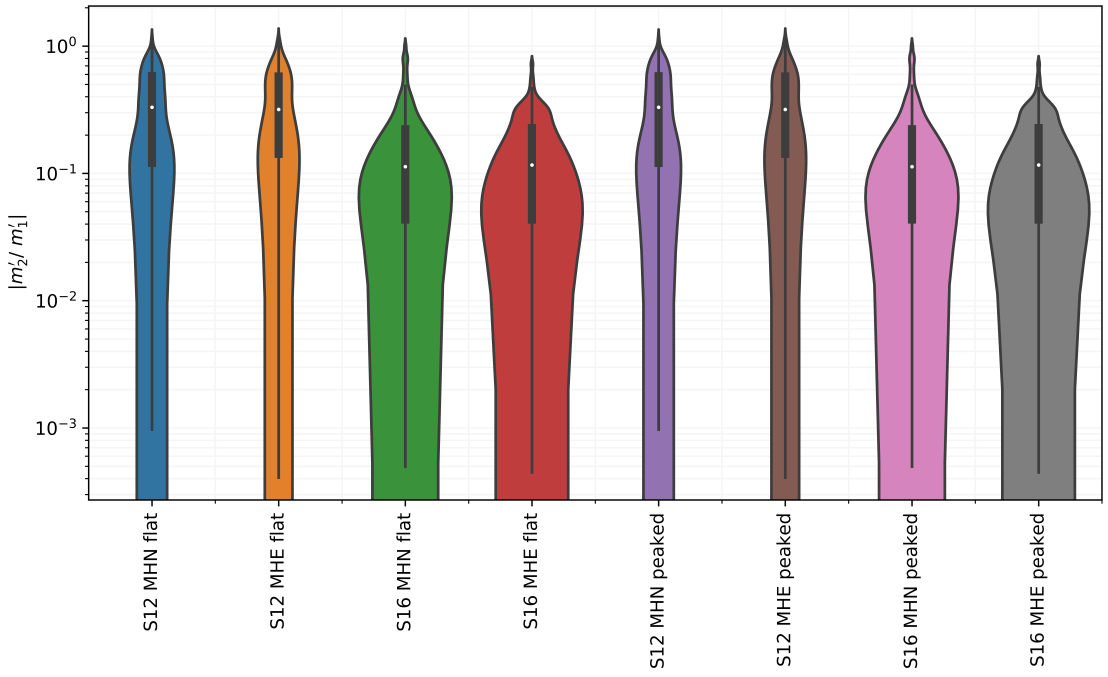


Figure B.30: Slip coefficient ratio $|m'_{2k}/m_{1k}|'$ for each station and channel, now plotted with a log axis. The white dot marks the median bootstrapped ratio at each station, the black bar delimits the inter-quartile range, and the thin black line delimits 1.5 × the inter-quartile range. The coloured areas illustrate the probability density of the ratio at each station.

C

Supporting information for "Using principal component analysis to improve relative arrival times of deep moonquakes"

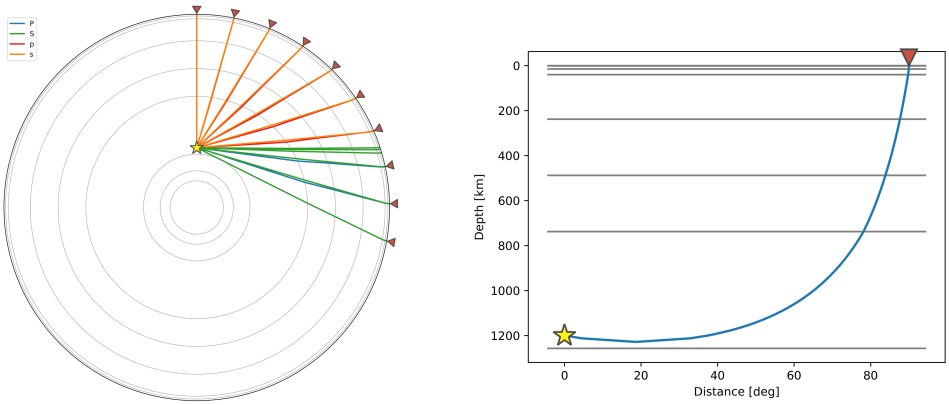


Figure C.1: Left: Ray paths of p,s,P and S phases produced by a deep moonquake with depth of 1200 km and recorded at stations with epicentral distances up to 100°. The incidence angles at the stations are less than 2°. The ray paths were calculated using the lunar interior model of Weber et al. (2011) and TauP (Crotwell et al., 1999).. **Left:** Ray paths of a P phase produced by a deep moonquake with depth of 1200 km and recorded at stations with epicentral distance of 80° plotted in Cartesian co-ordinates. The incidence angle at the station is 80°.

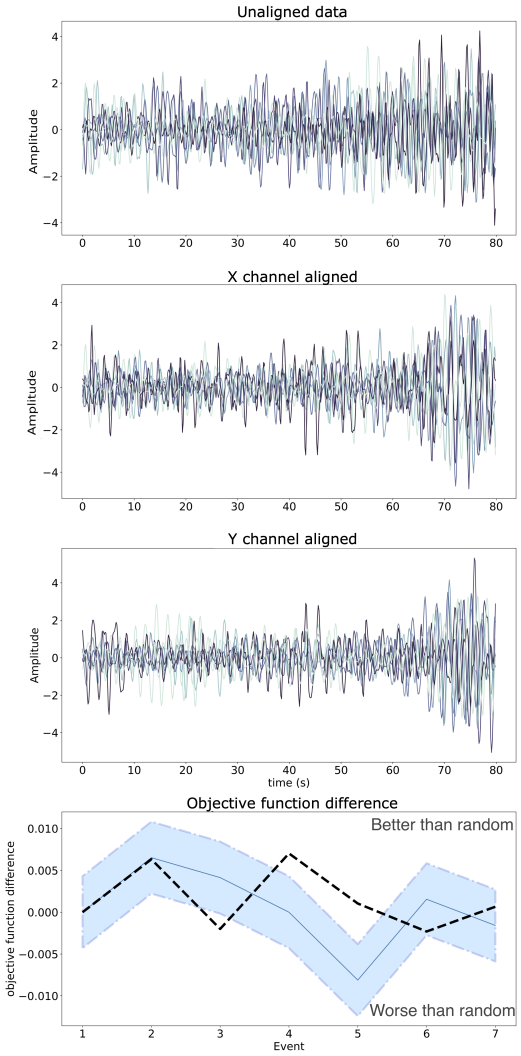


Figure C.2: Top: 8 unaligned deep moonquake stacks recorded on the x-channel. Each event is coloured in a different shade of blue. **Second:** Waveform recorded on the x-channel aligned relative to the A022 stack. **Third:** Waveform recorded on the y-channel aligned using the time-shifts recovered from the x-channel. **Bottom:** Y-channel objective function changes. Blue line shows the difference between the minimum objective function and the average value of the objective function when each event is randomly shifted by between 0 - 1.5 seconds. The blue line is calculated from the average 1000 random shifts for each event. The light blue region is the standard deviation (70th percentile) of the objective function difference for each event. The grey dashed line is the misfit difference between randomly aligned waveforms, and each event is further randomly aligned and is used as a baseline.

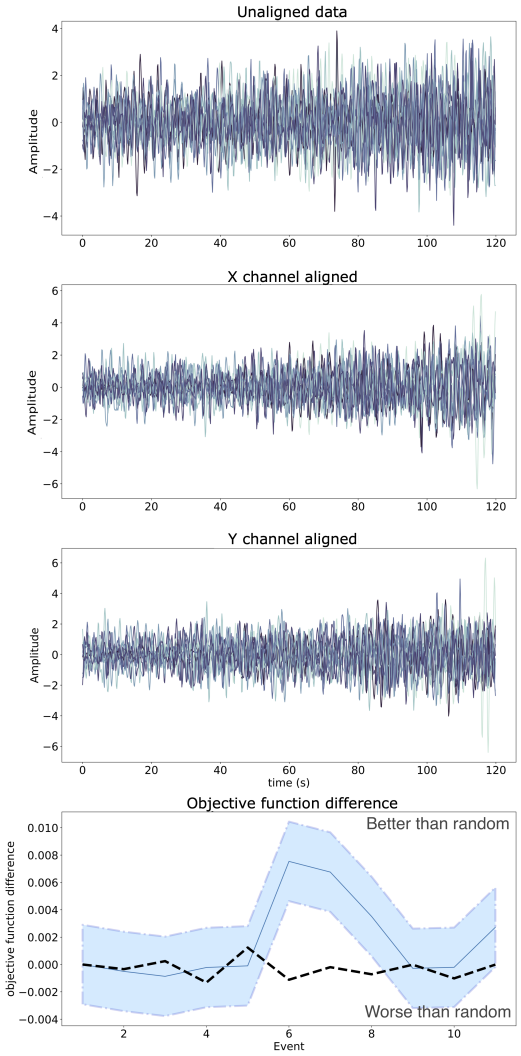


Figure C.3: Top: 11 unaligned deep moonquake stacks recorded on the x-channel. Each event is coloured in a different shade of blue. **Second:** Waveform recorded on the x-channel aligned relative to the A022 stack. **Third:** Waveform recorded on the y-channel aligned using the time-shifts recovered from the x-channel. **Bottom:** Y-channel objective function changes. Blue line shows the difference between the minimum objective function and the average value of the objective function when each event is randomly shifted by between 0 - 10 seconds. The blue line is calculated from the average 1000 random shifts for each event. The light blue region is the standard deviation (70th percentile) of the objective function difference for each event. The grey dashed line is the misfit difference between randomly aligned waveforms, and each event is further randomly aligned and is used as a baseline.

References

Abercrombie, R. E. (2014). "Stress drops of repeating earthquakes on the San Andreas fault at Parkfield". In: *Geophysical Research Letters* 41.24, pp. 8784–8791.

Abercrombie, R. E., X. Chen, and J. Zhang (2020). "Repeating earthquakes with remarkably repeatable ruptures on the San Andreas Fault at Parkfield". In: *Geophysical Research Letters* 47.23, e2020GL089820.

Allmann, B. P. and P. M. Shearer (2007). "Spatial and temporal stress drop variations in small earthquakes near Parkfield, California". In: *Journal of Geophysical Research: Solid Earth* 112.B4.

Anooshehpoor, A. and J. N. Brune (2001). "Quasi-static slip-rate shielding by locked and creeping zones as an explanation for small repeating earthquakes at Parkfield". In: *Bulletin of the Seismological Society of America* 91.2, pp. 401–403.

Araki, H. (2001). "Focal processes of deep moonquakes". In: *Journal of the Geodetic Society of Japan* 47.1, pp. 508–513.

Barbot, S. (2019). "Slow-slip, slow earthquakes, period-two cycles, full and partial ruptures, and deterministic chaos in a single asperity fault". In: *Tectonophysics* 768, p. 228171.

Beeler, N. and D. Lockner (2003). "Why earthquakes correlate weakly with the solid Earth tides: Effects of periodic stress on the rate and probability of earthquake occurrence". In: *Journal of Geophysical Research: Solid Earth* 108.B8.

Beeler, N., D. Lockner, and S. Hickman (2001). "A simple stick-slip and creep-slip model for repeating earthquakes and its implication for microearthquakes at Parkfield". In: *Bulletin of the Seismological Society of America* 91.6, pp. 1797–1804.

Bishop, C. M. and N. M. Nasrabadi (2006). *Pattern recognition and machine learning*. Vol. 4. 4. Springer.

Blanchette-Guertin, J.-F., C. Johnson, and J. Lawrence (2012). "Investigation of scattering in lunar seismic coda". In: *Journal of Geophysical Research: Planets* 117.E6.

Brantut, N., J. Sulem, and A. Schubnel (2011). "Effect of dehydration reactions on earthquake nucleation: Stable sliding, slow transients, and unstable slip". In: *Journal of Geophysical Research: Solid Earth* 116.B5.

Bulow, R., C. Johnson, and P. Shearer (2005). "New events discovered in the Apollo lunar seismic data". In: *Journal of Geophysical Research: Planets* 110.E10.

Bulow, R. et al. (2007). "Temporal and spatial properties of some deep moonquake clusters". In: *Journal of Geophysical Research: Planets* 112.E9.

Bürgmann, R. et al. (2000). "Earthquake potential along the northern Hayward fault, California". In: *Science* 289.5482, pp. 1178–1182.

Burnley, P. C., H. W. Green, and D. J. Prior (1991). "Faulting associated with the olivine to spinel transformation in Mg_2GeO_4 and its implications for deep-focus earthquakes". In: *Journal of Geophysical Research: Solid Earth* 96.B1, pp. 425–443.

Cattania, C. (2019). "Complex earthquake sequences on simple faults". In: *Geophysical Research Letters* 46.17-18, pp. 10384–10393.

Cattania, C. and P. Segall (2019). "Crack models of repeating earthquakes predict observed moment-recurrence scaling". In: *Journal of Geophysical Research: Solid Earth* 124.1, pp. 476–503.

Chalumeau, C. et al. (2021). "Repeating earthquakes at the edge of the afterslip of the 2016 Ecuadorian M_W 7.8 Pedernales earthquake". In: *Journal of Geophysical Research: Solid Earth* 126.5, e2021JB021746.

Chang, Y., L. M. Warren, and G. A. Prieto (2017). "Precise Locations for Intermediate-Depth Earthquakes in the Cauca Cluster, Colombia". In: *Bulletin of the Seismological Society of America* 107.6, pp. 2649–2663.

Che, X. et al. (2021). "Age and composition of young basalts on the Moon, measured from samples returned by Chang'e-5". In: *Science* 374.6569, pp. 887–890.

Chen, K. H., R. M. Nadeau, and R.-J. Rau (2007). "Towards a universal rule on the recurrence interval scaling of repeating earthquakes?" In: *Geophysical Research Letters* 34.16.

Chen, K. H., R.-J. Rau, and J.-C. Hu (2009). "Variability of repeating earthquake behavior along the Longitudinal Valley fault zone of eastern Taiwan". In: *Journal of Geophysical Research: Solid Earth* 114.B5.

Chen, K. H., R. Bürgmann, and R. M. Nadeau (2013). "Do earthquakes talk to each other? Triggering and interaction of repeating sequences at Parkfield". In: *Journal of Geophysical Research: Solid Earth* 118.1, pp. 165–182.

Chen, K. H. et al. (2010). "Postseismic variations in seismic moment and recurrence interval of repeating earthquakes". In: *Earth and Planetary Science Letters* 299.1-2, pp. 118–125.

Chen, T. and N. Lapusta (2009). "Scaling of small repeating earthquakes explained by interaction of seismic and aseismic slip in a rate and state fault model". In: *Journal of Geophysical Research: Solid Earth* 114.B1.

— (2019). "On behaviour and scaling of small repeating earthquakes in rate and state fault models". In: *Geophysical Journal International* 218.3, pp. 2001–2018.

Chen, Y. et al. (2020). "Probing the variation in aseismic slip behavior around an active suture zone: Observations of repeating earthquakes in eastern Taiwan". In: *Journal of Geophysical Research: Solid Earth* 125.5, e2019JB018561.

Cheng, C. H. and M. N. Toksöz (1978). "Tidal stresses in the Moon". In: *Journal of Geophysical Research: Solid Earth* 83.B2, pp. 845–853.

Chiaraluce, L. et al. (2007). "Architecture and mechanics of an active low-angle normal fault: Alto Tiberina fault, northern Apennines, Italy". In: *Journal of Geophysical Research: Solid Earth* 112.B10.

Cochran, E. S. et al. (2018). "Induced earthquake families reveal distinctive evolutionary patterns near disposal wells". In: *Journal of Geophysical Research: Solid Earth* 123.9, pp. 8045–8055.

Crotwell, H. P., T. J. Owens, J. Ritsema, et al. (1999). "The TauP Toolkit: Flexible seismic travel-time and ray-path utilities". In: *Seismological Research Letters* 70, pp. 154–160.

Dainty, A. M. and M. N. Toksöz (1981). "Seismic codas on the Earth and the Moon: A comparison". In: *Physics of the Earth and Planetary Interiors* 26.4, pp. 250–260.

Dainty, A. M. et al. (1974). "Seismic scattering and shallow structure of the Moon in Oceanus Procellarum". In: *The Moon* 9.1, pp. 11–29.

Danesi, S., S. Bannister, and A. Morelli (2007). "Repeating earthquakes from rupture of an asperity under an Antarctic outlet glacier". In: *Earth and Planetary Science Letters* 253.1-2, pp. 151–158.

Davies, J. H. (1999). "The role of hydraulic fractures and intermediate depth earthquakes in subduction zone magmatism". In: *Nature* 398.6723, pp. 142–145.

Dieterich, J. H. (1979). "Modeling of rock friction: 1. Experimental results and constitutive equations". In: *Journal of Geophysical Research: Solid Earth* 84.B5, pp. 2161–2168.

Dobson, D., P. Meredith, and S. Boon (2002). "Microseismicity associated With antigorite dehydration: Laboratory simulation of deep-focus earthquakes". In: *EGS General Assembly Conference Abstracts*, p. 3985.

Dominguez, L. A., T. Taira, and M. A. Santoyo (2016). "Spatiotemporal variations of characteristic repeating earthquake sequences along the Middle America Trench in Mexico". In: *Journal of Geophysical Research: Solid Earth* 121.12, pp. 8855–8870.

Dreger, D., R. M. Nadeau, and A. Chung (2007). "Repeating earthquake finite source models: Strong asperities revealed on the San Andreas Fault". In: *Geophysical Research Letters* 34.23.

Drilleau, M. et al. (2022). "Marsquake locations and 1-D seismic models for Mars from InSight data". In: *Journal of Geophysical Research: Planets* 127.9, e2021JE007067.

Eshelby, J. D. (1957). "The determination of the elastic field of an ellipsoidal inclusion, and related problems". In: *Proceedings of the royal society of London. Series A. Mathematical and physical sciences* 241.1226, pp. 376–396.

Evans, A. et al. (2014). "A wet, heterogeneous lunar interior: Lower mantle and core dynamo evolution". In: *Journal of Geophysical Research: Planets* 119.5, pp. 1061–1077.

Frohlich, C. and Y. Nakamura (2007). "Geographic variations in the tidal control of deep moonquake nests and speculation about their mechanical origin". In: *Lunar and Planetary Science Conference*. 1338, p. 1749.

Frohlich, C. and Y. Nakamura (2009). "The physical mechanisms of deep moonquakes and intermediate-depth earthquakes: How similar and how different?" In: *Physics of the Earth and Planetary Interiors* 173.3-4, pp. 365–374.

Gaddes, M., A. Hooper, and M. Bagnardi (2019). "Using machine learning to automatically detect volcanic unrest in a time series of interferograms". In: *Journal of Geophysical Research: Solid Earth* 124.11, pp. 12304–12322.

Gagnepain-Beyneix, J. et al. (2006). "A seismic model of the lunar mantle and constraints on temperature and mineralogy". In: *Physics of the Earth and Planetary Interiors* 159.3-4, pp. 140–166.

Gao, D., H. Kao, and B. Wang (2021). "Misconception of waveform similarity in the identification of repeating earthquakes". In: *Geophysical Research Letters* 48.13.

Garcia, R. F. et al. (2019). "Lunar seismology: An update on interior structure models". In: *Space Science Reviews* 215.8, pp. 1–47.

Garcia, R. F. et al. (2011). "Very preliminary reference Moon model". In: *Physics of the Earth and Planetary Interiors* 188.1-2, pp. 96–113.

— (2012). "Erratum to "Very Preliminary Reference Moon Model", by RF Garcia, J. Gagnepain-Beyneix, S. Chevrot, P. Lognonné [Phys. Earth Planet. Inter. 188 (2011) 96–113]". In: *Physics of the Earth and Planetary Interiors* 202, pp. 89–91.

Gillet, K. et al. (2017). "Scattering attenuation profile of the Moon: Implications for shallow moonquakes and the structure of the megaregolith". In: *Physics of the Earth and Planetary Interiors* 262, pp. 28–40.

Goins, N. R., A. M. Dainty, and M. N. Toksöz (1981). "Seismic energy release of the Moon". In: *Journal of Geophysical Research: Solid Earth* 86.B1, pp. 378–388.

Gomberg, J. et al. (2011). "Seismic and geodetic signatures of fault slip at the Slumgullion Landslide Natural Laboratory". In: *Journal of Geophysical Research: Solid Earth* 116.B9.

Goulty, N. R. (1979). "Tidal triggering of deep moonquakes". In: *Physics of the Earth and Planetary Interiors* 19.1, pp. 52–58.

Green, H. and P. Burnley (1989). "A new self-organizing mechanism for deep-focus earthquakes". In: *Nature* 341.6244, pp. 733–737.

Hacker, B. R. et al. (2003). "Subduction factory 2. Are intermediate-depth earthquakes in subducting slabs linked to metamorphic dehydration reactions?" In: *Journal of Geophysical Research: Solid Earth* 108.B1.

Hardebeck, J. L. and P. M. Shearer (2002). "A new method for determining first-motion focal mechanisms". In: *Bulletin of the Seismological Society of America* 92.6, pp. 2264–2276.

Haviland, H. F. et al. (2021). "The Lunar Geophysical Network Landing Sites Science Rationale". In: *arXiv preprint arXiv:2107.06451*.

Hempel, S. et al. (2012). "Uncertainty of Apollo deep moonquake locations and implications for future network designs". In: *Icarus* 220.2, pp. 971–980.

Huang, H. and L. Meng (2018). "Slow unlocking processes preceding the 2015 Mw 8.4 Illapel, Chile, earthquake". In: *Geophysical Research Letters* 45.9, pp. 3914–3922.

Igarashi, T., T. Matsuzawa, and A. Hasegawa (2003). "Repeating earthquakes and interplate aseismic slip in the northeastern Japan subduction zone". In: *Journal of Geophysical Research: Solid Earth* 108.B5.

Imanishi, K. and W. L. Ellsworth (2006). "Source scaling relationships of microearthquakes at Parkfield, CA, determined using the SAFOD pilot hole seismic array". In: *Washington DC American Geophysical Union Geophysical Monograph Series* 170, pp. 81–90.

Imanishi, K., W. L. Ellsworth, and S. G. Prejean (2004). "Earthquake source parameters determined by the SAFOD Pilot Hole seismic array". In: *Geophysical Research Letters* 31.12.

John, T. et al. (2009). "Generation of intermediate-depth earthquakes by self-localizing thermal runaway". In: *Nature Geoscience* 2.2, pp. 137–140.

Karato, S.-i., M. R. Riedel, and D. A. Yuen (2001). "Rheological structure and deformation of subducted slabs in the mantle transition zone: implications for mantle circulation and deep earthquakes". In: *Physics of the Earth and Planetary Interiors* 127.1-4, pp. 83–108.

Kawamura, T. et al. (2017). "Evaluation of deep moonquake source parameters: Implication for fault characteristics and thermal state". In: *Journal of Geophysical Research: Planets* 122.7, pp. 1487–1504.

Kawamura, T. et al. (2022). "An autonomous lunar geophysical experiment package (ALGEP) for future space missions". In: *Experimental Astronomy*, pp. 1–24.

Kelemen, P. B. and G. Hirth (2007). "A periodic shear-heating mechanism for intermediate-depth earthquakes in the mantle". In: *Nature* 446.7137, pp. 787–790.

Kelly, C. et al. (2013). "Temporal changes in attenuation associated with the 2004 M6. 0 Parkfield earthquake". In: *Journal of Geophysical Research: Solid Earth* 118.2, pp. 630–645.

Khan, A. and K. Mosegaard (2002). "An inquiry into the lunar interior: A nonlinear inversion of the Apollo lunar seismic data". In: *Journal of Geophysical Research: Planets* 107.E6, pp. 3–1.

Khan, A., K. Mosegaard, and K. L. Rasmussen (2000). "A new seismic velocity model for the Moon from a Monte Carlo inversion of the Apollo lunar seismic data". In: *Geophysical Research Letters* 27.11, pp. 1591–1594.

Khan, A. et al. (2014). "Geophysical evidence for melt in the deep lunar interior and implications for lunar evolution". In: *Journal of Geophysical Research: Planets* 119.10, pp. 2197–2221.

Kim, A. et al. (2016). "Changes in repeating earthquake slip behavior following the 2004 Parkfield main shock from waveform empirical Green's functions finite-source inversion". In: *Journal of Geophysical Research: Solid Earth* 121.3, pp. 1910–1926.

Kirby, S. H. (1987). "Localized polymorphic phase transformations in high-pressure faults and applications to the physical mechanism of deep earthquakes". In: *Journal of Geophysical Research: Solid Earth* 92.B13, pp. 13789–13800.

Kirby, S. H. et al. (1996). "Metastable mantle phase transformations and deep earthquakes in subducting oceanic lithosphere". In: *Reviews of geophysics* 34.2, pp. 261–306.

Konca, A. O. et al. (2008). "Partial rupture of a locked patch of the Sumatra megathrust during the 2007 earthquake sequence". In: *Nature* 456.7222, pp. 631–635.

Koyama, J. and Y. Nakamura (1980). "Focal mechanism of deep moonquakes". In: *Lunar and Planetary Science Conference Proceedings*. Vol. 11, pp. 1855–1865.

Kufner, S.-K. et al. (2021). "Not all icequakes are created equal: Basal icequakes suggest diverse bed deformation mechanisms at Rutford Ice Stream, West Antarctica". In: *Journal of Geophysical Research: Earth Surface* 126.3.

Lammlein, D. R. (1977). "Lunar seismicity and tectonics". In: *Physics of the Earth and Planetary Interiors* 14.3, pp. 224–273.

Latham, G. et al. (1972). "Moonquakes and lunar tectonism". In: *The Moon* 4.3, pp. 373–382.

Latham, G. V. et al. (1970a). "Apollo 11 passive seismic experiment". In: *Geochimica et Cosmochimica Acta Supplement* 1, p. 2309.

Latham, G. V. et al. (1970b). "Passive seismic experiment". In: *Science* 167.3918, pp. 455–457.

Lawrence, D. et al. (2003). "Small-area thorium features on the lunar surface". In: *Journal of Geophysical Research: Planets* 108.E9.

Lengliné, O. and D. Marsan (2009). "Inferring the coseismic and postseismic stress changes caused by the 2004 Mw= 6 Parkfield earthquake from variations of recurrence times of microearthquakes". In: *Journal of Geophysical Research: Solid Earth* 114.B10.

Lengliné, O. et al. (2014). "Fluid-induced earthquakes with variable stress drop". In: *Journal of Geophysical Research: Solid Earth* 119.12, pp. 8900–8913.

Li, H. et al. (2019). "Lunar cumulate mantle overturn: A model constrained by ilmenite rheology". In: *Journal of Geophysical Research: Planets* 124.5, pp. 1357–1378.

Lognonné, P., J. Gagnepain-Beyneix, and H. Chenet (2003). "A new seismic model of the Moon: implications for structure, thermal evolution and formation of the Moon". In: *Earth and Planetary Science Letters* 211.1-2, pp. 27–44.

Maaten, L. v. d. and G. Hinton (2008). "Visualizing data using t-SNE". In: *Journal of machine learning research* 9.Nov, pp. 2579–2605.

Malebran, C. V. et al. (2020). "Seismicity clusters in Central Chile: investigating the role of repeating earthquakes and swarms in a subduction region". In: *Geophysical Journal International*.

Marone, C., J. E. Vidale, and W. L. Ellsworth (1995). "Fault healing inferred from time dependent variations in source properties of repeating earthquakes". In: *Geophysical Research Letters* 22.22, pp. 3095–3098.

Matsuyama, I. et al. (2016). "GRAIL, LLR, and LOLA constraints on the interior structure of the Moon". In: *Geophysical Research Letters* 43.16, pp. 8365–8375.

McInnes, L., J. Healy, and S. Astels (2017). "hdbscan: Hierarchical density based clustering." In: *Journal of Open Source Software* 2.11, p. 205.

Meade, C. and R. Jeanloz (1991). "Deep-focus earthquakes and recycling of water into the Earth's mantle". In: *Science* 252.5002, pp. 68–72.

Mia, M. S., M. Abdelmeguid, and A. E. Elbanna (2022). "Spatio-Temporal Clustering of Seismicity Enabled by Off-Fault Plasticity". In: *Geophysical Research Letters* 49.8, e2021GL097601.

Minshull, T. and N. Goulty (1988). "The influence of tidal stresses on deep moonquake activity". In: *Physics of the earth and planetary interiors* 52.1-2, pp. 41–55.

Nadeau, R. et al. (1994). "Seismological studies at Parkfield III: Microearthquake clusters in the study of fault-zone dynamics". In: *Bulletin of the Seismological Society of America* 84.2, pp. 247–263.

Nadeau, R. M., W. Foxall, and T. McEvilly (1995). "Clustering and periodic recurrence of microearthquakes on the San Andreas fault at Parkfield, California". In: *Science* 267.5197, pp. 503–507.

Nadeau, R. M. and L. R. Johnson (1998). "Seismological studies at Parkfield VI: Moment release rates and estimates of source parameters for small repeating earthquakes". In: *Bulletin of the Seismological Society of America* 88.3, pp. 790–814.

Nadeau, R. M. and T. V. McEvilly (1999). "Fault slip rates at depth from recurrence intervals of repeating microearthquakes". In: *Science* 285.5428, pp. 718–721.

Nadeau, R. M. et al. (2004). "Detailed kinematics, structure and recurrence of micro-seismicity in the SAFOD target region". In: *Geophysical Research Letters* 31.12.

Nakamura, Y. (1978). "A1 moonquakes-source distribution and mechanism". In: *Lunar and Planetary Science Conference Proceedings*. Vol. 9, pp. 3589–3607.

Nakamura, Y. et al. (1977). "Seismic indication of broad-scale lateral heterogeneities in the lunar interior-A preliminary report". In: *Lunar and Planetary Science Conference Proceedings*. Vol. 8, pp. 487–498.

Nakamura, Y. (1983). "Seismic velocity structure of the lunar mantle". In: *Journal of Geophysical Research: Solid Earth* 88.B1, pp. 677–686.

— (2003). "New identification of deep moonquakes in the Apollo lunar seismic data". In: *Physics of the Earth and Planetary Interiors* 139.3-4, pp. 197–205.

— (2005a). "Farside deep moonquakes and deep interior of the Moon". In: *Journal of Geophysical Research: Planets* 110.E1.

— (2005b). "Spatial Extent of a Deep Moonquake Nest: A Preliminary Report of Reexamination". In: *Lunar and Planetary Science XXXVI, Part 14*.

Nakamura, Y., G. V. Latham, and H. J. Dorman (1980). "How we processed Apollo lunar seismic data". In: *Physics of the Earth and Planetary Interiors* 21.2-3, pp. 218–224.

— (1982). "Apollo lunar seismic experiment—Final summary". In: *Journal of Geophysical Research: Solid Earth* 87.S01, A117–A123.

National Academies of Sciences, Engineering, and Medicine (2022). *Origins, Worlds, and Life: A Decadal Strategy for Planetary Science and Astrobiology 2023-2032*. Tech. rep.

Nunn, C., R. C. Weber, and M. Panning (2020a). "Improving the Accessibility of the Apollo Seismic Data: Archiving at IRIS and the PDS". In: *Lunar and Planetary Science Conference*. 2326, p. 2269.

Nunn, C. et al. (2022). "A New Archive of Apollo Seismic Data". In: *LPI Contributions* 2678, p. 1170.

Nunn, C., Y. Nakamura, and H. Igel (2017). "Apollo passive seismic experiments: lunar data in SEED format". In: *AGU Fall Meeting Abstracts*. Vol. 2017, P41D–2860.

Nunn, C. et al. (2020b). "Lunar seismology: A data and instrumentation review". In: *Space Science Reviews* 216.5, pp. 1–39.

Ocaña, E. et al. (2008). "Spatial analysis of the La Paca, SE Spain, 2005 seismic series through the relative location of multiplets and principal component analysis". In: *Physics of the Earth and Planetary Interiors* 166.3-4, pp. 117–127.

Ogawa, M. (1987). "Shear instability in a viscoelastic material as the cause of deep focus earthquakes". In: *Journal of Geophysical Research: Solid Earth* 92.B13, pp. 13801–10.

Panning, M. et al. (2021). "Farside Seismic Suite (FSS): First seismic data from the farside of the Moon delivered by a commercial lander". In: *AGU Fall Meeting Abstracts*. Vol. 2021, P54C–01.

Peng, Z. and Y. Ben-Zion (2005). "Spatiotemporal variations of crustal anisotropy from similar events in aftershocks of the 1999 M 7.4 Izmit and M 7.1 Düzce, Turkey, earthquake sequences". In: *Geophysical Journal International* 160.3, pp. 1027–1043.

Perfettini, H. and J. Schmittbuhl (2001). "Periodic loading on a creeping fault: Implications for tides". In: *Geophysical Research Letters* 28.3, pp. 435–438.

Perfettini, H. et al. (2001). "Frictional response induced by time-dependent fluctuations of the normal loading". In: *Journal of Geophysical Research: Solid Earth* 106.B7, pp. 13455–13472.

Perrin, C., F. Waldhauser, and C. H. Scholz (2021). "The shear deformation zone and the smoothing of faults with displacement". In: *Journal of Geophysical Research: Solid Earth* 126.5, e2020JB020447.

Petersen, T. (2007). "Swarms of repeating long-period earthquakes at Shishaldin Volcano, Alaska, 2001–2004". In: *Journal of Volcanology and Geothermal Research* 166.3-4, pp. 177–192.

Poli, P. (2017). "Creep and slip: Seismic precursors to the Nuugaatsiaq landslide (Greenland)". In: *Geophysical Research Letters* 44.17, pp. 8832–8836.

Poli, P. et al. (2016). "Earthquakes initiation and thermal shear instability in the Hindu Kush intermediate depth nest". In: *Geophysical Research Letters* 43.4, pp. 1537–1542.

Poupinet, G., A. Ratdomopurbo, O. Coutant, et al. (1996). "On the use of earthquake multiplets to study fractures and the temporal evolution of an active volcano". In.

Prieto, G. A. et al. (2012). "Earthquake nests as natural laboratories for the study of intermediate-depth earthquake mechanics". In: *Tectonophysics* 570, pp. 42–56.

Proctor, B. and G. Hirth (2015). "Role of pore fluid pressure on transient strength changes and fabric development during serpentine dehydration at mantle conditions:

Implications for subduction-zone seismicity". In: *Earth and Planetary Science Letters* 421, pp. 1–12.

Qin, C., A. C. Muirhead, and S. Zhong (2012). "Correlation of deep moonquakes and mare basalts: Implications for lunar mantle structure and evolution". In: *Icarus* 220.1, pp. 100–105.

Qiu, Q. et al. (2016). "The mechanism of partial rupture of a locked megathrust: The role of fault morphology". In: *Geology* 44.10, pp. 875–878.

Rubin, A. M., D. Gillard, and J.-L. Got (1999). "Streaks of microearthquakes along creeping faults". In: *Nature* 400.6745, pp. 635–641.

Rubinstein, J. L., N. Uchida, and G. C. Beroza (2007). "Seismic velocity reductions caused by the 2003 Tokachi-Oki earthquake". In: *Journal of Geophysical Research: Solid Earth* 112.B5.

Ruina, A. (1983). "Slip instability and state variable friction laws". In: *Journal of Geophysical Research: Solid Earth* 88.B12, pp. 10359–10370.

Ruiz, S. et al. (2014). "Intense foreshocks and a slow slip event preceded the 2014 Iquique M w 8.1 earthquake". In: *Science* 345.6201, pp. 1165–1169.

Sakamaki, T. et al. (2010). "Density of high-Ti basalt magma at high pressure and origin of heterogeneities in the lunar mantle". In: *Earth and Planetary Science Letters* 299.3-4, pp. 285–289.

Sammis, C. G., R. M. Nadeau, and L. R. Johnson (1999). "How strong is an asperity?" In: *Journal of Geophysical Research: Solid Earth* 104.B5, pp. 10609–10619.

Sammis, C. G. and J. R. Rice (2001). "Repeating earthquakes as low-stress-drop events at a border between locked and creeping fault patches". In: *Bulletin of the Seismological Society of America* 91.3, pp. 532–537.

Schaff, D. P. and G. C. Beroza (2004). "Coseismic and postseismic velocity changes measured by repeating earthquakes". In: *Journal of Geophysical Research: Solid Earth* 109.B10.

Schaff, D. P. and F. Waldhauser (2005). "Waveform cross-correlation-based differential travel-time measurements at the Northern California Seismic Network". In: *Bulletin of the Seismological Society of America* 95.6, pp. 2446–2461.

Schaff, D. P. et al. (2002). "High-resolution image of Calaveras fault seismicity". In: *Journal of Geophysical Research: Solid Earth* 107.B9, ESE–5.

Schmidt, D. et al. (2005). "Distribution of aseismic slip rate on the Hayward fault inferred from seismic and geodetic data". In: *Journal of Geophysical Research: Solid Earth* 110.B8.

Schmittbuhl, J. et al. (2016). "Long-lasting seismic repeaters in the Central Basin of the Main Marmara fault". In: *Geophysical Research Letters* 43.18, pp. 9527–9534.

Schubnel, A. et al. (2013). "Deep-focus earthquake analogs recorded at high pressure and temperature in the laboratory". In: *Science* 341.6152, pp. 1377–1380.

Shakibay Senobari, N. and G. J. Funning (2019). "Widespread fault creep in the northern San Francisco Bay Area revealed by multistation cluster detection of repeating earthquakes". In: *Geophysical Research Letters* 46.12, pp. 6425–6434.

Shimizu, H. et al. (2013). "Constraint on the lunar core size from electromagnetic sounding based on magnetic field observations by an orbiting satellite". In: *Icarus* 222.1, pp. 32–43.

Sippl, C. et al. (2013). "Geometry of the Pamir-Hindu Kush intermediate-depth earthquake zone from local seismic data". In: *Journal of Geophysical Research: Solid Earth* 118.4, pp. 1438–1457.

Solomon, S. and J. Chaiken (1976). "Thermal expansion and thermal stress in the moon and terrestrial planets-Clues to early thermal history". In: *Lunar and planetary science conference proceedings*. Vol. 7, pp. 3229–3243.

Steinberger, B., D. Zhao, and S. C. Werner (2015). "Interior structure of the Moon: constraints from seismic tomography, gravity and topography". In: *Physics of the Earth and Planetary Interiors* 245, pp. 26–39.

Sun, W. and H. Tkalčić (2022). "Repetitive marsquakes in Martian upper mantle". In: *Nature Communications* 13.1, pp. 1–9.

Tartèse, R. et al. (2019). "Constraining the evolutionary history of the Moon and the inner solar system: a case for new returned lunar samples". In: *Space Science Reviews* 215.8, pp. 1–50.

Templeton, D. C., R. M. Nadeau, and R. Bürgmann (2008). "Behavior of repeating earthquake sequences in central California and the implications for subsurface fault creep". In: *Bulletin of the Seismological Society of America* 98.1, pp. 52–65.

Thielmann, M. et al. (2015). "Intermediate-depth earthquake generation and shear zone formation caused by grain size reduction and shear heating". In: *Geology* 43.9, pp. 791–794.

Thielmann, M. (2018). "Grain size assisted thermal runaway as a nucleation mechanism for continental mantle earthquakes: Impact of complex rheologies". In: *Tectonophysics* 746, pp. 611–623.

Thomas, M. Y. et al. (2014). "Quasi-dynamic versus fully dynamic simulations of earthquakes and aseismic slip with and without enhanced coseismic weakening". In: *Journal of Geophysical Research: Solid Earth* 119.3, pp. 1986–2004.

Tittmann, B. et al. (1980). "Possible mechanism for seismic attenuation in rocks containing small amounts of volatiles". In: *Journal of Geophysical Research: Solid Earth* 85.B10, pp. 5199–5208.

Toksöz, M. N., N. R. Goins, and C. Cheng (1977). "Moonquakes: Mechanisms and relation to tidal stresses". In: *Science* 196.4293, pp. 979–981.

Toksöz, M. N. et al. (1974). "Structure of the Moon". In: *Reviews of Geophysics* 12.4, pp. 539–567.

Turner, R. C., R. M. Nadeau, and R. Bürgmann (2013). "Aseismic slip and fault interaction from repeating earthquakes in the Loma Prieta aftershock zone". In: *Geophysical Research Letters* 40.6, pp. 1079–1083.

Uchida, N. (2019). "Detection of repeating earthquakes and their application in characterizing slow fault slip". In: *Progress in Earth and Planetary Science* 6.1, pp. 1–21.

Uchida, N. and R. Bürgmann (2019). "Repeating earthquakes". In: *Annual Review of Earth and Planetary Sciences* 47, pp. 305–332.

Uchida, N. and T. Matsuzawa (2013). "Pre-and postseismic slow slip surrounding the 2011 Tohoku-oki earthquake rupture". In: *Earth and Planetary Science Letters* 374, pp. 81–91.

Uchida, N. et al. (2007). "Source parameters of a M4. 8 and its accompanying repeating earthquakes off Kamaishi, NE Japan: Implications for the hierarchical structure of asperities and earthquake cycle". In: *Geophysical research letters* 34.20.

Uchida, N. et al. (2012). "Source parameters of microearthquakes on an interplate asperity off Kamaishi, NE Japan over two earthquake cycles". In: *Geophysical Journal International* 189.2, pp. 999–1014.

Uchida, N. et al. (2015). "Postseismic response of repeating earthquakes around the 2011 Tohoku-oki earthquake: Moment increases due to the fast loading rate". In: *Journal of Geophysical Research: Solid Earth* 120.1, pp. 259–274.

Uchida, N. et al. (2020). "Stagnant forearc mantle wedge inferred from mapping of shear-wave anisotropy using S-net seafloor seismometers". In: *Nature communications* 11.1, pp. 1–8.

Vasco, D. (1989). "Deriving source-time functions using principal component analysis". In: *Bulletin of the Seismological Society of America* 79.3, pp. 711–730.

— (1990). "Seismic source representation in orthogonal functions". In: *Geophysical journal international* 102.3, pp. 531–535.

Vavryčuk, V. et al. (2017). "Moment tensor inversion based on the principal component analysis of waveforms: Method and application to microearthquakes in West Bohemia, Czech Republic". In: *Seismological Research Letters* 88.5, pp. 1303–1315.

Vidale, J. et al. (1994). "Variations in rupture process with recurrence interval in a repeated small earthquake". In: *Nature* 368.6472, pp. 624–626.

Vidale, J. et al. (2017). *Southern California Earthquake Center: Research Program in Earthquake System Science, 2017-2022*. Tech. rep.

Waldhauser, F. (2013). *Real-time double-difference earthquake locations for northern California*.

Waldhauser, F. and W. L. Ellsworth (2002). "Fault structure and mechanics of the Hayward fault, California, from double-difference earthquake locations". In: *Journal of Geophysical Research: Solid Earth* 107.B3, ESE–3.

Waldhauser, F. and D. P. Schaff (2008). "Large-scale relocation of two decades of Northern California seismicity using cross-correlation and double-difference methods". In: *Journal of Geophysical Research: Solid Earth* 113.B8.

— (2021). "A Comprehensive Search for Repeating Earthquakes in Northern California: Implications for Fault Creep, Slip Rates, Slip Partitioning, and Transient Stress". In: *Journal of Geophysical Research: Solid Earth* 126.11, e2021JB022495.

Walsh, J. J. and J. Watterson (1988). "Analysis of the relationship between displacements and dimensions of faults". In: *Journal of Structural geology* 10.3, pp. 239–247.

Watters, T. R., C. L. Johnson, and R. Schultz (2010). "Lunar tectonics". In: *Planetary tectonics* 11, p. 121.

Watterson, J. (1986). "Fault dimensions, displacements and growth". In: *Pure and Applied Geophysics* 124.1, pp. 365–373.

Weber, R. C., B. Bills, and C. Johnson (2009). "Constraints on deep moonquake focal mechanisms through analyses of tidal stress". In: *Journal of Geophysical Research: Planets* 114.E5.

Weber, R. C. et al. (2011). "Seismic detection of the lunar core". In: *science* 331.6015, pp. 309–312.

Weber, R. C., B. G. Bills, and C. L. Johnson (2010). "A simple physical model for deep moonquake occurrence times". In: *Physics of the Earth and Planetary Interiors* 182.3-4, pp. 152–160.

Wellik, J. J., S. G. Prejean, and D. K. Syahbana (2021). "Repeating Earthquakes During Multiple Phases of Unrest and Eruption at Mount Agung, Bali, Indonesia, 2017". In: *Frontiers in Earth Science* 9, p. 369.

White, R. A. et al. (1998). "Observations of hybrid seismic events at Soufriere Hills volcano, Montserrat: July 1995 to September 1996". In: *Geophysical Research Letters* 25.19, pp. 3657–3660.

White, R. S. et al. (2011). "Dynamics of dyke intrusion in the mid-crust of Iceland". In: *Earth and Planetary Science Letters* 304.3-4, pp. 300–312.

Wieczorek, M. A. et al. (2006). "The constitution and structure of the lunar interior". In: *Reviews in mineralogy and geochemistry* 60.1, pp. 221–364.

Wieczorek, M. A. et al. (2013). "The crust of the Moon as seen by GRAIL". In: *Science* 339.6120, pp. 671–675.

Wiens, D. A. and N. O. Snider (2001). "Repeating deep earthquakes: evidence for fault reactivation at great depth". In: *Science* 293.5534, pp. 1463–1466.

Williams, J. G. et al. (2006). "Lunar laser ranging science: Gravitational physics and lunar interior and geodesy". In: *Advances in Space Research* 37.1, pp. 67–71.

Williams, J. G. et al. (2014). "Lunar interior properties from the GRAIL mission". In: *Journal of Geophysical Research: Planets* 119.7, pp. 1546–1578.

Williams, J. R., J. Hawthorne, and O. Lengliné (2019). "The long recurrence intervals of small repeating earthquakes may be due to the slow slip rates of small fault strands". In: *Geophysical Research Letters* 46.22, pp. 12823–12832.

Williams, M. et al. (2010). *Unlocking the Secrets of the North American Continent: An Earthscope Science Plan for 2010 – 2020*. Tech. rep. www.earthscope-program-2003-2018.org.

Wu, C. et al. (2014). "Triggering of repeating earthquakes in central California". In: *Geophysical Research Letters* 41.5, pp. 1499–1505.

Wyss, M. et al. (2004). "Fractal dimension and b-value on creeping and locked patches of the San Andreas fault near Parkfield, California". In: *Bulletin of the Seismological Society of America* 94.2, pp. 410–421.

Yamada, M., J. Mori, and Y. Matsushi (2016). "Possible stick-slip behavior before the Rausu landslide inferred from repeating seismic events". In: *Geophysical Research Letters* 43.17, pp. 9038–9044.

Yamada, R. et al. (2011). "Optimisation of seismic network design: application to a geophysical international lunar network". In: *Planetary and Space Science* 59.4, pp. 343–354.

Yang, W., E. Hauksson, and P. M. Shearer (2012). "Computing a large refined catalog of focal mechanisms for southern California (1981–2010): Temporal stability of the style of faulting". In: *Bulletin of the Seismological Society of America* 102.3, pp. 1179–1194.

Yang, Y. and X. Song (2020). "Temporal changes of the inner core from globally distributed repeating earthquakes". In: *Journal of Geophysical Research: Solid Earth* 125.3, e2019JB018652.

Yu, W.-c. (2016). "Time-dependent inner core structures examined using repeating earthquakes in subduction zones of the southwest Pacific". In: *Geophysical Journal International* 204.2, pp. 1204–1215.

Yu, W.-c. and L. Wen (2012). "Deep-focus repeating earthquakes in the Tonga–Fiji subduction zone". In: *Bulletin of the Seismological Society of America* 102.4, pp. 1829–1849.

Yuan, Y. et al. (2021). "New Methods for Data Stacking and P-and S-wave Arrival Time Determination Using the Deep Moonquake Apollo Recordings". In: *Journal of Geophysical Research: Planets* 126.2, e2020JE006424.

Zhao, D., J. Lei, and L. Liu (2008). "Seismic tomography of the Moon". In: *Chinese Science Bulletin* 53.24, pp. 3897–3907.

Zhao, D. et al. (2012). "Seismic tomography and geochemical evidence for lunar mantle heterogeneity: comparing with Earth". In: *Global and Planetary Change* 90, pp. 29–36.

Zuber, M. T. et al. (2012). "Gravity Recovery and Interior Laboratory (GRAIL): Mapping the lunar interior from crust to core". In: *GRAIL: Mapping the Moon's Interior*. Springer, pp. 3–24.